

Influence of multiphase processes on the chemistry and measurement
of organic compounds in indoor and outdoor environments

by

Demetrios Pagonis

B.S., Davidson College, 2013

A thesis submitted to the
Faculty of the Graduate School of the
University of Colorado in partial fulfillment
of the requirement for the degree of
Doctor of Philosophy

Department of Chemistry

2018

This thesis entitled:
Influence of multiphase processes on the chemistry and measurement of
organic compounds in indoor and outdoor environments
written by Demetrios Pagonis
has been approved for the Department of Chemistry

Professor Paul Ziemann

Professor Joost de Gouw

Date _____

The final copy of this thesis has been examined by the signatories, and we
find that both the content and the form meet acceptable presentation standards
of scholarly work in the above-mentioned discipline.

Pagonis, Demetrios (Ph.D., Chemistry, Department of Chemistry)

Influence of multiphase processes on the chemistry and measurement of organic compounds in indoor and outdoor environments

Thesis directed by Paul Ziemann

Abstract

Organic compounds are ubiquitous in indoor and outdoor environments, with organic aerosols and gases impacting air quality, global climate, and human health. The life cycle of volatile organic compounds (VOCs) in the atmosphere includes emission from indoor and outdoor sources, oxidation in the atmosphere to form secondary organic aerosol (SOA), and eventual deposition to a surface. Understanding each of these processes is necessary to predict the impact of organic compounds on indoor and outdoor environments, and this thesis presents the results of a series of studies across the life cycle of VOCs, examining the chemical and physical processes that transform organic compounds in the atmosphere.

First, the chemistry of multifunctional hydroperoxides in SOA is studied by a series of laboratory studies utilizing a model hydroperoxyaldehyde designed to represent the highly oxidized multifunctional compounds that impact SOA growth in pristine environments. Measurements of reaction rates, equilibrium constants, and decomposition mechanisms provide insight into how chemical structure and aerosol properties affect the chemistry of multifunctional hydroperoxides in SOA. Second, emission rates, deposition velocities, reaction rates, and reaction products from a field study in a university art museum are presented. This study quantifies the significant impact of human activities on indoor VOC emissions, as well as the effect of indoor surfaces and indoor oxidants on the fate of those emissions. Lastly, this thesis

presents a study aimed to improve researchers' ability to make time-resolved measurements of gas-phase organic compounds that partition to instrument surfaces and to Teflon tubing commonly used for sampling lines. The simple chromatography model presented here accurately predicts the delay in instrument response caused by gas-surface partitioning across all the tubing lengths, diameters, flow rates, and analytes tested. Together, the studies presented in this thesis advance the understanding of, and the ability to measure, the fate of organic compounds in indoor and outdoor environments.

Acknowledgements

First, Paul — thank you for your mentorship and everything you've taught me over the last five years. Your attention to detail across every aspect of a research project has made my experiments more creative, my writing more succinct, and my figure design more aesthetically pleasing. You taught me how to keep excitement and curiosity at the center of my research, and I am truly grateful for all the ways you've made me a better chemist.

Joost and Jose — thank you for all the advice and guidance on the many projects we've collaborated on and I'm looking forward to continuing to work with you in the future.

Many, many thanks to all the members of the Ziemann group. None of the work I've done could have been done without all the hard work you put in every day maintaining the instruments and chambers or all the time you've spent teaching me new methods. Megan — thank you for all the chemistry insights and your patience working with and teaching me for years. Luke — thank you for always having your door open to talk through whatever idea I'm struggling to articulate that day. Anne — all your help in the field and in lab is truly invaluable.

Lastly, Amanda — you've been a part of this entire journey and I never would have made it to this point without your love and support. Thank you.

Contents

Introduction.....	1
1.1. Organic compounds in the atmosphere.....	1
1.2. Indoor Air Quality.....	2
1.3. Measurements of Gas-Phase Organic Compounds.....	2
1.4. Thesis Overview	3
Chemistry of Hydroperoxycarbonyls in Secondary Organic Aerosol	5
2.1. Introduction.....	5
2.2. Materials and Methods.....	7
2.2.1. Chemicals.....	7
2.2.2. AHPA Solution Synthesis.....	8
2.2.3. Environmental Chamber Reactions.	8
2.2.4. Mass Spectrometric Analysis.....	10
2.2.5. Filter Sampling.....	11
2.2.6. Functional Group Analysis.	12
2.2.7. NMR Analysis.	12
2.3. Results and Discussion	13
2.3.1. Mechanism of Formation of AHPA.....	13
2.3.2. Yield of AHPA Formed From the Gas-Phase Reaction of Cyclodecene with O ₃ in the Presence of 1-Propanol.	13

2.3.3. Potential Reaction Pathways of AHPA.....	14
2.3.4. Mass Spectra of AHPA Standards.....	18
2.3.5. Rate and Equilibrium Constants for AHPA Cyclization.....	19
2.3.6. Peroxide Decomposition.....	23
2.3.7. Identification of Peroxide Decomposition Products.....	27
2.3.8. Particle Phase Alcohol and Water Exchange Reactions.....	36
2.4. Conclusions.....	38
Time-Resolved Measurements of Indoor Chemical Emission Rates, Deposition Velocities, and Reactions in a University Art Museum	41
3.1. Introduction.....	41
3.2. Materials and Methods.....	44
3.2.1. Art Museum Site.....	44
3.2.2. Measurements and Instrumentation.....	44
3.2.3. Art Museum Model.....	46
3.3. Results and Discussion	50
3.3.1. VOC Emission Rates.....	50
3.3.2. VOC Deposition Rates.....	56
3.3.3. Ozone Loss Rates.....	59
3.3.4. VOC Oxidation and Autoxidation.....	61
3.4. Conclusions.....	67

Effects of Gas-Wall Partitioning in Teflon Tubing and Instrumentation on Time-Resolved Measurements of Gas-Phase Organic Compounds	70
4.1. Introduction.....	70
4.2. Materials and Methods.....	72
4.2.1. Measurements of Tubing Delay.....	72
4.2.2. Chemicals.....	73
4.2.3. Model for Transport of an Organic Compound Through Teflon Tubing	74
4.3. Results and Discussion	79
4.3.1. Effect of Volatility, Tubing Length, and Flow Rate on Tubing Delays.	79
4.3.2. Estimating C_w for Teflon Tubing.....	87
4.3.3. Effect of Tubing Diameter on Tubing Delays.	88
4.3.4. Effect of Instrumentation on Delays.	92
4.4. Conclusions.....	93
Thesis Conclusions	96
References.....	100

List of Figures

Figure 2.1. Simple representation of the autoxidation mechanism that leads to HOM formation from an alkylperoxy radical (Crouse et al. 2013). The resulting HOM in this scheme is a hydroperoxycarbonyl, like the AHPA model compound studied here.	6
Figure 2.2. Mechanism of reaction of cyclodecene with O ₃ in the presence of 1-propanol to form 10- <i>n</i> -propoxy-10-hydroperoxy decanal (AHPA).....	8
Figure 2.3. Potential reactions of AHPA in SOA. In the concerted elimination and strong acid decomposition pathways H ₂ , water, and propanol co-products are not shown.	15
Figure 2.4. Mass spectra of AHPA standard obtained via EI-TDPBMS and CI-ITMS.	16
Figure 2.5. Time profile of the ratio of real-time EI-TDPBMS mass spectral signals measured at peaks characteristic of CPHA (<i>m/z</i> 169) and AHPA (<i>m/z</i> 171) in SOA formed from reaction of cyclodecene with O ₃ in the presence of 1-propanol and DOS seed particles. The data were fit to an exponential function to determine the timescale to establish cyclization equilibrium (τ_{eq}) and the equilibrium constant (K_{eq}).....	20
Figure 2.6. Time profiles of peroxide functional group content of SOA formed from the reaction of cyclodecene with O ₃ in the presence of 1-propanol and seed particles with the following composition: (squares) aqueous ammonium sulfate/sulfuric acid at 50% RH and pH = 1, (circles) dry DOS, and (diamonds) dry DOS/sulfuric acid.	25
Figure 2.7. Real-time EI-TDPBMS mass spectra measured at different times for SOA formed from the reaction of cyclodecene with O ₃ in the presence of 1-propanol and seed particles with different compositions as follows: (A) immediately after formation on dry DOS, (B) 4 h after formation on dry DOS, (C) immediately after formation on dry DOS/sulfuric	

acid, and (D) 4 h after formation on aqueous ammonium sulfate/sulfuric acid at 50% RH and pH = 1..... 29

Figure 2.8. Reference EI spectra of dipropoxy acetals: 1,1-dipropoxyheptane (A), 1,1-dipropoxypropane (B), and 1,1-dipropoxytrimethylamine (C) (Stein 2016; SDBSWeb, 2017). The characteristic fragmentation pattern is α -cleavage at the acetal carbon (m/z 131) followed by neutral loss of propene (m/z 89). 30

Figure 2.9. CI-ITMS mass spectra of filter extracts of SOA collected at different times from the reaction of cyclodecene with O₃ in the presence of 1-propanol in the absence or presence of seed particles as follows: (A) immediately after formation in the absence of seed particles, (B) 4 h after formation in the absence of seed particles, and (C) immediately after formation on dry sulfuric acid seed particles. DOS seed particles were not used in these experiments because DOS is the dominant signal in CI-ITMS at the concentrations used in chamber experiments..... 32

Figure 2.10. EI-TDPBMS spectrum of SOA produced from ozonolysis of cyclodecene in the presence of a large excess of carbon monoxide (A). NIST reference spectrum of sebacic acid (B) (Stein, 2016)..... 35

Figure 2.11. Real-time EI-TDPBMS mass spectra of (A) SOA formed from the reaction of cyclodecene with O₃ in the presence of 1-propanol and dry DOS/sulfuric acid seed particles, and with the subsequent addition of (B) methanol, and then (C) water..... 37

Figure 2.12. Potential reactions of hydroperoxyaldehydes in SOA. In the concerted elimination and strong acid decomposition pathways coproducts of hydrogen and water are not shown. 40

Figure 3.1. Schematic of the box model used to describe the transport, emission, deposition, and reaction of compounds in the University of Colorado Art Museum. The air exchange rate of the gallery is 10 hr^{-1} and the indoor-outdoor air exchange rate is 0.8 hr^{-1} . The museum is represented by two compartments, the gallery and the supply air + rest of the building, corresponding to the two sampling locations of this study. Air in each compartment is assumed to be perfectly mixed..... 47

Figure 3.2. Time series of carbon dioxide (A) and lactic acid (B) concentration measured by Picarro and iodide-CIMS, respectively, during an exhibit opening at the University of Colorado Art Museum. After the conclusion of the opening at 7:00 PM carbon dioxide is removed from the museum at the rate of indoor-outdoor air exchange, while lactic acid is lost at a faster rate due to deposition to surfaces. 54

Figure 3.3. Correlation of human emission factors for this study and Tang et al. 2016. Data points are plotted as the mass-to-charge ratio measured by the quadrupole PTR-MS. Emission factors between the two studies generally agree within a factor of two. Elevated ethanol emissions (m/z 47) observed in this study are likely due to alcohol consumption and decreased monoterpene emissions (m/z 137) are likely due to lower emissions from personal care products. Additionally, lower O_3 concentrations during this study led to lower secondary emissions of O_3 with squalene on occupants' skin..... 56

Figure 3.4. Deposition rates of organic compounds measured in the University of Colorado Art Museum as a function of volatility (C^*) and Henry's law coefficient (H) calculated using SIMPOL (Pankow and Asher, 2008) and GROMHE (Raventos-Duran et al. 2010), respectively. Deposition rate increases with decreasing volatility and with increasing

Henry's law coefficient. The dashed lines represent the bounds of measurable removal rates from the museum supply air given the sampling configuration used.....	58
Figure 3.5. O ₃ loss rate in the University of Colorado Art Museum gallery apportioned between reactions with gallery surfaces, occupants, NO, and NO ₂ . The art exhibit opening can be clearly seen as the dramatic increase in the loss rate to occupants at 5:00 PM on April 28 th .	61
Figure 3.6. Measured and modeled time series of limonene concentrations in the University of Colorado Art museum following the consumption of an orange showing removal by ventilation and chemistry (A). Measured and modeled concentrations of highly oxidized multifunctional compounds (HOMs) produced from limonene ozonolysis (B). The model outputs using the two published yields for limonene HOMs bracket the measured HOM concentrations.	63
Figure 3.7. Comparison of nitrate-CIMS mass spectra of HOMs formed from limonene ozonolysis in a laboratory (Jokinen et al. 2014) and in the University of Colorado Art Museum.....	65
Figure 4.1. Schematic of the chromatography model used to describe delays caused by gas-wall partitioning of organic compounds in Teflon tubing. Compounds flow through a series of perfectly mixed bins, undergoing gas-wall partitioning within each bin. The rates of flow between bins (k_f), absorption (k_a) and desorption (k_d) are dependent on tubing diameter, flow rate, and the saturation vapor concentration c^* of the compound being measured..	75
Figure 4.2. Simulated time profiles of compound concentrations at the tubing exit assuming flow in bins is perfectly mixed rather than laminar. The mixed flow profile was generated by	

running the model with gas-wall partitioning turned off. The profiles are for 1 m of tubing with 3/16 in. ID at a flow rate of 1 L min⁻¹..... 78

Figure 4.3. (A) PTR-MS time profiles measured in response to a step function increase in the concentration of 2-ketones. All compounds were measured simultaneously through 1 m of 3/16 in. ID PFA Teflon tubing at a flow rate of 0.36 L min⁻¹. Profiles are normalized to peak signal. The decline in signal over time is due to drift in instrument response following start-up. (B) PTR-MS time profiles measured in response to a step function decrease in the concentration of 2-ketones for tubing + PTR-MS (thick lines) and the PTR-MS alone (thin lines). The tubing used was a 3 m length of 3/16 in. ID PFA Teflon, and the flow rate for both traces was 0.36 L min⁻¹. Profiles are normalized to the equilibrium concentration measured prior to the step change. The signal-to-noise ratio is lower at higher carbon numbers due to gas-wall partitioning in the chamber lowering sample concentration as well as mass discrimination within the PTR-MS quadrupole mass analyzer. For visual clarity the traces for 2-octanone are not shown since they overlap with the traces for 2-decanone. 81

Figure 4.4. (A) Tubing delays for PTR-MS analysis of 2-ketones sampled using 1 and 3 m of 3/16 in. ID tubing at a flow rate of 0.36 L min⁻¹. The dashed line corresponds to the model case where the delay is proportional to the length of the tubing, which for these experiments is a factor of three. (B) Tubing delays for PTR-MS analysis of 2-ketones sampled using 3 m of 3/16 in. ID tubing and flow rates of 0.36 and 2.7 L min⁻¹. The dashed line corresponds to the model case where the delay is inversely proportional to the flow rate, which for these experiments is a factor of 0.13. 83

Figure 4.5. Comparison of modeled and measured tubing delays for homologous series of 2-ketones and 1-alkenes with a range of c^* values using short (ST = 1 m) and long (LT = 3 m) lengths of 3/16 in. ID tubing with low (LF = 0.36 L min⁻¹) flow, and long tubing with low and high (HF = 2.7 L min⁻¹) flow. The instrument delay for the PTR-MS is also shown. Values of c^* were calculated using SIMPOL.1 (Pankow and Asher, 2007). Error bars are only shown for the 2-ketones LF/ST case, and represent the variability (std. dev.) of the observations. Note that for the larger delays, the error bars are smaller than the data points..... 85

Figure 4.6. Simulated tubing delays presented as a function of c^* and flow rate for 3/16 in. ID PFA Teflon tubing. The range of conditions for measurements made in this study are shown by the dashed box. Values of c^* were calculated using SIMPOL.1 (Pankow and Asher, 2007)..... 87

Figure 4.7. Simulated tubing delays presented as a function of tubing ID at various flow rates for a compound with $c^* = 10^5 \mu\text{g m}^{-3}$ sampled through PFA tubing..... 90

Figure 4.8. Comparison of measured and modeled tubing delays for 1/16 in. ID and 3/16 ID PFA Teflon tubing sampling at 0.36 L min⁻¹. Values of c^* were calculated using SIMPOL.1 (Pankow and Asher, 2008)..... 90

Figure 4.9. Simulated tubing delays presented as a function of tubing ID and flow rate for a compound with $c^* = 10^5 \mu\text{g m}^{-3}$ sampled through PFA tubing. Reynolds numbers are overlaid to illustrate the nonlinear relationship between tubing delay, flow rate and tubing diameter..... 91

Figure 4.10. Measured and modeled time series for a 60-second pulse of 2-ketones measured by the PTR-MS through 1 m of 3/16 in. ID PFA Teflon tubing at 0.36 L min⁻¹. The tubing

model output was convolved with the instrument response function for each 2-ketone to
generate the traces..... 93

List of Tables

Table 2.1. Characteristic ions and fragmentation pathways for major products in SOA analyzed by EI-TDPBMS and CI-ITMS.....	19
Table 2.2. Peak shifts and assignments for ¹ H-NMR spectrum of AHPA-CPHA equilibrium. Molecular structures with assignment labels are included to show which protons undergo a change in chemical environment following the cyclization reaction (depicted in bold).	22
Table 2.3. Molar yields of functional groups in SOA formed in the presence of CO without seed particles or 1-propanol with sulfuric acid seed particles.	35
Table 3.1. Chemical reactions included in the box model of the museum. Rate constants for VOC reactions are those of limonene (Ziemann and Atkinson, 2012). All other rate constants were taken from the 2015 Jet Propulsion Lab Evaluation (Burkholder et al. 2015). Ozone deposition velocities v_d were fitted to minimize the error in model estimates of gallery ozone concentration.....	49
Table 3.2. Emission factors and peak concentrations for volatile chemical products emissions following application of paint to 12 m ² of wall in the University of Colorado Art Museum.....	51
Table 3.3. Mass and peak concentrations for VOCs emitted inside the University of Colorado Art Museum during the ARTISTIC campaign.	52
Table 3.4. Assigned molecular formulas and detected m/z's for HOMs formed from limonene ozonolysis in the University of Colorado Art Museum.	66

Chapter 1

Introduction

1.1. Organic compounds in the atmosphere

Organic compounds are ubiquitous in the atmosphere, impacting global climate, human health, and air quality (Atkinson and Arey, 2003; Ziemann and Atkinson, 2012). Atmospheric organic compounds exist in the gas phase (volatile organic compounds, VOCs) and in suspended solid and liquid particles (organic aerosol, OA). Roughly half of submicron aerosol mass in the atmosphere is OA, with OA impacting global climate through its role in cloud formation and interactions with solar radiation (Jimenez et al. 2009). Gas-phase VOCs are oxidized in the atmosphere to form less-volatile products that condense onto existing aerosols, forming secondary organic aerosol (SOA), a significant component of the global OA burden. SOA has significant negative impacts on human health and is an important determinant of air quality (Pope et al. 2009). However, many aspects of the formation of SOA from VOCs and subsequent reactions as SOA ages in the atmosphere are poorly understood, and research is needed to elucidate the chemical mechanisms that form and process SOA.

The reaction mechanisms that lead to SOA formation are modulated by the concentrations of nitrogen oxides (NO_x) in the atmosphere through reactions of nitric oxide with peroxy (RO_2) radicals, an intermediate in all major VOC oxidation pathways (Orlando and Tyndall, 2012). In the last 60 years, VOC and NO_x emissions in urban areas have declined dramatically, in large part because of reductions in emissions from automobiles (Warneke et al. 2012). The reduction in NO_x concentrations has led to changes in the gas-phase oxidative

chemistry of VOCs, increasing the lifetime of RO₂ radicals and allowing for intramolecular RO₂ radical reactions (autoxidation) to take place (Crouse et al. 2013; Praske et al. 2018). The products of autoxidation reactions tend to be large, peroxide-rich multifunctional molecules with sufficiently low vapor pressure to condense and form SOA. Little is known about the fate of these multifunctional hydroperoxides.

1.2. Indoor Air Quality

The average person in the United States spends 87% of their time indoors, indicating that indoor air quality and the concentration of pollutants indoor are key determinants of lifetime exposures (Klepeis et al. 2001). Anthropogenic emissions of VOCs that occur indoors directly impact the chemistry of the space where they are emitted, and they also have a significant impact on the total VOC burden in urban areas, with the total contribution of volatile chemical products (VCPs) to urban SOA potential exceeding that of automobile emissions in Los Angeles (McDonald et al. 2018). The spatial, temporal, and chemical evolution of these VCP emissions in the indoor environment is not well constrained, and there is a need to investigate the ways that human activities impact indoor air quality by making time-resolved measurements of indoor chemistry.

1.3. Measurements of Gas-Phase Organic Compounds

Gas-phase organic compounds in indoor and outdoor environments have a large range of volatilities, with the most volatile species having a saturation vapor concentration (C^*) roughly ten orders of magnitude higher than compounds that partition equally between gas and aerosol phases in the atmosphere (Pankow, 1994). Accordingly, gas-phase organic compounds show a wide range of partitioning behaviors in the presence of surfaces, with semi-, intermediate- and low-volatility compounds having an increased tendency to partition to the condensed phase. This

phenomenon is evident in the partitioning of organic compounds with C^* below $10^6 \mu\text{g m}^{-3}$ to Teflon used to construct the environmental chambers and the sampling lines used throughout studies of atmospheric chemistry. Partitioning of organic compounds to the Teflon walls in environmental chambers has been studied and systematically characterized (Matsunaga and Ziemann, 2010; Yeh and Ziemann 2015; Krechmer et al. 2016; Huang et al. 2018), but partitioning of organic compounds to the walls of Teflon tubing has not.

1.4. Thesis Overview

This thesis presents advances in the understanding of secondary organic aerosol chemistry in pristine environments, the chemistry of the indoor environment, and the effects of inlet tubing and instrument surfaces on time-resolved measurements of organic gases.

Chapter 2 describes the chemistry of multifunctional hydroperoxides in SOA. The chemical fate of a model hydroperoxide was studied under a variety of conditions in an environmental chamber. We present the first measurements of reaction rates and equilibrium constants for peroxyhemiacetal formation in SOA. Oligomeric decomposition products were identified for this model system, indicating a role for hydroperoxides in accretion reactions in SOA. We also present results suggesting that aerosol phase state can significantly impact the nature of acid catalysis in SOA. The reaction rates and mechanisms presented in this chapter will facilitate future studies of hydroperoxide chemistry in SOA.

Chapter 3 presents results from field measurements of indoor chemistry at the University of Colorado Art Museum. The time-resolved measurements presented in this chapter allow for quantification of emission rates from occupants and their activities, deposition rates of organic compounds to indoor surfaces, and ozone-driven oxidation chemistry. This work provides new insights into how indoor emissions are transported and reacted through the indoor environment.

Chapter 4 describes results from a study characterizing the effects of organic gases partitioning to Teflon tubing and instrument surfaces on time-resolved measurements. The time required for analytes to equilibrate with Teflon tubing and instrument surfaces can be on the order of minutes for compounds found in the gas phase in the indoor and outdoor environments, significantly impacting the measured time series of the analyte. We present a simple chromatography model that accurately captures the time needed for Teflon tubing to equilibrate with organic gases at variable tubing lengths, tubing diameters, sample flow rates, and organic functionality. This model will aid researchers in building sampling inlets and designing experiments in ways that minimize the impacts of gas-surface partitioning.

Chapter 2

Chemistry of Hydroperoxycarbonyls in Secondary Organic Aerosol

Reprinted with permission from Pagonis, D. and Ziemann, P. J.: Chemistry of Hydroperoxycarbonyls in secondary organic aerosol, *Aerosol Science and Technology*, 2018. DOI: 10.1080/02786826.2018.1511046, Copyright 2018.

2.1. Introduction

Highly oxidized multifunctional compounds (HOMs) formed from the reaction of ozone with α -pinene and by the oxidation of other volatile organic compounds (VOCs) have been measured as gas-phase (Ehn et al. 2012; Krapf et al. 2016) and particle-phase (Mutzel et al. 2015; Kristensen et al. 2016) reaction products in the laboratory and in the atmosphere. These HOMs have low volatility and are estimated to contribute over 50% of secondary organic aerosol (SOA) mass formed under pristine conditions (Ehn et al. 2014), and are expected to become a larger fraction of future SOA mass in urban areas as NO_x concentrations decrease due to air quality regulations (Praske et al. 2018). HOMs are believed to be labile multifunctional hydroperoxides formed through gas-phase autoxidation reactions (Crouse et al. 2013) that allow a single VOC-oxidant reaction to lead to multiple additions of oxygen to organic molecules. A simple example of the formation of a hydroperoxycarbonyl through an autoxidation mechanism is shown in Figure 2.1 (Crouse et al. 2013), where the initial alkylperoxy radical (RO_2^*) is a key intermediate formed in the oxidation of nearly all VOCs (Orlando and Tyndall 2012). Upon condensing into particles HOMs can decompose on timescales of tens of minutes or more (Krapf

et al. 2016; Mertes et al. 2012), but due to the chemical complexity of HOMs and the SOA matrix, the particle-phase mechanisms by which they react have not been studied in detail. For example, mass spectrometric analysis of gas-phase HOMs produced from the reaction of α -pinene with O_3 detected dozens of unique HOM molecular formulas corresponding to monomers and dimers with 5–20 carbons and 4–18 oxygens in each molecule (Ehn et al. 2012), and similar studies of SOA formed from this reaction have identified more than a thousand molecular formulas (Gao, Hall, and Johnston 2010). Since these studies rely on molecular formulas to assign products, they understate the chemical complexity of the HOMs and SOA by not being able to differentiate isomers or molecular structures. Studies of isoprene oxidation products have also observed that changes in aerosol acidity and phase state impact the condensed-phase chemistry of multifunctional peroxides (Riva et al. 2017; Zhang et al. 2018). For example, the reactive uptake of multifunctional hydroperoxides onto acidified seed aerosol can be suppressed by reduction of aerosol water in the seed particles and by organic coatings (Riva et al. 2017). Without greater knowledge of the molecular structures of the HOMs produced in these SOA systems, detailed studies of the particle-phase chemistry of HOMs are not feasible.

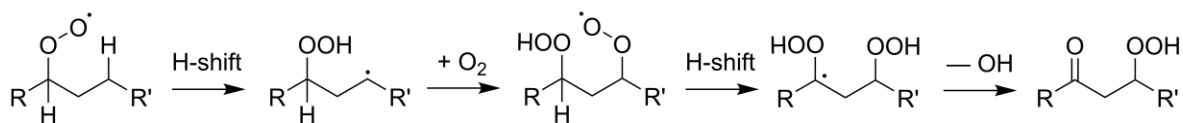


Figure 2.1. Simple representation of the autoxidation mechanism that leads to HOM formation from an alkylperoxy radical (Crouse et al. 2013). The resulting HOM in this scheme is a hydroperoxycarbonyl, like the AHPA model compound studied here.

In an attempt to overcome this difficulty, we recently investigated the kinetics, equilibria, products, and mechanisms of the particle-phase and solution reactions of 10-*n*-propoxy-10-hydroperoxydecanal [HOOCH(OCH₂CH₂CH₃)(CH₂)₈CHO], a C₁₃ α -alkoxy

hydroperoxyaldehyde (AHPA) that is an appropriate model for HOMs. This compound was chosen because in addition to being hydroperoxide-rich, HOM monomers in SOA produced by α -pinene ozonolysis have been reported to contain 1–2 carbonyl groups per molecule (Krapf et al. 2016; Mutzel et al. 2015). The highly reactive hydroperoxide and carbonyl groups in these HOMs are expected to play a critical role in their particle-phase chemistry (Ziemann and Atkinson 2012), so it was necessary that the model compound employed here contain both structural features. A recent study also suggested that production rates of AHPA in the atmosphere can be significant under certain conditions (McGillen et al. 2017). Additional advantages of studying this AHPA are that it can be easily synthesized with high yields either in solution or in an environmental chamber as a major component of SOA, thus allowing for detailed studies on a single hydroperoxycarbonyl compound under well-characterized conditions, and that it has sufficiently low vapor pressure that its chemistry involves only particle-phase reactions (Ziemann 2003). The results of this study provide information that will be useful for understanding and predicting the atmospheric fate of HOMs and their contributions to SOA formation, lifetime, and composition.

2.2. Materials and Methods

2.2.1. Chemicals. Chemicals with purities/grades and suppliers were as follows: *trans*-cyclodecene (98%), 1-propanol (99.5%), (Sigma-Aldrich); tridecanoic acid (98%) (Aldrich); 3-hexadecanone (99%) (Alfa Aesar); ethyl acetate (ACS) (Millipore); *bis*-diethylhexyl sebacate (DOS) (97%) (Fluka); ammonium sulfate (99.5%) (Fisher Scientific); sulfuric acid (ACS) (Macron); nitric oxide (>99%) (Matheson Gas); oxygen (UHP), carbon monoxide (CP) (AirGas). Ozone was produced from oxygen using a Del Ozone LG7 ozone generator. The reagents and

solvents used in functional group analysis have been described previously (Aimanant and Ziemann 2013a).

2.2.2. AHPA Solution Synthesis. AHPA standards were prepared by dissolving 10 μL of cyclodecene in 10 mL of 1-propanol [$\text{CH}_3\text{CH}_2\text{CH}_2\text{OH}$] and bubbling 2% O_3 through the solution at 1 L min^{-1} for 10 seconds to react all the alkene. The mechanism of the reaction is shown in Figure 2.2 and discussed below, but in solution produces AHPA with yields of $\geq 95\%$ (Zelikman et al. 1971). Due to the potentially explosive nature of organic peroxides researchers should take care when using this procedure. Total amounts of concentrated hydroperoxide should be kept to a minimum, especially when working with smaller peroxides than those synthesized here.

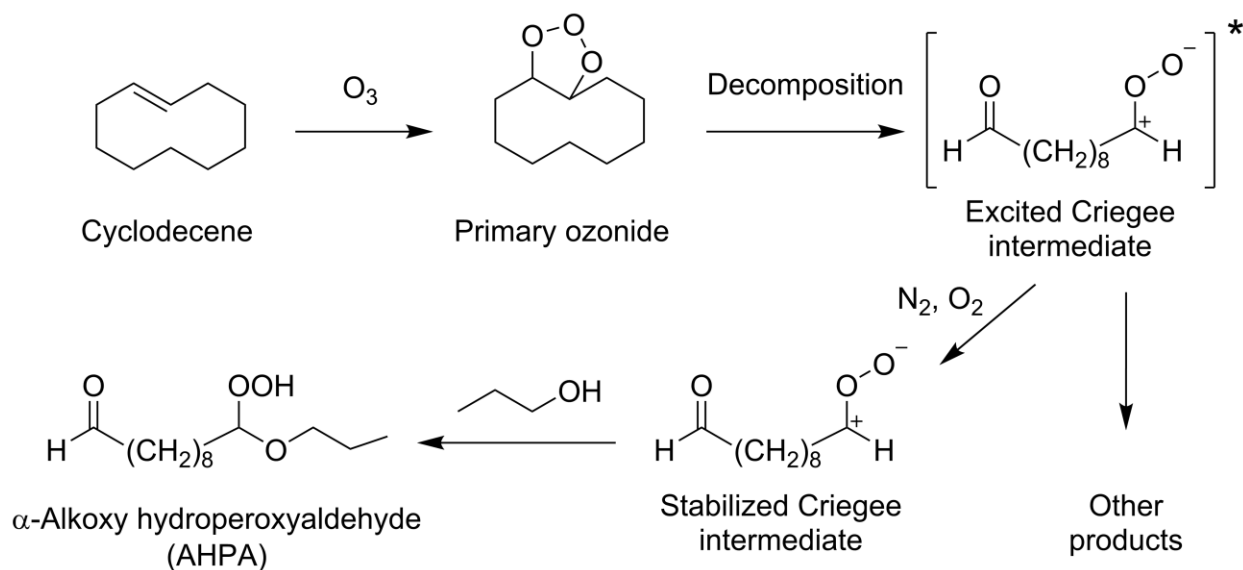


Figure 2.2. Mechanism of reaction of cyclodecene with O_3 in the presence of 1-propanol to form 10-*n*-propoxy-10-hydroperoxy decanal (AHPA).

2.2.3. Environmental Chamber Reactions. AHPA was also formed as a component of SOA in an 8.0 m^3 FEP Teflon environmental chamber by the gas-phase reaction of cyclodecene with O_3 in the presence of 1-propanol. The chamber is operated at room temperature ($\sim 25^\circ\text{C}$) and pressure (~ 630 Torr) and is flushed and filled with pure dry air (< 5 ppb hydrocarbons, $< 1\%$

RH) from an AADCO clean air generator. Reactions were typically conducted by adding seed particles, 1 ppm of cyclodecene, 1500 ppm of 1-propanol, and then 30 ppm of O₃ to initiate the reaction. Aerosol growth was complete within ~5 min. After 10 min of reaction, which was sufficient to react >95% of the cyclodecene (indicated by the cyclodecene decay measured with a proton transfer reaction-mass spectrometer (de Gouw and Warneke 2007) and estimated from the ~1 min lifetime calculated from the rate constant of $2.9 \times 10^{-17} \text{ cm}^3 \text{ molec}^{-1} \text{ s}^{-1}$ for *cis*-cyclodecene (Atkinson and Arey 2003) and the 30 ppm concentration of O₃), 60 ppm of NO was added to remove the remaining O₃ (O₃ + NO → NO₂ + O₂). Also, in one experiment particle-phase exchange reactions were probed by adding ~4000 ppm of methanol from 15–30 min after the aerosol stopped growing, and then adding ~6000 ppm of water (~18% RH) 30–60 min later. And in another experiment 630 ppm of carbon monoxide was used in place of 1-propanol as an SCI scavenger (>95% efficiency), with 50 ppm of cyclohexane used as an OH radical scavenger (Tobias and Ziemann, 2001; Docherty and Ziemann 2003). All reactants were added by flushing measured amounts from a glass bulb (with or without heating) into the chamber using ultra-high purity (UHP) N₂. Seed particles were either dioctyl sebacate (DOS), DOS/sulfuric acid, or aqueous ammonium sulfate/sulfuric acid. DOS was chosen because it is an inert, liquid organic compound with a sufficiently low vapor pressure to be essentially nonvolatile, for which we have developed methods for forming a nearly monodisperse seed aerosol. Use of DOS seed aerosol also allows for monitoring of particle wall losses using real-time mass spectrometry and the detection of SOA evaporation during a chamber reaction (Aimanant and Ziemann, 2013b). The DOS particles were formed using an evaporation-condensation generator, and the DOS/sulfuric acid particles were formed by evaporating 0.25 mL of 0.1% sulfuric acid/water from a glass bulb and allowing the small sulfuric acid particles generated following the addition to coagulate with

DOS seed particles produced by the evaporation-condensation generator. The coagulation was monitored with a scanning mobility particle sizer (SMPS) and the presence of sulfuric acid in the aerosol was confirmed by thermal desorption particle beam mass spectrometric (TDPBMS) analysis. These instruments are described below. The aqueous ammonium sulfate/sulfuric acid particles were formed by atomizing an aqueous solution of 8×10^{-3} M ammonium sulfate and 8×10^{-5} M sulfuric acid from a Collison atomizer into the chamber at 50% RH. According to E-AIM calculations (www.aim.env.uea.ac.uk/aim/aim.php; Clegg, Brimblecombe, and Wexler 1998; Wexler and Clegg, 2002) this aerosol had pH ~ 1 once it equilibrated with the water vapor in the chamber. Throughout each experiment the aerosol size distribution was measured using a scanning mobility particle sizer (SMPS) (Docherty and Ziemann 2003), aerosol composition was analyzed with a thermal desorption particle beam mass spectrometer (Tobias et al. 2000), and O_3 was monitored with a Dasibi 1003 Ozone Monitor. After each experiment aerosol was collected onto filters for offline analyses.

2.2.4. Mass Spectrometric Analysis. Aerosol is sampled directly into the thermal desorption particle beam mass spectrometer (TDPBMS) (Tobias et al. 2000) through an aerodynamic lens, which focuses the particles into a narrow beam for transport into a differentially-pumped high-vacuum chamber. There they impact and vaporize on a polymer-coated copper rod that is heated to 160°C , and the vapors are ionized by 70 eV electrons for analysis in an Extrel triple quadrupole mass spectrometer. To make explicit that TDPBMS mass spectra are obtained by electron ionization we hereafter refer to this as the EI-TDPBMS.

The EI-TDPBMS response to AHPA aerosol was calibrated by generating known mass concentrations of aerosol containing synthesized AHPA. A 6.3 mM solution of the AHPA standard in 1-propanol (synthesized as described above) was atomized in a Collison atomizer

that was coupled to a syringe pump (Chemyx Nexus 3000) and operated at 0.1 mL min^{-1} . The aerosol produced was dried by passing through charcoal and silica gel diffusion dryers and then the flow was split, with 0.75 L min^{-1} entering the EI-TDPBMS and 5 L min^{-1} passing through a filter sampler for collection of particles onto pre-weighed PTFE filters (Millipore Fluoropore $0.45 \text{ }\mu\text{m}$) for 50 min. Filters were reweighed to determine the mass concentration of the AHPA aerosol entering the EI-TDPBMS and analyzed using peroxide functional group analysis to determine AHPA purity, which was $>95\%$.

Solution-synthesized hydroperoxides and SOA collected on filter samples were also analyzed using a Thermo Finnigan PolarisQ chemical ionization ion trap mass spectrometer (CI-ITMS) equipped with a direct insertion probe (Ranney and Ziemann 2017). Samples were prepared for CI-ITMS analysis by drying $\sim 3 \text{ }\mu\text{L}$ of 5 mg mL^{-1} solution inside a small glass vial. The vials were then loaded into the tip of the direct insertion probe and thermally desorbed from the tip of the probe into the ionization region, where they underwent chemical ionization with isobutane as a reagent gas.

2.2.5. Filter Sampling. Aerosol was collected onto pairs of pre-weighed PTFE filters (Millipore Fluoropore $0.45 \text{ }\mu\text{m}$) by sampling air at 15 L min^{-1} through two 30 cm long, $\frac{1}{4}$ " outer diameter stainless steel tubes. Filters were re-weighed after sampling and the mass of SOA collected was determined by difference. All mass measurements were conducted with a Mettler Toledo XS3DU microbalance ($1 \text{ }\mu\text{g}$ precision). The collected SOA was extracted into ethyl acetate without sonication (three 5-min extractions into 5 mL of ethyl acetate, which were then pooled) immediately following weighing to minimize the amount of time for SOA components to react while on the filter. Extraction efficiencies determined previously for these methods were $>95\%$ (Matsunaga and Ziemann 2009). When necessary, samples were stored overnight in a

freezer at $-25\text{ }^{\circ}\text{C}$. Peroxide functional group analysis was always conducted immediately after extraction (never frozen), and all other functional group analyses were conducted within 18 h of filter collection.

2.2.6. Functional Group Analysis. Derivatization-spectrophotometric methods we developed previously (Aimanant and Ziemann 2013a) were used to quantify the moles of peroxide [HC–OOH] ($M = 46$), carboxyl [O=C–OH] ($M = 45$), carbonyl [C=O] ($M = 28$), ester [O=C–O]–R ($M = 44$), hydroxyl [HC–OH] ($M = 30$), and methylene [CH₂] ($M = 14$) functional groups in SOA, with the number of methylene groups being determined from the difference in the measured SOA mass and the mass of other functional groups calculated by assuming they have molecular weights corresponding to the structures shown in brackets. For convenience it was assumed that all the products have 10 carbons, the same number of as cyclodecene. This assumption is likely the largest source of error in our estimate of molecular weight, but since there was no evidence for the presence of oligomers in the SOA the error should not be large. Each derivatization technique involves the formation of a chromophore specific to the functional group being measured, and solutions were then analyzed using an Ocean Optics USB4000 UV-Vis spectrophotometer.

2.2.7. NMR Analysis. Proton nuclear magnetic resonance spectroscopy ($^1\text{H-NMR}$) analysis was carried out at the University of Colorado Department of Chemistry and Biochemistry NMR Spectroscopy Facility using a Bruker Avance-300 NMR. AHPA standards were synthesized as described above and either analyzed as is or purified by collecting fractions manually from HPLC eluent. Fractions were dried under UHP N₂ and reconstituted in deuterated dimethyl sulfoxide ($d_6\text{-DMSO}$) for analysis. Spectra were processed using the MestReNova

software package. Without and with purification the purity of AHPA determined from the NMR analysis was $\geq 95\%$.

2.3. Results and Discussion

2.3.1. Mechanism of Formation of AHPA. The mechanism of formation of the AHPA model HOM from reaction of cyclodecene with O_3 in the presence of 1-propanol is shown in Figure 2.2 (Ziemann 2003). The reaction is initiated by addition of O_3 to the C=C double bond to form an unstable primary ozonide, which rapidly decomposes to an excited Criegee intermediate (ECI). In solution, essentially all ECI are thermalized by collisions with solvent to form stabilized Criegee intermediates (SCI), which react almost exclusively with 1-propanol to form the AHPA, 10-*n*-propoxy-10-hydroperoxydecanal (Zelikman, et al. 1971). In the gas phase, the ECI can be thermalized by collisions with air to form SCI, which can undergo ring closure to form a secondary ozonide (SOZ) (Donahue et al. 2011), or in the presence of a high concentration of 1-propanol the SCI can react to form the AHPA. Using the approach presented in Docherty et al. (2005) we estimate that the large excess of 1-propanol scavenges $>95\%$ of the stabilized Criegee intermediates and $>99\%$ of the OH radicals produced from the reaction. ECI also undergo isomerization and decomposition reactions that lead to stable products and the formation of RO_2^{\bullet} radicals, which for the high VOC concentrations used here are expected to react with other RO_2^{\bullet} radicals and HO_2 radicals to form a variety of products containing carbonyl, hydroxyl, carboxyl, hydroperoxy, peroxy-carboxyl (Ziemann 2002), and possibly ester (Müller et al. 2008) groups.

2.3.2. Yield of AHPA Formed From the Gas-Phase Reaction of Cyclodecene with O_3 in the Presence of 1-Propanol. In order to interpret the experimental results of this study, it was necessary to determine the molar yield of AHPA (same as the molar yield of SCI) formed from

the gas-phase reaction of cyclodecene with O₃ in the presence of 1-propanol. This was determined from the difference in the molar yields of peroxide in SOA (moles of peroxide in SOA/moles of cyclodecene reacted) formed when 1-propanol and CO were used as SCI scavengers, since reaction of CO with the SCI forms CO₂ and a volatile C₁₀ dialdehyde (Atkinson 1997) rather than AHPA. From the measured molar yields of peroxide in SOA of 0.18 and 0.06 for the 1-propanol and CO experiments we obtained a molar yield of AHPA of 0.12. For this reaction we thus estimate that 12% of the products are formed through the SCI pathway and 88% through other pathways.

2.3.3. Potential Reaction Pathways of AHPA. A previous study of AHPA (Ziemann 2003) has shown that its hydroperoxide and carbonyl groups readily undergo an intramolecular reaction in SOA to form a cyclic peroxyhemiacetal (CPHA), as shown in Figure 2.3, and that these are the dominant early reaction products. Intermolecular peroxyhemiacetal oligomer formation is also possible for AHPA, as it has been observed from the reaction of the C₁₄ α -methoxy hydroperoxide and C₁₃ aldehyde products of the ozonolysis of 1-tetradecene in the presence of methanol (Tobias and Ziemann, 2000). In that study the C₂₇ peroxyhemiacetal was thermally desorbed intact for mass spectral analysis using temperature-programmed TDPBMS, and when the same technique was applied to AHPA SOA no C₂₆ peroxyhemiacetal oligomer (which would have been the product formed from reaction of two C₁₃ AHPA molecules) was detected, indicating that AHPA does not undergo intermolecular peroxyhemiacetal formation (Ziemann 2003). It is also worth noting that evidence for the stability of peroxides during thermal desorption under the conditions used here can be found in the EI-TDPBMS and CI-ITMS mass spectra shown in Figure 2.4, which can only be explained by fragmentation of the [M]⁺⁺ and [M + H]⁺ ions formed by ionization of the intact AHPA.

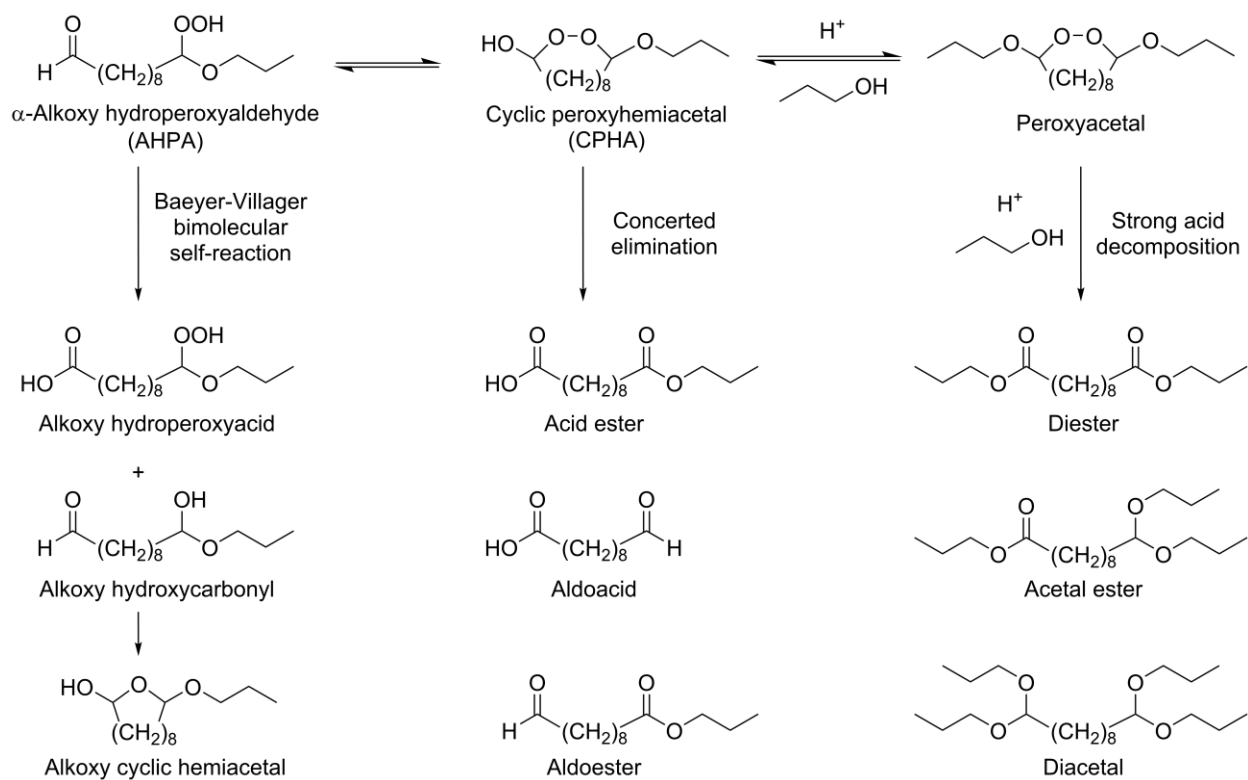


Figure 2.3. Potential reactions of AHPA in SOA. In the concerted elimination and strong acid decomposition pathways H_2 , water, and propanol co-products are not shown.

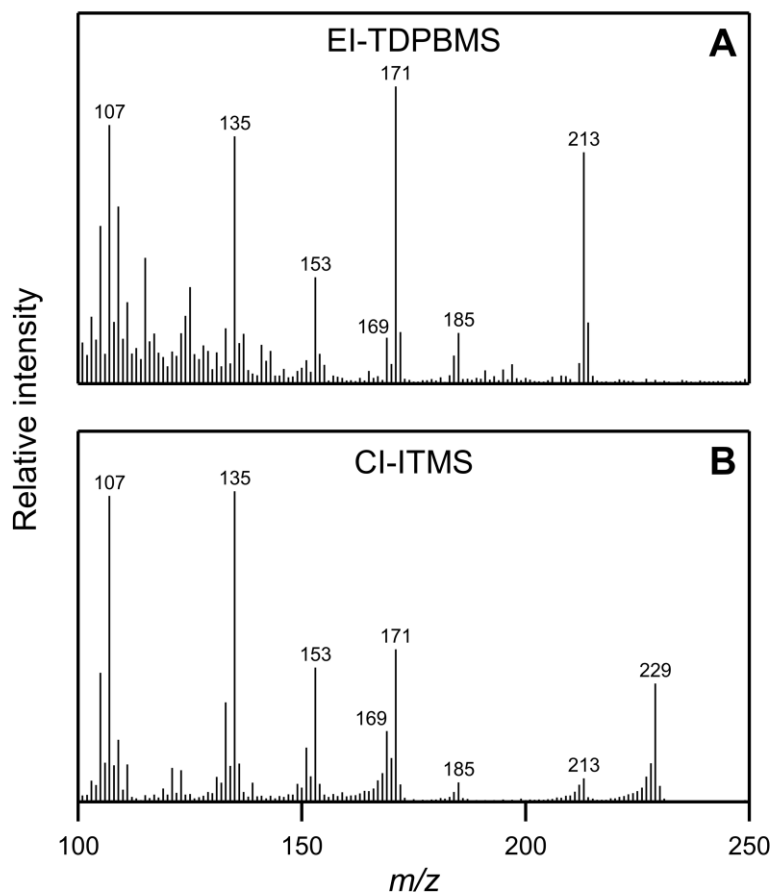


Figure 2.4. Mass spectra of AHPA standard obtained via EI-TDPBMS and CI-ITMS.

Since relatively little is known about the reactions of hydroperoxides in SOA beyond peroxyhemiacetal formation, and since CPHA have structures similar to the cyclic hemiacetals (CHA) formed in SOA from cyclization of 1,4-hydroxycarbonyls (Aimanant and Ziemann 2013b; Ranney and Ziemann 2016), we have looked to the chemistry of 1,4-hydroxycarbonyls and to the synthetic organic chemistry literature to develop a more complete scheme for describing the potential fate of AHPA.

After 1,4-hydroxycarbonyls cyclize to form CHA they can undergo dehydration to form dihydrofurans, or oligomerization in which CHA undergo self-reactions to form acetals

(Aimanant and Ziemann 2013b). Studies conducted on CHA in dry SOA in the presence of added HNO₃ showed that the dehydration of CHA is catalyzed by undissociated molecular HNO₃ (general acid catalysis) (Ranney and Ziemann 2016), whereas acetal formation is apparently catalyzed by H⁺ (specific acid catalysis) (Ziemann and Atkinson 2012). On the basis of these studies, CPHA is expected to undergo either dehydration or reaction with 1-propanol to form a peroxyacetal. 1-Propanol is shown as the reacting alcohol in Figure 2.3 because its mixing ratio in the chamber (1500 ppm to ensure high-efficiency scavenging of SCI) was so high that it provided a controlled source of hydroxyl groups for particle-phase reactions. Knowing the identity of the reacting alcohol in the SOA facilitated the identification of products of accretion reactions.

Two studies of the decomposition of organic hydroperoxides in the presence of aldehydes (Durham, Wurster, and Mosher 1958) and strong acid (Griesbaum and Neumeister, 1982) reported in the synthetic organic chemistry literature are also relevant to the current work, even though they were conducted in bulk solutions instead of SOA. In particular, they are informative since they establish that AHPA cyclize to CPHA, and they point to the importance of peroxyhemiacetals as key intermediates in decomposition reactions. In their study of the decomposition of *n*-butyl hydroperoxide in the presence of butanal, Durham, Wurster and Mosher (1958) observed a high yield (0.52) of gaseous H₂, and experiments with deuterated peroxide showed that the source of H₂ was the alkyl chains of the hydroperoxide and aldehyde. The primary products in solution were butyric acid, butyraldehyde, butyl butyrate, butyl alcohol, and a small amount of butyl formate, indicating that decomposition did not proceed by a single pathway under these conditions. And when Griesbaum and Neumeister (1982) investigated the decomposition of 6-methoxy-6-hydroperoxyhexanal (an AHPA similar to ours) in methanol in

the presence of strong acid, they observed a 1:2:1 yield ratio of diester, acetal ester, and diacetal, and proposed a simpler decomposition mechanism in which a peroxyacetal intermediate decomposed to give these products. These results have been incorporated into Figure 2.3 as the concerted elimination and strong acid decomposition pathways for CHPA, respectively. Knowing then that CPHA and peroxyacetals are likely to be key intermediates in AHPA decomposition in SOA, we set out to characterize the cyclization reaction of AHPA and identify decomposition products with and without strong acid present to determine which of these pathways are likely applicable to HOMs.

2.3.4. Mass Spectra of AHPA Standards. Mass spectra of the AHPA ($M = 246$) standard acquired using EI-TDPBMS and CI-ITMS are shown in Figure 2.4. The electron ionization fragmentation pattern has been established previously (Ziemann 2003), with dominant peaks at m/z 213 and 171. Under chemical ionization conditions the AHPA shows a similar fragmentation pattern, but with an additional peak at m/z 229. These fragmentation pathways are described further in Table 2.1.

Table 2.1. Characteristic ions and fragmentation pathways for major products in SOA analyzed by EI-TDPBMS and CI-ITMS.

Compound	Structure	M	EI-TDPBMS [M] ⁺⁺		CI-ITMS [M + H] ⁺	
			Neutral loss	<i>m/z</i>	Neutral loss	<i>m/z</i>
AHPA		246	HO ₂	213	H ₂ O	229
			HO ₂ + C ₃ H ₆	171	H ₂ O ₂	213
			HO ₂ + C ₃ H ₇ OH	153	H ₂ O ₂ + C ₃ H ₆	171
					H ₂ O ₂ + C ₃ H ₇ OH	153
CPHA		246	OH	229		
			OH + C ₃ H ₇ OH	169		
Diester		286				287
			C ₃ H ₆	245		
			C ₃ H ₇ O	227	C ₃ H ₇ OH	227
			C ₃ H ₇ O + C ₃ H ₆	185	C ₃ H ₇ OH + C ₃ H ₆	185
Acetal ester		330	C ₃ H ₇ O	271	C ₃ H ₇ OH	271
			C ₃ H ₇ O + C ₃ H ₆	229	C ₃ H ₇ OH + C ₃ H ₆	229
			α-cleavage	131		
			α-cleavage + C ₃ H ₆	89		
Diacetal		374	C ₃ H ₇ O + C ₃ H ₇ OH	255		
			α-cleavage	131		
			α-cleavage + C ₃ H ₆	89		

2.3.5. Rate and Equilibrium Constants for AHPA Cyclization. Rate and equilibrium constants for cyclization of hydroperoxyaldehydes have not been previously reported, and SOA models (Capouet et al. 2008) have only included peroxyhemiacetal formation from bimolecular reactions using values obtained from measurements conducted in bulk solutions (Antonovskii and Terent'ev 1967). In an effort to gain more quantitative information on this reaction, the formation of AHPA and cyclization to CPHA in SOA produced in the environmental chamber from the reaction of cyclodecene with O₃ in the presence of 1-propanol and DOS seed particles were monitored using the EI-TDPBMS signals at *m/z* 169 and 171, which are characteristic ions formed by electron ionization of CPHA and AHPA, respectively (Ziemann 2003). A plot of the

ratio of these signals is shown in Figure 2.5, with the ratio reaching an equilibrium plateau at ~10 min. An exponential fit to this profile yields a timescale to reach equilibrium of $\tau_{eq} = 2.7$ min. In addition, an equilibrium constant of $K_{eq} = 2.6$ was calculated for the reaction from Equation 2.1:

$$K_{eq} = \frac{[CPHA]_{eq}}{[AHPA]_{eq}} = \frac{[AHPA + CPHA]_{eq} - [AHPA]_{eq}}{[AHPA]_{eq}} \quad (2.1)$$

where $[AHPA]_{eq}$, $[CPHA]_{eq}$, and $[AHPA + CPHA]_{eq}$ are the concentrations of AHPA, CPHA, and AHPA + CPHA in the SOA at equilibrium. $[AHPA]_{eq}$ was determined from the m/z 171 signal at the plateau using the calibration procedure described above, and $[AHPA + CPHA]_{eq}$ was determined from offline peroxide analysis and the ratio of the AHPA molar yield/total peroxide molar yield of 0.12/0.18 reported above using Equation 2.2:

$$[AHPA + CPHA]_{eq} = [Total\ peroxide] \times \frac{0.12}{0.18} \quad (2.2)$$

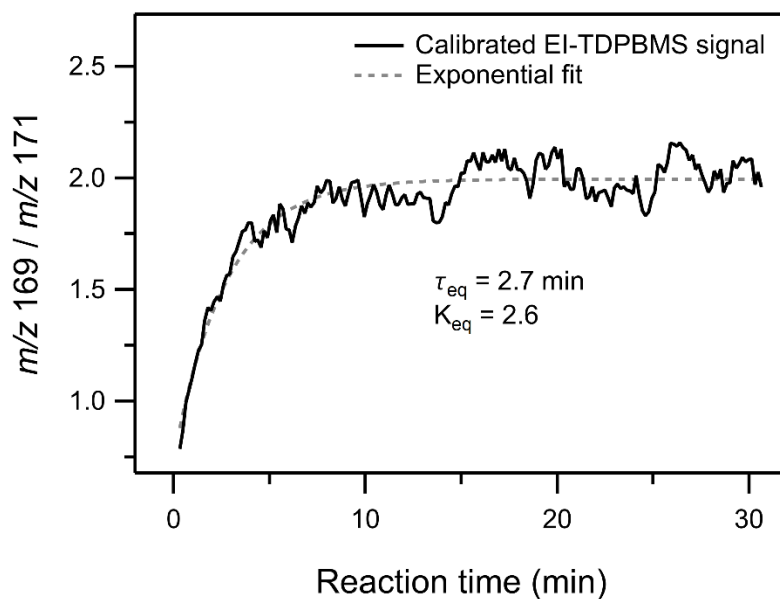
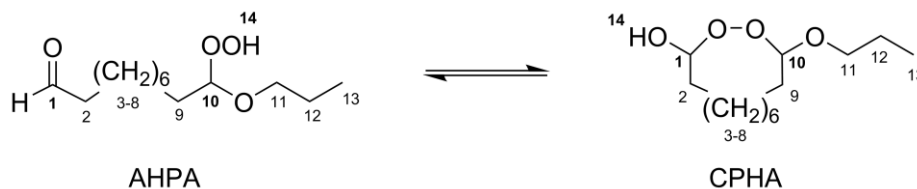


Figure 2.5. Time profile of the ratio of real-time EI-TDPBMS mass spectral signals measured at peaks characteristic of CPHA (m/z 169) and AHPA (m/z 171) in SOA formed from reaction of cyclodecene with O_3 in the presence of 1-propanol and DOS seed particles. The data were fit to an exponential function to determine the timescale to establish cyclization equilibrium (τ_{eq}) and the equilibrium constant (K_{eq}).

We also measured a similar equilibrium constant of 2.8 for the cyclization of AHPA in d_6 -DMSO using $^1\text{H-NMR}$. Peak shifts, areas, and assignments are presented below in Table 2.2. We normalize all peaks using the methyl triplet at 0.87 ppm, since the peak is large, isolated, and straightforward to assign. All peak splitting is consistent with assignments in Table 2.2, with long-range splitting observed across the alcohol and propoxy oxygens, giving rise to a doublet of multiplets, a doublet of triplets, and a quintet for assignments 11, CHPA 1, and CPHA 10, respectively. The methylene hydrogens (2-9, 11-12) and the methyl hydrogens (13) do not undergo any significant change in chemical environment upon cyclization, and so they each give an integrated area of ~ 1 . We observe that three peaks in AHPA undergo a change in chemical environment upon cyclization to CPHA: the aldehydic hydrogen (1), the hydroperoxide hydrogen (14), and the hydrogen bonded to the hydroperoxide carbon (10). Since $^1\text{H-NMR}$ peak areas are quantitative, we can use the average integrated areas of the peaks assigned to AHPA and CPHA to determine the relative concentration of each species and calculate the equilibrium constant using Equation 2.1.

Table 2.2. Peak shifts and assignments for $^1\text{H-NMR}$ spectrum of AHPA-CPHA equilibrium. Molecular structures with assignment labels are included to show which protons undergo a change in chemical environment following the cyclization reaction (depicted in bold).

δ (ppm)	Area	Multiplicity	Assignment
0.87	3.00 ^a	3	CH ₃ : 13
1.24	11.71	m	CH ₂ : 3-8
1.50	6.18	m	CH ₂ : 2, 9, 12
3.57	1.96	2 × m ^b	CH ₂ -OR: 11
4.69	0.26	3	HOO-CH-OR: AHPA 10
4.88	0.69	2 × 3	ROO-CH-OH: CPHA 1
5.02	0.66	5	ROO-CH-OR: CPHA 10
6.43	0.65	2	ROH: CPHA 14
9.66	0.22	3	C(O)H: AHPA 1
11.44	0.24	1	ROOH: AHPA 14



^a Used for area normalization.

^b Doublet of multiplets.

Taking the values presented in Figure 2.5, the rate constants for the cyclization (k_f) and ring-opening reactions (k_r) were then calculated from $\tau_{eq} = 2.7$ min and $K_{eq} = 2.6$ to be $k_f = 4.4 \times 10^{-3} \text{ s}^{-1}$ and $k_r = 1.7 \times 10^{-3} \text{ s}^{-1}$ using Equations 2.3 and 2.4 (Schwarzenbach, Gschwend, and Imboden 2003):

$$K_{eq} = \frac{k_f}{k_r} \quad (2.3)$$

$$\tau_{eq} = \frac{1}{k_f + k_r} \quad (2.4)$$

This measured timescale of ~ 3 min for cyclization can be compared with values expected for particle-phase bimolecular reactions. From experiments conducted with tert-butyl hydroperoxide (a tertiary hydroperoxide with a structure most similar to the secondary

hydroperoxide used here) and acetaldehyde in different solvents, Antonovskii and Terent'ev (1967) report a range of room temperature rate constants of 1.2×10^{-2} to $1.3 \times 10^{-4} \text{ M}^{-1} \text{ s}^{-1}$ for bimolecular peroxyhemiacetal formation and 2.0×10^{-4} to $8.3 \times 10^{-5} \text{ s}^{-1}$ for the reverse reaction.

These rate constants were used in kinetic simulations conducted in KinSim v3.1 (Peng et al. 2015) with the following quantities to give a range of timescales for establishing equilibrium of about 6 to 80 min: initial concentrations of hydroperoxide and aldehyde groups of 2 M (estimated assuming an SOA density of 1.2 g cm^{-3}), an average SOA molecular weight of 250 g mol^{-1} (calculated from the results of the functional group analysis (Aimanant and Ziemann 2013a)), and a mole fraction of AHPA in the SOA of 0.43 (calculated from the product of the molar yields of AHPA (0.12) and SOA (0.36), with the latter value calculated as (mass of SOA/molecular weight of SOA)/moles of cyclodecene reacted). Cyclization is faster than all of these reactions, probably because unimolecular reactions do not have the same unfavorable loss of entropy as bimolecular reactions (Bruckner 2002). The rates of both cyclization and oligomer formation could be increased by the presence of a strong acid catalyst, but this also affects rates of decomposition reactions as discussed below.

2.3.6. Peroxide Decomposition. Prior to investigating the decomposition of peroxides present in SOA, the possible effects of filter sampling, extraction, and weighing on their stability was determined by atomizing synthesized AHPA (purity $\geq 95\%$) onto a PTFE filter, extracting the AHPA in ethyl acetate, and measuring the mass and peroxide content of the extract. Comparison of the extracted moles of AHPA based on measured SOA mass (moles AHPA = SOA mass/AHPA molecular weight) and measured peroxide (moles AHPA = moles peroxide) showed that the sample was still $\geq 95\%$ AHPA, indicating that filter collection and extraction did

not contribute to the peroxide decomposition reported here for SOA. In addition, filter mass was stable over the 3 min required to take replicate measurements on the microbalance.

The rate of decomposition of AHPA (and other peroxides present in smaller amounts) was then measured for SOA formed under the following three conditions: DOS seed particles at ~0% RH, DOS/sulfuric acid seed particles at ~0% RH, and aqueous ammonium sulfate/sulfuric acid seed particles at pH ~ 1 and 50% RH, which is typical of atmospheric conditions (Guo et al. 2015; Guo et al. 2017). After SOA formation, 3–6 filter samples were collected at different intervals over a period of ~4 h, extracted, and analyzed immediately for peroxide content. We note that no nucleation was observed in any experiment with seed aerosol, and that functional group analysis of experiments without seed aerosol gave the same results as those using dry DOS seed. Furthermore, the SOA mass concentration in the chamber was constant after correcting for particle wall loss, indicating that no significant particle evaporation occurred during the experiments.

The results of the peroxide decomposition measurements are shown in Figure 2.6, where the number of moles of SOA was calculated from the SOA mass and the average SOA molecular weight of 250 g mol⁻¹. Under dry conditions with inert DOS seed particles the decomposition rate was 17% hour⁻¹. This is similar to the rates of 13% h⁻¹ and 15% h⁻¹ measured by Mertes et al. (2012) and Krapf et al. (2016) for SOA formed from α -pinene ozonolysis. Despite the differences in peroxide structure and SOA composition, the emerging trend is that organic peroxides in SOA decompose within a few hours when there are no strong acids present. In experiments conducted with seed particles containing sulfuric acid, the effect of the sulfuric acid on peroxide decomposition varied with the type of particles used. In experiments using dry DOS/sulfuric acid seed particles the peroxide content of the SOA had fallen to almost zero by the

time a filter sample could be collected after 30 min of reaction (Figure 2.6), indicating a timescale less than ~10 min. When aqueous ammonium sulfate/sulfuric acid seed particles were used, however, the peroxide decomposition rate was similar to that for dry DOS seed particles without added acid.

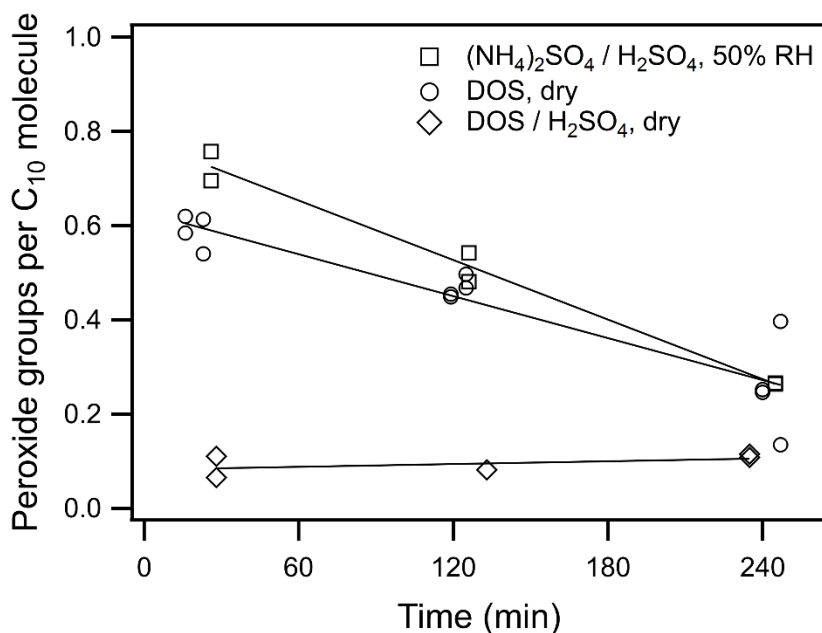


Figure 2.6. Time profiles of peroxide functional group content of SOA formed from the reaction of cyclodecene with O₃ in the presence of 1-propanol and seed particles with the following composition: (squares) aqueous ammonium sulfate/sulfuric acid at 50% RH and pH = 1, (circles) dry DOS, and (diamonds) dry DOS/sulfuric acid.

We attribute the difference in decomposition observed with dry DOS/sulfuric acid and aqueous ammonium sulfate/sulfuric acid seed particles to the phase state of the particles and its effect on partitioning of sulfuric acid. The parameterization of Bertram et al. (2011) shows that SOA with an O/C ratio of 0.3 (calculated from the functional group composition) and an ammonium sulfate component will exhibit liquid-liquid phase separation between the organic and aqueous phases below 95% RH. The experiments in this work using aqueous ammonium sulfate/sulfuric acid seed particles were conducted at 50% RH, so we expect two phases to be

present when AHPA SOA condenses onto the seed particles. Although the morphology of these phase-separated particles is unknown, for organic aerosol with an average molecular weight of 250 g mol^{-1} and no oligomers, the estimated timescale for a molecule to diffuse through a particle of the size generated in these experiments is $\sim 1 \text{ ms}$ (Docherty and Ziemann, 2006). Since this timescale is much shorter than the observed timescale for peroxide decomposition ($\sim 6 \text{ h}$), the organic phase is likely well-mixed during peroxide decomposition regardless of morphology. Furthermore, although published research investigating the partitioning of sulfuric acid between aqueous and organic phases is sparse, one reported study (Hayes and Pepper, 1961) conducted with dichloroethane indicates that only a trace amount of undissociated molecular sulfuric acid partitions to the organic phase. This is consistent with our E-AIM (Wexler and Clegg 2002) calculations that show that 100% of the sulfuric acid is dissociated in the aqueous phase, making molecular sulfuric acid unavailable for partitioning to the organic SOA phase. Together these results suggest that sulfuric acid exists almost entirely in the aqueous phase in these experiments and so is probably not available to catalyze AHPA decomposition in the organic phase.

These results highlight the uncertain nature of acid catalysis in aerosol where there is little water or there is phase separation between organic and aqueous phases. Recent results showing that the pH range of ambient submicron aerosols is typically 0–4 assume that hygroscopic organic components are in the aqueous phase and contribute to total aerosol water uptake (Guo et al. 2015; Guo et al. 2017). Our results indicate, however, that for phase-separated aerosol with low O/C ratios, such as AHPA, most of the acid remains in the aqueous phase and so is not available to catalyze reactions in the organic phase. Phase separation may thus create a potential barrier to acid catalysis in aerosol particles. In light of the results of Ranney and Ziemann (2016) that demonstrated occurrence of general acid catalysis by

undissociated molecular nitric acid in dry organic aerosol, it seems plausible that the acid-catalyzed decomposition that we observe in dry aerosol using organic seed is general acid catalysis by undissociated molecular sulfuric acid. The mechanisms of general acid catalysis in concentrated solutions are well documented, with prior studies of the acid-catalyzed hydration of alkenes and acid-catalyzed dehydration of alcohols showing that these reactions can proceed through a wide variety of general acid catalysis mechanisms, depending on the identity and concentration of the acid catalyst and the properties of the solvent (Vinnik and Obraztsov, 1990). It seems likely, therefore, that acid catalysis in aerosols proceeds by different mechanisms in different aerosol phases, and that the mechanisms of reaction will vary with aerosol phase and humidity.

2.3.7. Identification of Peroxide Decomposition Products. Using the EI-TDPBMS and CI-ITMS mass spectra, functional group composition, and potential reaction pathways outlined above as guides, we have identified several decomposition products of AHPA. The structure, molecular weight, characteristic ions, and EI and CI fragmentation pathways for all the major identified reaction products are shown in Table 2.1. Figure 2.7 shows real-time EI-TDPBMS spectra of the SOA formed in the absence and presence of sulfuric acid and humidity. Figure 2.7A shows the mass spectrum immediately following SOA formation on dry DOS seed particles in the absence of sulfuric acid and Figure 2.7B shows the mass spectrum of this SOA after 4 h of peroxide decomposition. Most notable is the similarity of the two mass spectra. Whereas we attribute the peaks at m/z 213 and 171 in Figure 2.7A to AHPA, and m/z 229 and 169 to CPHA (Ziemann, 2003), their presence in Figure 2.7B must also be due to other compounds since we know from functional group analysis that ~60% of the peroxides have decomposed within 4 h (Figure 2.6). Products that are expected to have peaks at m/z 229, 213, 171, and 169 could be

formed from a bimolecular Baeyer-Villager reaction (Wurster, Durham, and Mosher 1958) between two AHPA, which are present in significant amounts ($[AHPA]_{eq}/[CPHA]_{eq} \sim 0.4$) after rapid equilibration with CPHA. In this reaction, a hydroperoxide group in one AHPA oxidizes the carbonyl group of another AHPA to a carboxyl group and in the process is reduced to a hydroxyl group (Figure 2.3). The resulting products are an alkoxy hydroperoxyacid and alkoxy hydroxycarbonyl, with the latter compound rapidly cyclizing to an alkoxy cyclic hemiacetal (Ranney and Ziemann 2016). They should undergo EI fragmentation by pathways similar to those of AHPA and CHPA (Ziemann, 2003) to form ions at m/z 229, 213, 171, and m/z 169. It is also likely that over the 4 h period of peroxide decomposition that the peroxyacetal is formed (Figure 2.3) in significant amounts and contributes to the m/z 229 and 169 peaks by fragmentation pathways similar to the CPHA.

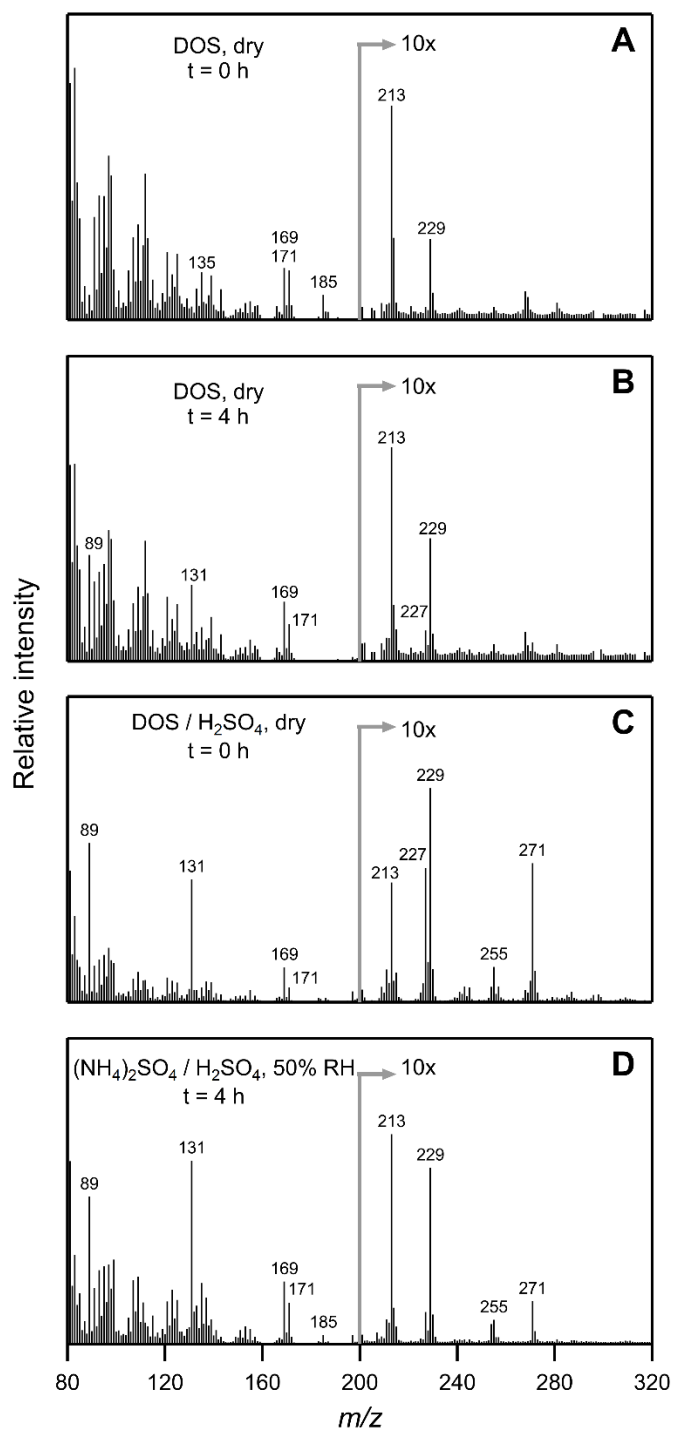


Figure 2.7. Real-time EI-TDPBMS mass spectra measured at different times for SOA formed from the reaction of cyclodecene with O₃ in the presence of 1-propanol and seed particles with different compositions as follows: (A) immediately after formation on dry DOS, (B) 4 h after formation on dry DOS, (C) immediately after formation on dry DOS/sulfuric acid, and (D) 4 h after formation on aqueous ammonium sulfate/sulfuric acid at 50% RH and pH = 1.

When real-time EI-TDPBMS mass spectra were taken as SOA peroxides decomposed (Figure 2.7B-D), peaks at m/z 131 and 89 and increased with time regardless of the absence or presence of sulfuric acid or humidity. These peaks were observed as a pair in all instances, and are characteristic of α -cleavage of dipropoxy acetals (Borisova et al. 1981; Friedel and Sharkey 1956). Several reference spectra of dipropoxy acetals are also available in the NIST Chemistry WebBook and the AIST Spectral Database that display peaks at m/z 89 and 131, and these are shown in Figure 2.8 (Stein 2016; SDBSWeb 2017). The acetal ester and diacetal shown in Figure 2.3 (2 of the 3 products of peroxyacetal decomposition), are the likely source of these peaks. Formation of the acetal ester, diacetal, and diester are consistent with the peaks at m/z 271, 255, and 227, respectively, in Figure 2.7C and Figure 2.7D (McLafferty 2012).

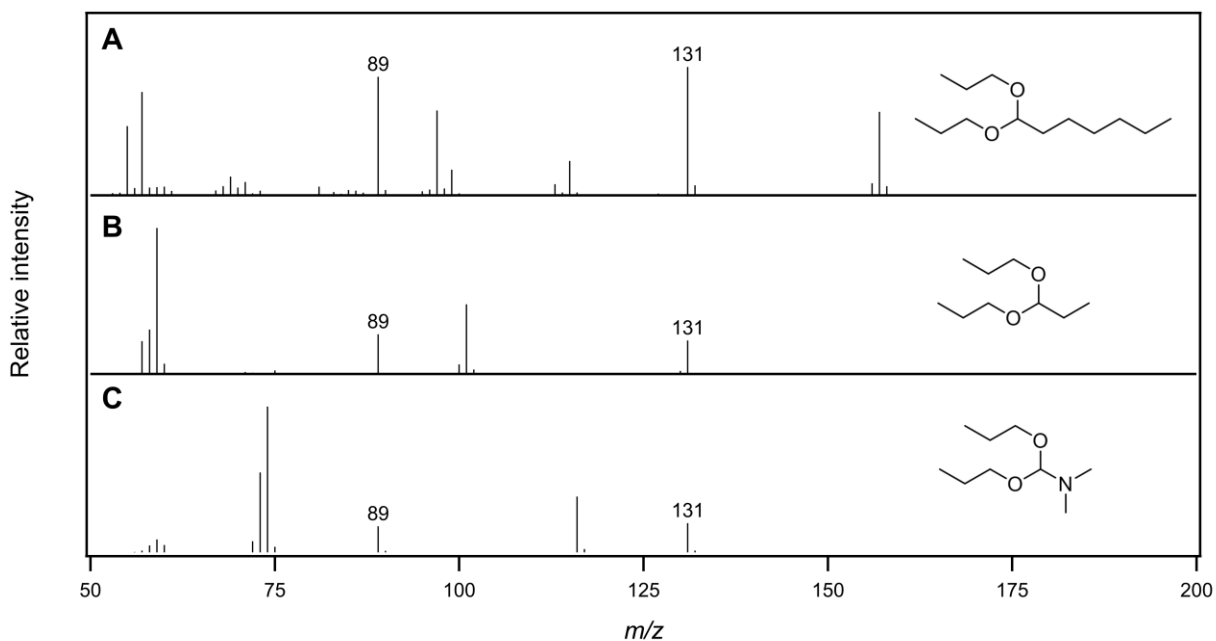


Figure 2.8. Reference EI spectra of dipropoxy acetals: 1,1-dipropoxyheptane (A), 1,1-dipropoxypropane (B), and 1,1-dipropoxytrimethylamine (C) (Stein 2016; SDBSWeb, 2017). The characteristic fragmentation pattern is α -cleavage at the acetal carbon (m/z 131) followed by neutral loss of propene (m/z 89).

Further evidence of the formation of peroxyacetals and subsequent decomposition to the acetal ester and diester are seen in the CI-ITMS mass spectra in Figure 2.9 of SOA formed in the absence (Figure 2.9A and Figure 2.9B) and presence (Figure 2.9C) of dry sulfuric acid seed particles. Looking first at Figure 2.9C, ionization of the acetal ester should create an $[M + H]^+$ ion that fragments to form m/z 271 and 229 ions that are characteristic of acetals (Lin, Tien, and Chang 1989; Borisova et al. 1981). Evidence for the diester was obtained by comparing the mass spectrum with that of *bis*-diethylhexyl sebacate (DOS), a sebacate diester standard, for which we observed a $[M + H]^+$ peak along with peaks corresponding to losses of an alkene, alcohol, and both simultaneously, from the alkyl substituents. The corresponding peaks for the diester are m/z 287, 245, 227, and 185, all of which are intense in the mass spectrum. Peaks from the acetal ester and (to a lesser extent) the diester are also present in mass spectra of the SOA formed and aged in the absence of sulfuric acid seed particles (Figure 2.9A and Figure 2.9B), though they are less intense due to the reduced decomposition of peroxides. In the mass spectra in Figure 2.9B and Figure 2.9C it is likely that the CPHA and peroxyacetal, which are precursors to acetal ester and diester formation, also contribute to the m/z 229 and 169 and peaks. The formation of the acetal ester, diester, and diacetal products is consistent with the mechanism proposed by Griesbaum and Neumeister (1982), but only the real-time EI-TDPBMS mass spectrum provides plausible evidence for the formation of the diacetal that they propose. It is possible that peaks due to the diacetal are absent in the CI-ITMS mass spectrum because of ion suppression by the esters, which is a phenomenon we have observed in some analyses. The presence of the acid ester, aldoacid, and aldoester products of CPHA decomposition (Figure 2.3) cannot be verified from the mass spectra, since their dominant peaks in EI-TDPBMS and CI-ITMS analysis are likely to

be m/z 185 and or 169, which overlap with peaks assigned to fragmentation of other products that are more definitively identified from characteristic high-mass peaks.

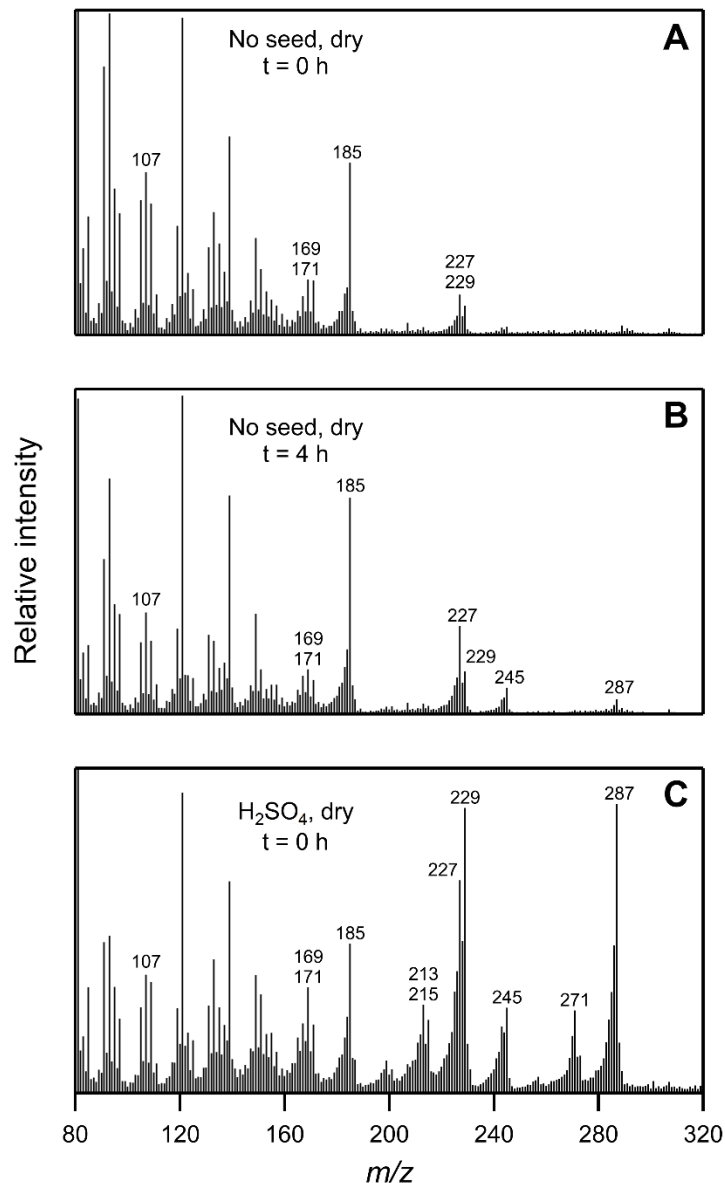


Figure 2.9. CI-ITMS mass spectra of filter extracts of SOA collected at different times from the reaction of cyclodecene with O_3 in the presence of 1-propanol in the absence or presence of seed particles as follows: (A) immediately after formation in the absence of seed particles, (B) 4 h after formation in the absence of seed particles, and (C) immediately after formation on dry sulfuric acid seed particles. DOS seed particles were not used in these experiments because DOS is the dominant signal in CI-ITMS at the concentrations used in chamber experiments.

The formation of the acetal ester, diester, and diacetal from decomposition of the peroxyacetal is also supported by the results of SOA functional group analysis presented in Table 2.3. By comparing the functional group composition of SOA produced in the presence of CO (which does not include products formed by the SCI pathway) to that produced in the presence of 1-propanol (which includes the same products as in the CO experiment plus AHPA formed by the SCI pathway) and sulfuric acid seed aerosol (which leads to rapid peroxide decomposition), one can infer the functionality of the products of peroxyacetal decomposition since they are formed from AHPA. Complications can occur in the interpretation of functional group analyses when significant amounts of peroxides decompose during an analysis, which is why we do not present results for experiments where significant amounts of AHPA are still present. For the two experiments presented in Table 2.3 that was not an issue since almost no peroxide was present in either SOA. The greater yield of ester (0.20 compared to 0.10) and carbonyl (0.47 compared to 0.20) groups in the SOA formed in the presence of 1-propanol and sulfuric acid is indicative of the formation of the acetal ester, diester, and diacetal, since during carbonyl analysis acetals are hydrolyzed to form carbonyl (and hydroxyl) groups, and these carbonyl groups are then derivatized and contribute to the measured carbonyl content. The higher SOA molar yield for that experiment (0.36 compared to 0.19), which is close to the sum of the yields (0.31) for the CO experiment (0.19) and AHPA (0.12), is also to be expected since AHPA is the sole product of the SCI reaction with 1-propanol and is the precursor to the peroxyacetal. The observed lower yield of carboxyl groups (0.14 compared to 0.18) is not as easily explained, but is possibly due to particle-phase reactions of oxoacids and hydroxyacids in the aerosol. These compounds comprise a significant fraction of SOA produced from cycloalkene ozonolysis (Gao et al. 2004), and could have undergone acid-catalyzed cyclization to form more volatile hydroxylactones and cyclic

esters that evaporated from the aerosol and so lowered the yield of carboxyl groups. The consistency of the functional group analysis results (which are obtained without use of high temperatures) with the products of AHPA decomposition identified using EI-TDPBMS and CI-ITMS give us confidence that the high temperatures used to vaporize SOA in those instruments did not introduce significant artifacts in our results. It is also worth noting that the occurrence of peroxide decomposition in the presence of either DOS or DOS/sulfuric acid seed particles suggests that a strong acid is not necessary to catalyze this process. For example, from EI-TDPBMS mass spectra (Figure 2.10) we identified sebacic acid as a major component of the SOA produced by a non-SCI pathway, and it is possible that organic acids such as this are able to catalyze CHPA and peroxyacetal decomposition. The larger decrease in the amount of peroxide groups and larger increase in the amounts of carbonyl and ester groups and the peaks at m/z 89 and 131 in EI-TDPBMS mass spectra, in experiments when sulfuric acid seed was present, indicate that sulfuric acid is more efficient than organic acids at catalyzing peroxide decomposition.

Table 2.3. Molar yields of functional groups in SOA formed in the presence of CO without seed particles or 1-propanol with sulfuric acid seed particles.

Functional group ^a	Molar yield	
	CO no seed	1-Propanol sulfuric acid seed
Carbonyl	0.20	0.47
Carboxyl	0.18	0.14
Ester	0.10	0.20
Peroxide	0.06	0.03
SOA ^b	0.19	0.36

^aCalculated from the measured moles of each functional group in SOA/moles of cyclodecene reacted.

^bCalculated as (mass of SOA/molecular weight of SOA)/moles of cyclodecene reacted.

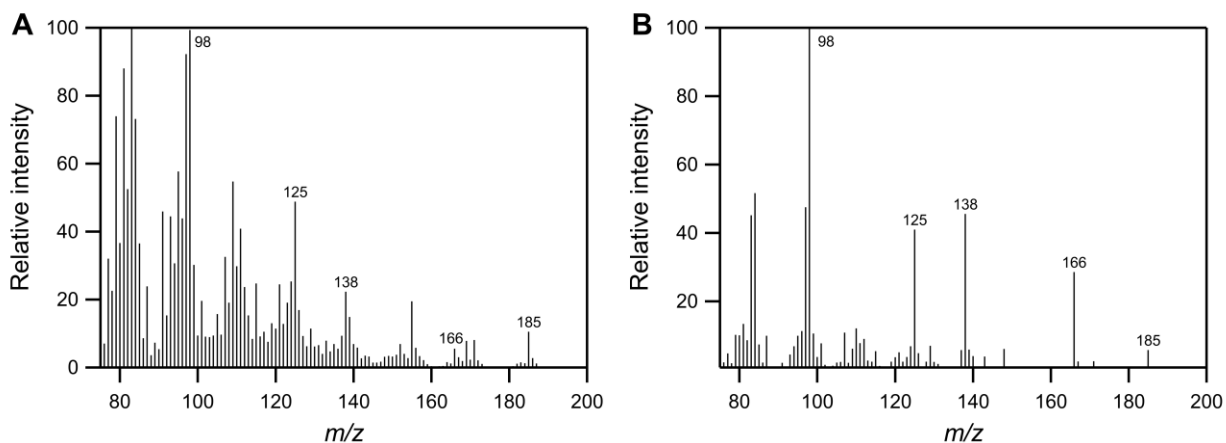


Figure 2.10. EI-TDPBMS spectrum of SOA produced from ozonolysis of cyclodecene in the presence of a large excess of carbon monoxide (A). NIST reference spectrum of sebacic acid (B) (Stein, 2016).

2.3.8. Particle Phase Alcohol and Water Exchange Reactions. Since the decomposition products identified above are oligomers formed from reactions involving the most abundant alcohol in the SOA (1-propanol), understanding the reactions between CPHA and alcohols in SOA is central to understanding how HOMs will react with alcohols in atmospheric aerosol. To explore this question, an environmental chamber experiment was conducted to probe the exchange of alkoxy groups in SOA products due to competition with other alcohols or water. After forming SOA from the reaction of cyclodecene with O₃ in the presence of 1-propanol and dry DOS/sulfuric acid seed particles, ~4000 ppm of methanol was added to the chamber, and then ~6000 ppm of water (18% RH). As shown in Figure 2.11, upon addition of methanol peaks at *m/z* 103 and 75 grew in relative to that at *m/z* 131 due to exchange of one and then two propoxy groups for methoxy groups in the acetal ester and diacetal. High-mass peaks at *m/z* 243, 227, and 201 also grew in relative to those at *m/z* 271, 255, and 229 due to these exchange reactions, but since fragmentation of the acetal ester and diacetal occur by loss of alcohols, alkenes, and alkoxy radicals, changes in high-mass peaks did not provide information beyond the exchange of one methoxy and propoxy group. When water was then added, peaks at *m/z* 131, 103, 89, and 75 all decreased significantly, due to exchange of methoxy and propoxy for hydroxyl groups. Although the relative intensities of some of the high-mass peaks also changed, no significant new peaks grew in. This is probably due to dissociation of the hemiacetal and gemdiol products to aldehydes, alcohols, and water that then evaporated from the particles because of their high volatility.

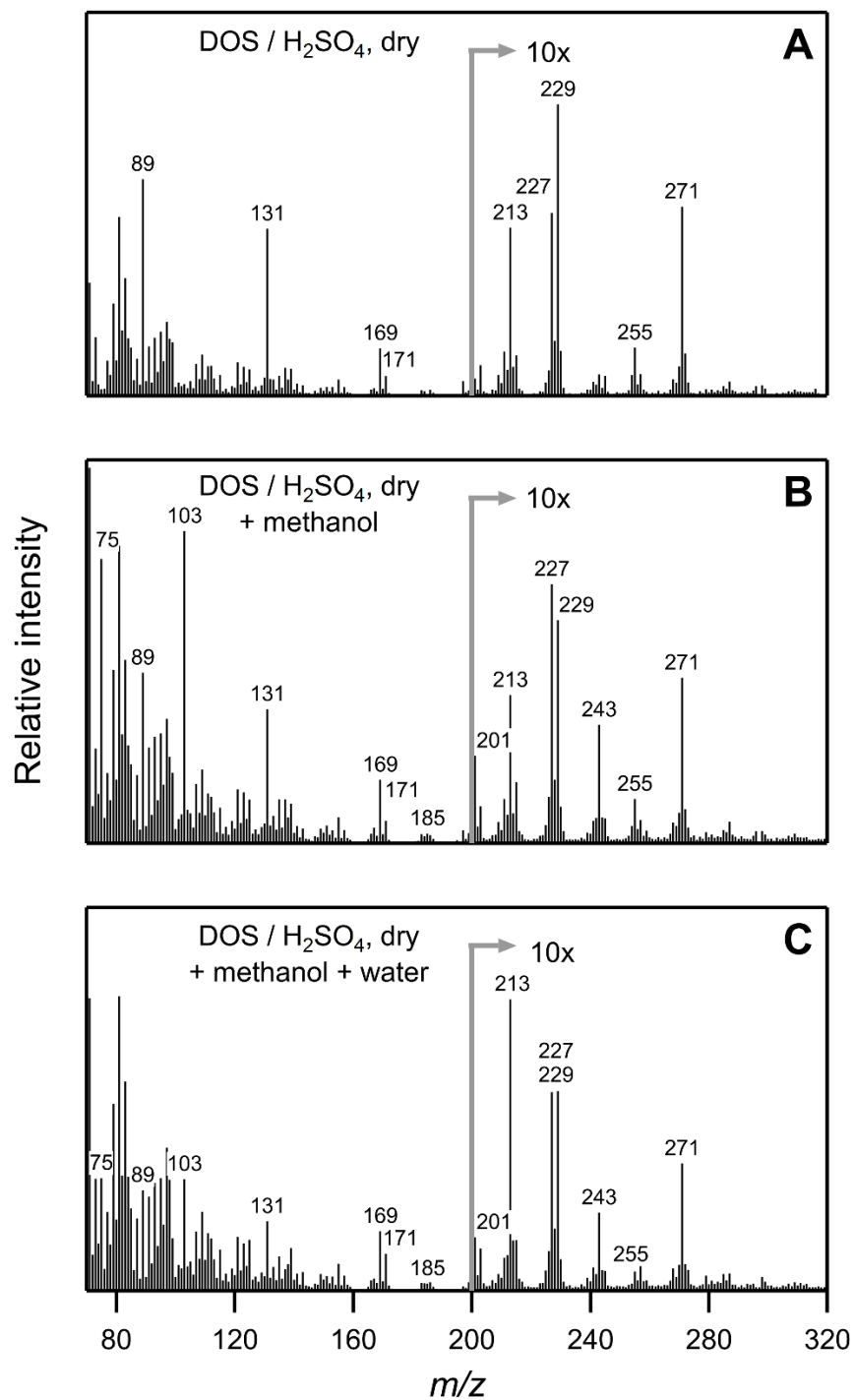


Figure 2.11. Real-time EI-TDPBMS mass spectra of (A) SOA formed from the reaction of cyclodecene with O₃ in the presence of 1-propanol and dry DOS/sulfuric acid seed particles, and with the subsequent addition of (B) methanol, and then (C) water.

2.4. Conclusions

The results of this study provide new information on the potential influence of particle-phase chemistry on the atmospheric fate of hydroperoxycarbonyl compounds that can be formed under low-NO conditions, including HOMs that are formed through autoxidation reactions. Experiments conducted in an environmental chamber and in solution using a model α -alkoxy hydroperoxyaldehyde formed from the ozonolysis of cyclodecene in the presence of 1-propanol indicate that these compounds rapidly cyclize in particles to cyclic peroxyhemiacetals, reaching an ~3:1 equilibrium mixture of the cyclic and acyclic forms in ~3 min. Based on results of SOA mass spectral and functional group analysis we propose that a number of different reaction pathways then lead to cleavage of the O–O peroxide bond and formation of a variety of decomposition products. In particular, it appears that the α -alkoxy hydroperoxyaldehyde decomposes through a bimolecular Baeyer-Villiger self-reaction and that the cyclic peroxyhemiacetal either decomposes by a unimolecular reaction or first reacts with alcohol (in this case 1-propanol) to form a peroxyacetal that then undergoes unimolecular decomposition. In SOA formed in the absence of sulfuric acid or in particles apparently containing separate SOA and aqueous ammonium sulfate/sulfuric acid phases decomposition occurred on a timescale of ~4 h, similar to other reported studies, whereas in dry SOA containing sulfuric acid the timescale was at most ~10 min. These timescales are all significantly shorter than the 6-day peroxide photolysis lifetime measured for SOA produced from α -pinene ozonolysis (Epstein, Blair, and Nizkorodov 2014), indicating that non-photolytic decomposition reactions of the type observed here are the dominant loss processes for hydroperoxycarbonyls in SOA. The fate of these compounds in the atmosphere should thus depend on the composition of the SOA, particle acidity, and relative humidity.

It is important to note here that because of differences in gas-phase reaction mechanisms hydroperoxycarbonyls formed in the atmosphere would most likely contain an alkyl group instead of the alkoxy group that is present in the model α -alkoxy hydroperoxyaldehyde, cyclic peroxyhemiacetal, and their decomposition products. Despite this difference, the consistency of our results with prior studies of rates (Mertes et al. 2012; Krapf et al. 2016) and products of decomposition of peroxyhemiacetals (Durham, Wurster, and Mosher 1958) leads us to believe that the decomposition pathways of a hydroperoxycarbonyl with an alkoxy substituent are similar to those of a hydroperoxycarbonyl with an alkyl substituent. The alkoxy hydroperoxyacid, alkoxy hydroxycarbonyl, alkoxy cyclic hemiacetal, acid ester, aldoacid, and aldoester decomposition products (Figure 2.3) would then become a hydroperoxyacid, hydroxycarbonyl, cyclic hemiacetal, ketoacid, and dicarbonyl (Figure 2.12). And for the peroxyacetal and its decomposition products one of the alkoxy groups would be replaced by an alkyl group, so that the diester, acetal ester, and diacetal would then become a ketoester, ketoacetal, hydroxyester, and hydroxyacetal (Figure 2.12). Furthermore, in the atmosphere the alkoxy groups in all these compounds would have been added by reactions with the large variety of low volatility multifunctional compounds containing hydroxyl groups (instead of 1-propanol) that are present in SOA, leading to the formation of much larger oligomeric compounds. These compounds would in turn be amenable to acid-catalyzed exchange reactions with other alcohols or water.

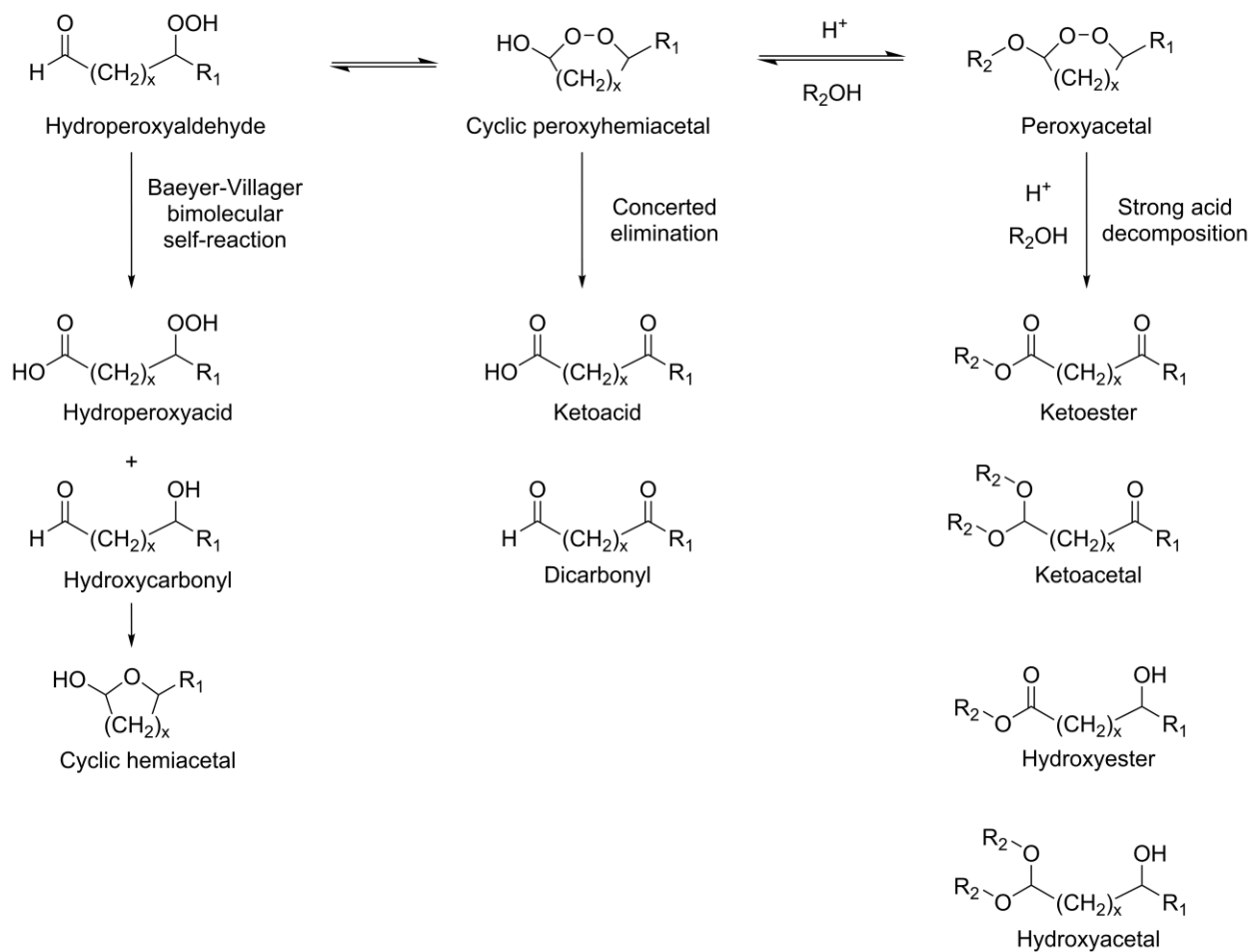


Figure 2.12. Potential reactions of hydroperoxyaldehydes in SOA. In the concerted elimination and strong acid decomposition pathways coproducts of hydrogen and water are not shown.

Chapter 3

Time-Resolved Measurements of Indoor Chemical Emission Rates, Deposition Velocities, and Reactions in a University Art Museum

3.1. Introduction

Online measurements of trace gases in the indoor environment have allowed for new insights into how pollutants are emitted, transported, and transformed through chemical reactions indoors. Measurements of volatile organic compounds (VOCs) in university classrooms using proton transfer reaction mass spectrometry (PTRMS) have allowed for quantitative source attribution of VOC emissions from occupants, ventilation, and surfaces (Liu et al. 2016), and determination of emission rates by occupants for a wide variety of VOCs (Tang et al. 2016). Use of high-resolution, time-of-flight chemical ionization mass spectrometers (CIMS) have allowed for novel source attributions of oxygenated semivolatile compounds (SVOCs) (Liu et al. 2017) and chlorinated emissions following application of cleaning products containing bleach (Wong et al. 2017). These studies have consistently documented a significant contribution of humans to indoor VOC concentrations, with human influence even being detectable in an open-air soccer stadium (Veres et al. 2013).

Even with these advances, significant questions remain surrounding the variability of emission profiles across different indoor environments as occupancy rates, construction materials, and activities undergone in the space being studied change. Additionally, broader changes in emissions (McDonald et al. 2018) are indicating that in some cities volatile chemical products (VCPs) are emerging as the dominant source of anthropogenic VOCs outdoors. These

emissions include personal care products, cleaning supplies, paints, and other compounds that are initially emitted indoors, and so characterizing the indoor emissions of these compounds is necessary to improve understanding of both indoor and outdoor air quality.

Many of the VCPs emitted indoors are SVOCs, and the fate of these compounds following their emission is not well understood. SVOCs undergo partitioning to indoor surfaces, partitioning to indoor particulate matter (Bennett and Furtaw, 2004; Weschler and Nazaroff, 2017), reactions with indoor oxidants such as O₃ and OH radicals (Weschler and Carslaw, 2018), and transport to the outdoor environment through heating, ventilation and cooling (HVAC) systems as well as through open windows and doors. Partitioning to indoor surfaces is an aspect of SVOC fate that is being actively researched. Models of impermeable indoor surfaces describe the formation of organic films on top of those surfaces by SVOCs with octanol-air partitioning coefficients below 10¹⁰ (Weschler and Nazaroff, 2017). The contribution of permeable indoor surfaces such as paints and plastics to indoor SVOC partitioning has received less attention, and these surfaces have the potential to be a significant indoor SVOC sink (Won et al. 2001). Additionally, water-soluble organic compounds are expected to be absorbed into films of surface water indoors (Duncan et al. 2017).

Recent research has also focused on the mechanisms by which indoor VOCs are oxidized. Indoor O₃ chemistry has received considerable attention, and recent measurements of indoor photolysis have indicated that OH radicals can also play a role in indoor VOC oxidation (Weschler and Carslaw, 2018). After the initiation of VOC oxidation by one of the oxidants mentioned above, most reactions proceed through the formation of an alkyl peroxy radical (RO₂•) intermediate (Orlando and Tyndall, 2012). A key factor in determining the products of VOC oxidation is the fate of these RO₂• radicals, specifically whether they react with another RO₂•

radical, a molecule of NO, an HO₂ radical, or through an intramolecular autoxidation reaction (Ziemann and Atkinson, 2012; Crouse et al. 2013). The products produced by each of these reaction pathways are chemically different, and these differences can impact the amount of secondary organic aerosol (SOA) formed from VOC oxidation. In polluted environments where NO concentrations are high, RO₂[•] radicals react primarily with NO, forming an alkoxy radical (RO[•]) and NO₂, a key step in the photochemical production of O₃. As NO emissions have declined, however, the rate of RO₂[•] reaction with NO has declined and the relative contribution of autoxidation reactions has increased (Praske et al. 2018). In autoxidation reactions, RO₂[•] radicals react intramolecularly to abstract a hydrogen, producing a hydroperoxy group and a new RO₂[•] radical at the site from which the hydrogen was abstracted. These reactions form highly oxidized multifunctional compounds (HOMs) that are particularly efficient in forming SOA, with HOMs comprising the majority of SOA produced in pristine environments (Ehn et al. 2014). With the reactions of RO₂[•] radicals being a key determinant of SOA and O₃ production, understanding the indoor fate of RO₂[•] radicals is central to understanding the transformation of pollutants indoors.

In this study we present results from six weeks of indoor measurements at a university art museum. We present emission rates from occupants consistent with the studies described above, emission rates of VCPs emitted from painting and other occupant activities, the volatility dependence of SVOC deposition to indoor surfaces, and what we believe are the first measurements of indoor HOMs produced through autoxidation. This work provides the most comprehensive picture to date of how indoor pollutants are emitted, transported, deposited, and chemically transformed in a single indoor setting, and these results will be particularly useful for improving models describing the chemistry of the indoor environment.

3.2. Materials and Methods

3.2.1. Art Museum Site. The art museum study of indoor chemistry (ARTISTIC) campaign was conducted from April 13th to May 23rd at the University of Colorado Art Museum (40.0072 deg. lat. -105.2701 deg. lon. 1,650 m above mean sea level). The museum has a volume of 6,000 m³ and is ventilated at a constant volume flow rate of 48,000 m³ hr⁻¹, with 4,800 m³ hr⁻¹ being outside air. The temperature and relative humidity (RH) of the museum are tightly controlled at constant values of 21 °C and 45%, respectively. From April 13th to May 9th we sampled from one of the museum's galleries ("the gallery", 780 m³, constant ventilation at 7,800 m³ hr⁻¹) that was exhibiting art by the university's students, and from May 9th to May 23rd measurements were conducted from the museum's collections room (1,400 m³, constant ventilation at 8,200 m³ hr⁻¹), where the university's permanent collections are stored.

3.2.2. Measurements and Instrumentation. VOCs were measured using a quadrupole proton transfer reaction mass spectrometer (PTR-MS) (de Gouw and Warneke, 2007), and more oxygenated organic compounds were measured using a high-resolution time-of-flight chemical ionization mass spectrometer that was operated using iodide (I-CIMS) or nitrate (NO₃-CIMS) as reagent ions (Bertram et al. 2011, Jokinen et al. 2012). Carbon dioxide, carbon monoxide, methane, and water were measured using a Picarro G2401 cavity ringdown spectrometer. Ozone, nitrogen oxides (NO_x) and sulfur dioxide (SO₂) were measured with a Thermo 49i O₃ analyser, Thermo 42i-TL NO_x analyser, and a Thermo 43i-TLE SO₂ analyser, respectively. Aerosol size distributions and mass concentration were measured with a TSI scanning mobility particle sizer (SMPS). Relative humidity and temperature were measured with a Vaisala RH probe. Zero air was generated on-site using a Thermo 1160 zero air generator. Photolysis rates were measured using an Ocean Optics USB 2000+ spectrometer, with calibration details presented below. Trace

gases were sampled through 0.47 cm inner diameter (ID) FEP Teflon tubing, and aerosols were sampled through 0.47 cm ID copper tubing. The NO₃-CIMS sampled through a 1.5 cm ID stainless steel tube 0.7 m in length.

In the gallery and collections rooms the instruments sampled air from inside each room and from the supply air from the HVAC system. The supply air was sampled after all conditioning had occurred, with the supply air sampling lines located immediately (< 30 cm) upstream of the diffusers where the supply air enters either room. The instruments sampled using an automated valve system that alternated sampling between room air and supply air every 5 min, with makeup flows applied so that air was being pulled through both sampling lines at all times. The valve timing was chosen to balance the ability to sample both air masses as frequently as possible after considering the delays in response times of the instruments and sampling lines to semivolatile organic compounds (SVOCs) (Pagonis et al. 2017). Because analytes detected by the NO₃-CIMS tend to show irreversible losses to the walls of the inlet tubing, and sampling from the supply air registers would have required prohibitively long sampling lines, the NO₃-CIMS only sampled air in the gallery or the collections room.

The proton transfer reaction mass spectrometer (PTRMS) was calibrated using a standard cylinder containing approximately 1 ppb each of methanol, acetonitrile, acetaldehyde, acetone, isoprene, 2-butanone, benzene, toluene, *o*-xylene, and 1,2,4-trimethylbenzene. Six-point calibration curves were generated by diluting the calibration gas with air that had VOCs scrubbed by a heated platinum catalyst. A generic calibration factor for other VOCs was derived by averaging the calibration factors of all calibrants besides methanol, which is excluded because its quantification at m/z 33 is impacted by the large O₂⁺ signal at m/z 32. The Thermo 43i-TLE SO₂ analyser, Thermo 42i-TL NO_x analyser, and Picarro G2401 cavity ringdown spectrometer

were calibrated by generating five-point calibration curves in the field every week. Standard cylinders of SO₂, NO, CO and CO₂ were purchased from Scott-Marrin, Inc. and had concentrations of 1.01 ppm, 5.2 ppm, 9.72 ppm, and 39,800 ppm respectively. Standard cylinders were diluted with zero air (Ultra Zero grade, Airgas). The Thermo 49i O₃ analyser was calibrated against the Thermo 42i-TL NO_x analyser in lab by reacting O₃ + NO → NO₂ in a 23 m³ Teflon environmental chamber. Photolysis rates were measured by collecting ambient light using a flat circular quartz diffuser plate (5 mm diameter), coupled to a commercial spectrometer (Ocean Optics USB 2000+) via a 10-meter UV-grade fiber. Absolute spectral actinic fluxes were calibrated using NIST-calibrated light sources. Details of the calibration setup can be found Stark et al., 2007. Photolysis rates were calculated from the spectral actinic flux using reference absorption spectra and quantum yields (Sander et al., 2003). Compounds detected by the NO₃-CIMS were quantified by assuming that analytes cluster with nitrate anions at the collisional limit (Ehn et al. 2014; Krechmer et al. 2015) and that 35% of HOMs are lost irreversibly to the walls of the inlet.

3.2.3. Art Museum Model. A simple box model was used to quantify emissions, deposition, and reaction rates of chemicals inside the museum, as depicted in Figure 3.1. In the model the museum is represented by two compartments: the gallery and the supply air + rest of the museum. For consistency with the discussion of measurements we refer to the two compartments as the gallery and the supply air, since these correspond to the two air sampling locations. The measured supply air concentration was used to represent the rest of the museum because the supply air is 74% recirculated air from the rest of the museum, 16% recirculated gallery air, and 10% outside air. Exchange between (a) the gallery and the supply air and (b) the supply air and outside air were determined from the ventilation rates given above, both

compartments assumed to be well mixed. The model was numerically integrated using the Euler method at a time step of 0.36 s. Shortening the time step did not affect the model outputs.

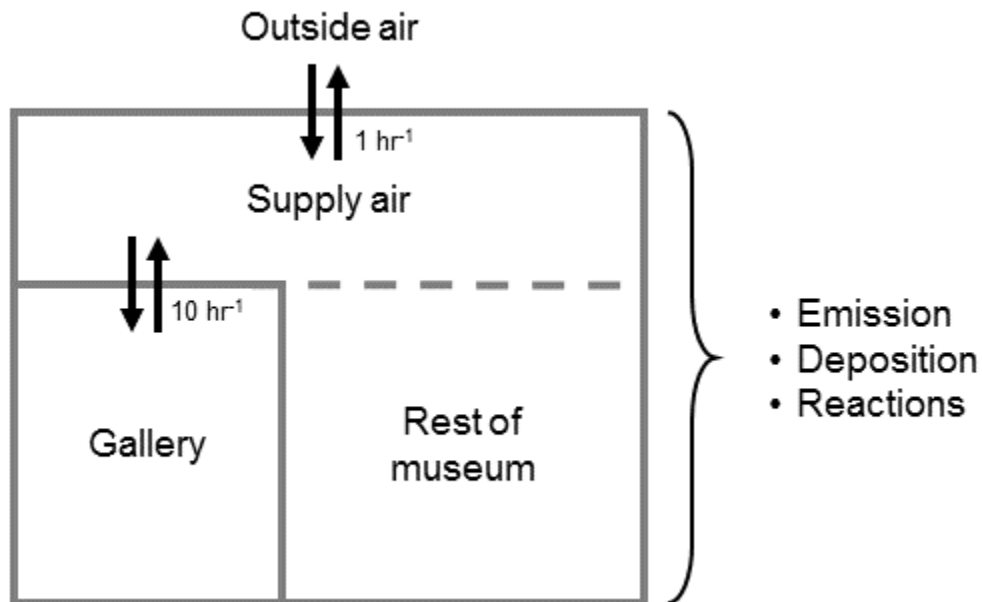


Figure 3.1. Schematic of the box model used to describe the transport, emission, deposition, and reaction of compounds in the University of Colorado Art Museum. The air exchange rate of the gallery is 10 hr^{-1} and the indoor-outdoor air exchange rate is 0.8 hr^{-1} . The museum is represented by two compartments, the gallery and the supply air + rest of the building, corresponding to the two sampling locations of this study. Air in each compartment is assumed to be perfectly mixed.

Emissions of VOCs inside the gallery were quantified using Equation 3.1 (Tang et al. 2015),

$$E(t)_g = V_g \left[AER_g ([A]_g - [A]_s) + \frac{d[A]_g}{dt} \right] \quad (3.1)$$

where $E(t)_g$ is the mass emission rate at time t , V_g is the gallery volume, AER_g is the gallery's air exchange rate, and $[A]_g$ and $[A]_s$ are the VOC concentrations in the gallery and supply air.

Emissions occurring inside the museum but outside the gallery were quantified similarly using Equation 3.2,

$$E(t)_m = V_m \left[AER_m ([A]_s - [A]_o) + \frac{d[A]_s}{dt} \right] - E(t)_g \quad (3.2)$$

where $E(t)_m$ is the mass emission rate, V_m is the volume, and AER_m is the outside air exchange rate, all for the rest of the museum, and $[A]_o$ is the VOC concentration in outdoor air. Outdoor air concentrations during the integrated period were assumed to remain constant at the levels measured in the supply air immediately before the start of an emission event (Veres et al. 2013).

Deposition rates of VOCs to museum surfaces following emission in the gallery were calculated as first-order removal rates using Equation 3.3,

$$k_{dep} = -\frac{E(t)_m}{[A]_g} \quad (3.3)$$

where k_{dep} is the first-order removal rate constant. When a VOC that is emitted inside the gallery deposits to surfaces in the museum before it recirculates through the supply air, the measured increase in the supply air concentration $d[A]_g/dt$ in Equation 3.2 is smaller than the expected increase based on the gallery emission rate $E(t)_g$ in Equation 3.2. Accordingly, VOC deposition leads to a negative value of $E(t)_m$ by Equation 3.2, and the minus sign in Equation 3.3 then gives a positive value for k_{dep} .

The model was also configured to account for reactions of O_3 , NO, NO_2 , and VOCs inside the gallery. Because of variability in outdoor chemistry, we do not assume outdoor concentrations for these species but instead constrain the model using their measured supply air concentrations. The chemical reactions that were included in the model and the accompanying rate constants are presented in Table 3.1. Rate constants for VOC reactions are those of limonene (Ziemann and Atkinson, 2012), and all other rate constants were taken from the 2015 Jet Propulsion Lab Evaluation (Burkholder et al. 2015). Reaction of O_3 with the surfaces inside the gallery was modelled using a constant deposition velocity, and reaction of O_3 with people was modeled as a constant deposition velocity that scales with the number of people inside the room, with occupancy calculated as described above. These O_3 deposition velocities were varied to find

the values that gave a minimum chi-squared error when model predictions of gallery O₃, NO, and NO₂ concentrations were evaluated against their respective measured concentrations in the gallery. Measurements of photon fluxes inside the gallery gave upper limits of photolysis rates of NO₂ and NO₃ of 4.6×10^{-7} and $1.2 \times 10^{-4} \text{ s}^{-1}$, respectively. These photolysis reactions were included in the model but were too slow to affect model outputs.

Table 3.1. Chemical reactions included in the box model of the museum. Rate constants for VOC reactions are those of limonene (Ziemann and Atkinson, 2012). All other rate constants were taken from the 2015 Jet Propulsion Lab Evaluation (Burkholder et al. 2015). Ozone deposition velocities v_d were fitted to minimize the error in model estimates of gallery ozone concentration.

Reaction	Rate constant (cm ³ molec ⁻¹ sec ⁻¹)
NO + O ₃ → NO ₃ + O ₂	2.0×10^{-14}
NO ₂ + O ₃ → NO ₃ + O ₃	3.2×10^{-17}
NO ₃ + NO → 2 NO ₂	2.6×10^{-11}
NO ₃ + NO ₂ → N ₂ O ₅	1.3×10^{-13}
N ₂ O ₅ → NO ₃ + NO ₂	$3.5 \times 10^{-3} \text{ sec}^{-1}$
OH + NO ₂ → HNO ₃	1.1×10^{-11}
Limonene + O ₃ → Products	2.0×10^{-16}
Limonene + OH → Products	1.6×10^{-10}
Limonene + NO ₃ → Products	1.2×10^{-11}
O ₃ + surfaces → Products	$v_d = 0.021 \text{ cm s}^{-1}$
O ₃ + people → Products	$v_d = 0.38 \text{ cm s}^{-1} \text{ person}^{-1}$

From the model outputs of O₃ and NO_x concentrations we also estimated the net production rate of NO₃ and OH radicals inside the gallery. We estimated NO₃ radical production from the reactions presented in Table 3.1. Since NO₃ radical photolysis is very slow inside the gallery, it is not significant and the dominant loss pathways for NO₃ radicals were reaction with NO, NO₂, and VOCs. Typical sources of indoor OH radicals are photolysis of precursors like HONO (Gligorovski, 2016) and ozonolysis of alkenes (Waring and Wells, 2015). We assumed an OH radical yield of 0.5 from alkene ozonolysis (Ziemann and Atkinson, 2012), and that the only loss processes are reactions with VOCs and NO₂. Measured photon fluxes in the gallery gave an upper limit for the HONO photolysis rate (j_{HONO}) of $6 \times 10^{-8} \text{ s}^{-1}$, and assuming conditions that would maximize OH radical production from HONO photolysis and minimize OH radical production from ozonolysis (10 ppb HONO, 1 ppb alkenes) we calculate that photochemistry accounts for <5% of the OH radical production in the museum.

3.3. Results and Discussion

3.3.1. VOC Emission Rates. VOC emission rates quantified for the gallery during different periods and activities using measurements and the model are presented in Table 3.2 and Table 3.3.

Table 3.2. Emission factors and peak concentrations for volatile chemical products emissions following application of paint to 12 m² of wall in the University of Colorado Art Museum.

Ion <i>m/z</i>	Assigned compound	Paint emission factor (mg m ⁻²)	Peak concentration (ppb)
43	Carboxylic acids	160	22
45	Ethylene glycol	480	46
47	Formic acid	33	15
57	Alkanes	>75	43
59	Acetone	150	42
61	Acetic acid	190	14
71	Methyl vinyl ketone or methacrolein	2.7	1.2
73	Acrylic acid	7.1	1.1
75	Propanoic acid	8.1	2.8
87	Methacrylic acid	3.2	0.8
91	Unknown	0.8	0.4
93	Toluene	1.9	1.5
107	C ₈ aromatics	4.3	1.8
121	C ₉ aromatics	2.7	1.0
135	C ₁₀ aromatics	0.5	0.2

Table 3.3. Mass and peak concentrations for VOCs emitted inside the University of Colorado Art Museum during the ARTISTIC campaign.

Ion <i>m/z</i>	Assigned compound	Emission date and time	Mass emitted (mg)	Peak concentration (ppb)
33	Methanol	4/20, 19:30	4,500	1,020
43	Carboxylic acids	4/20, 8:00	65	13
43	Carboxylic acids	5/19, 10:15	150	17
47	Ethanol	4/20, 19:30	1,200	270
47	Ethanol	5/19, 10:15	2,000	210
57	Alkanes	4/24, 8:45	120	25
57	Alkanes	5/22, 10:00	790	27
59	Acetone	5/6, 7:00	180	13
59	Acetone	5/22, 10:00	640	21
91	Unknown	4/26, 17:00	610	0.6
91	Unknown	5/6, 7:00	6.3	0.4
93	Toluene	4/21, 12:45	17	1.5
93	Toluene	4/27, 9:30	12	0.9
93	Toluene	4/28, 12:15	9.4	0.8
93	Toluene	5/2, 7:15	22	1.2
93	Toluene	5/6, 7:00	620	18
93	Toluene	5/15, 13:30	212	5.0
95	Phenol	4/26, 17:00	610	0.6
107	C ₈ aromatic	4/30, 13:15	26	1.1
135	C ₁₀ aromatic	4/24, 10:45	20	0.2
137	Monoterpenes	4/20, 12:30	27	0.7
137	Monoterpenes	5/3, 14:15	39	1.3

On April 21st, museum staff re-painted a wall inside the gallery to prepare for an upcoming exhibit. A single coat of primer and a single coat of white paint were applied to 12 m² of wall, directly on top of the existing paint. For compounds where unambiguous identification was not possible using the quadrupole PTRMS (e.g., distinguishing propanol from acetic acid, which are both detected at m/z 47), paint samples were collected and analysed in the laboratory using a high-resolution time-of-flight VOCUS PTR-MS (Krechmer et al. 2018) to determine which compound was emitted. The compounds emitted in the painting event are consistent with several of the major classes of VCPs described by McDonald et al. (2018), including alkanes, glycol ethers, and acetone. As is discussed below, deposition of these compounds to building surfaces prior to being ventilated to outdoor air is a significant fate for VCPs emitted indoors and is a key parameter for bridging VCP emission measurements like those presented here with outdoor measurements.

On April 28th an exhibit opening was held for the thesis exhibition of the university's Bachelor of Fine Arts (BFA) program from 5:00 to 7:00 PM local time. The CO₂ mass emission rates in the museum (gallery and the rest of the building) during the opening were calculated using Equations 3.1 and 3.2, the measured time series of CO₂ in the gallery and supply air shown in Figure 3.2a, an assumed CO₂ concentration in outdoor air of 400 ppb, and the building parameters given above. Assuming an emission rate of 21 g CO₂ person⁻¹ hr⁻¹ (Tang et al. 2016), we then estimated that the average occupancies of the gallery and the rest of the building during the opening were 108 and 68 people, respectively. Museum staff counted 300 attendees at the opening, indicating that the average attendee spent 70 min ($120 \text{ min} \times 176/300$) inside the museum.

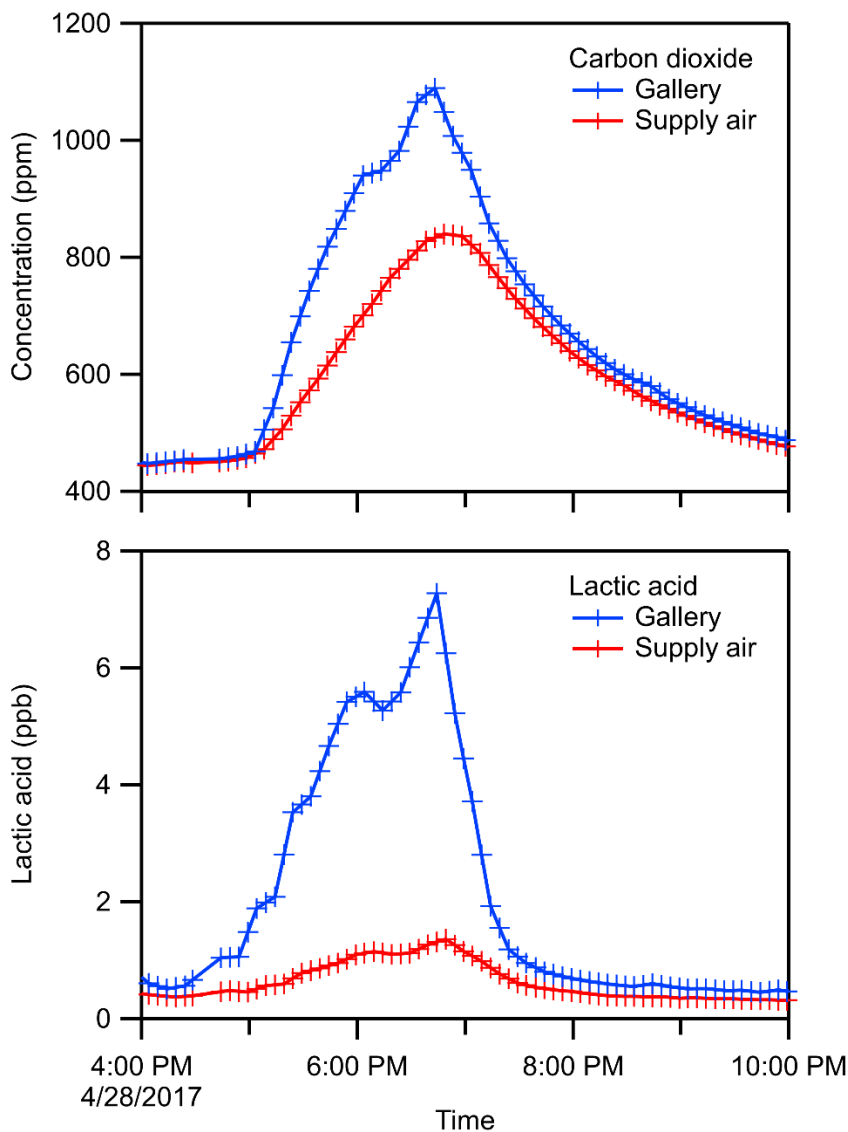


Figure 3.2. Time series of carbon dioxide (A) and lactic acid (B) concentration measured by Picarro and iodide-CIMS, respectively, during an exhibit opening at the University of Colorado Art Museum. After the conclusion of the opening at 7:00 PM carbon dioxide is removed from the museum at the rate of indoor-outdoor air exchange, while lactic acid is lost at a faster rate due to deposition to surfaces.

VOC emission rates were calculated for the gallery during the opening using Equation 3.1, the measured time series of VOCs in the gallery and supply air, and the building parameters given above. These values were more accurate than those that would be calculated for the whole

museum using Equation 3.2, because all the quantities in Equation 3.1 were known whereas the concentrations of VOCs in outdoor air that would be needed in Equation 3.2 must be assumed. Those gallery emission rates that correlated with CO₂ were then used to calculate average per-person VOC emission rates during the entire opening. The results are shown in Figure 3.3, where they are compared to human emission factors measured by Tang et al. (2016) in a classroom. Most values agree within a factor of two, except for monoterpenes (*m/z* 81 and 137), ethanol (*m/z* 47), and products of reactions of O₃ with skin oil, such as 6-methyl-5-hepten-2-one (6-MHO, *m/z* 127 and 109) and 4-oxopentanal (4-OPA, *m/z* 101). The elevated ethanol emission rate during the exhibit opening compared to the classroom is likely due to alcohol consumption by attendees prior to the opening since no alcohol was served at the opening. The ethanol emissions are consistent with 16% of gallery occupants (18 people) having a blood alcohol content of 0.03, which is roughly equivalent to having consumed one standard drink in the hour prior to the opening (Kypri et al. 2005, Wright et al. 1975). Measured emissions of acetaldehyde (*m/z* 45) were also higher than prior studies, likely because breath acetaldehyde concentrations are also elevated following alcohol consumption (Wong et al. 1992). Lower observed emission rates of monoterpenes were likely due to reduced emissions from personal care products – either because these products wore off over the course of the day (Coggon et al. 2018) or because less product was used. The lower emission rates of skin oil-O₃ reaction products measured in this study compared to Tang et al. (2016) were likely due to the lower O₃ concentrations inside the museum. The average O₃ concentration in the gallery during the opening was 4.5 ppb, while the O₃ concentration in the Tang et al. study ranged from 10-25 ppb (personal communication). Additional emission events monitored in the museum are presented in Table 3.3.

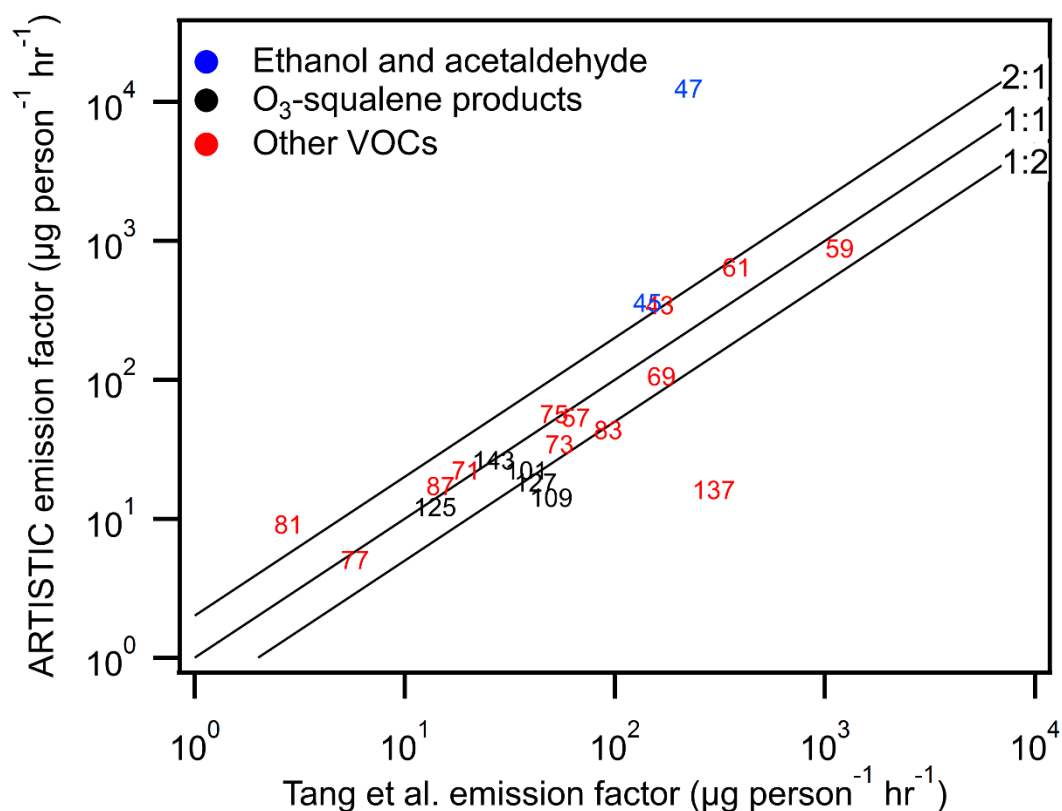


Figure 3.3. Correlation of human emission factors for this study and Tang et al. 2016. Data points are plotted as the mass-to-charge ratio measured by the quadrupole PTR-MS. Emission factors between the two studies generally agree within a factor of two. Elevated ethanol emissions (m/z 47) observed in this study are likely due to alcohol consumption and decreased monoterpene emissions (m/z 137) are likely due to lower emissions from personal care products. Additionally, lower O_3 concentrations during this study led to lower secondary emissions of O_3 with squalene on occupants' skin.

3.3.2. VOC Deposition Rates. Following emission of a compound at some point inside the museum, the compound is distributed throughout the museum via the building's HVAC system. As this happens one expects the concentration of the compound to rise in the supply air. For many of the emissions measured, however, the increase in supply air concentration was significantly lower than that predicted by the model and the measured gallery emission rate, museum volume, and air exchange rates. For example, the difference in recirculation behaviour of CO_2 and lactic acid can clearly be seen in Figure 3.2. Although lactic acid and CO_2 were co-

emitted by museum occupants during the opening, the relative increase in lactic acid concentration in the supply air was significantly less than that of CO₂. This result suggests a loss process for lactic acid that occurs between when it is emitted in the gallery and when it re-enters the gallery via the supply air. The first-order removal rates of VOCs in the gallery were calculated using Equation 3.3, the calculated VOC emission rates in the museum, and the concentrations of VOCs in the gallery. The results are shown in Figure 3.4. The values correlate inversely with the saturation vapor concentration (C^*) estimated using SIMPOL.1 (Pankow and Asher, 2008) and proportionally with Henry's law coefficients (H) estimated using GROMHE (Raventos-Duran et al. 2010), suggesting that removal occurs by deposition to surfaces in the museum and the HVAC system. For compounds with C^* below $10^8 \mu\text{g m}^{-3}$ deposition to surfaces should be a significant sink. As is discussed below, the rates of gas-phase reactions of VOCs in the museum are too slow to account for the loss rates observed here.

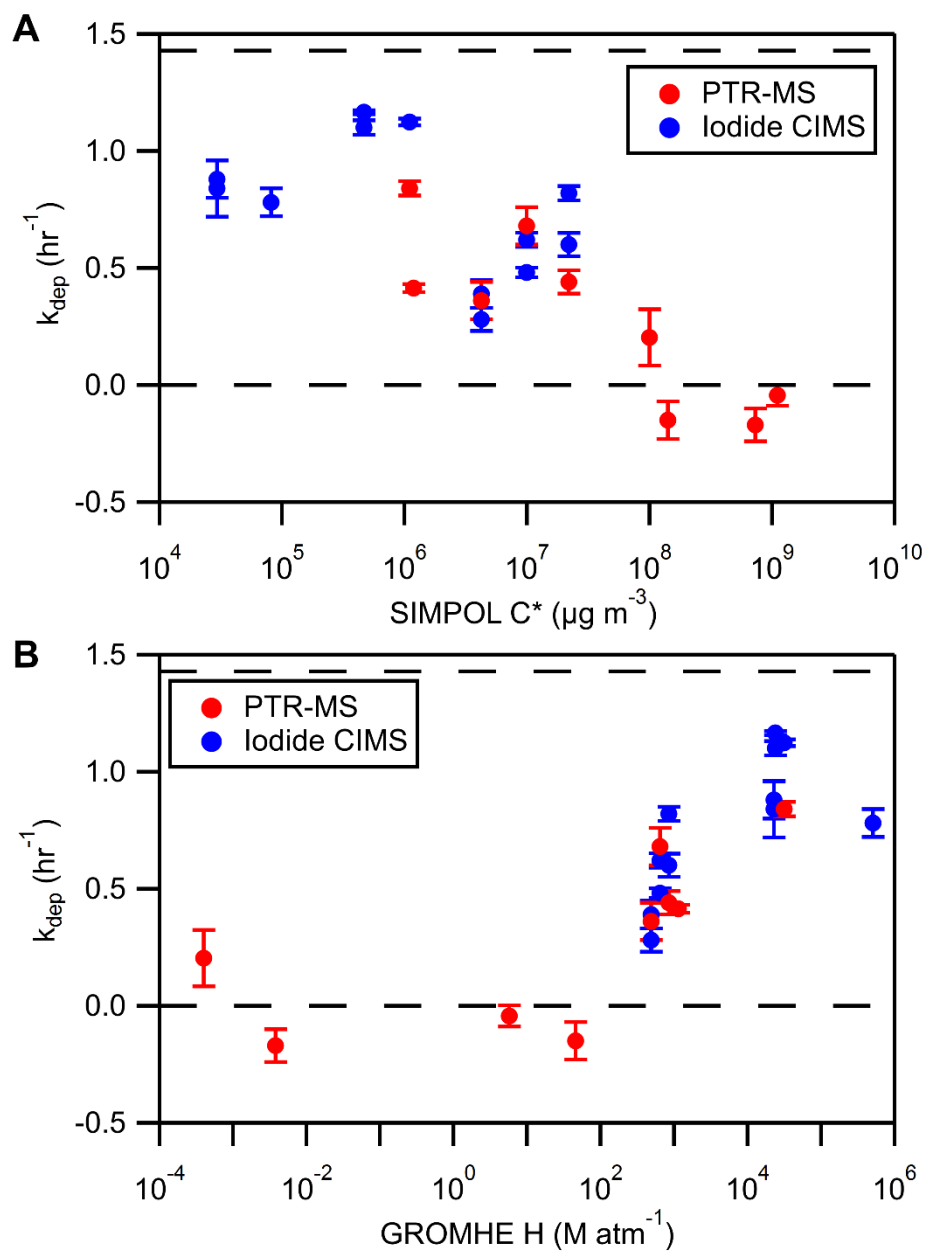


Figure 3.4. Deposition rates of organic compounds measured in the University of Colorado Art Museum as a function of volatility (C^*) and Henry's law coefficient (H) calculated using SIMPOL (Pankow and Asher, 2008) and GROMHE (Raventos-Duran et al. 2010), respectively. Deposition rate increases with decreasing volatility and with increasing Henry's law coefficient. The dashed lines represent the bounds of measurable removal rates from the museum supply air given the sampling configuration used.

Models have been developed previously that relate gas-surface partitioning indoors to compound volatility and Henry's Law coefficient (Bennett and Furtaw Jr., 2004), and key parameters that must typically be assumed are the amount of organic material and water sorbed to surfaces, which determines the volatility and Henry's Law coefficient at which a gas-phase compound will sorb to a surface. In Figure 3.4 we have plotted the deposition rate of VOCs in the museum as a function of both volatility (C^*) and Henry's law coefficient (H), but are unable to determine the relative contributions of sorption to surface water and to organic films. This is because compound saturation vapor concentrations and Henry's Law coefficients tend to show an inverse relationship (i.e., low-volatility compounds have high Henry's Law coefficients), and since the museum relative humidity is held constant we could not systematically explore the role of surface water in gas-surface partitioning. Replicating this analysis in an environment where relative humidity can vary would allow one to uncouple the two effects and determine if indoor VOC-surface partitioning is better modeled as partitioning to aqueous or organic surface films.

3.3.3. Ozone Loss Rates. We used measurements of O_3 , NO_x , and CO_2 in the gallery and the supply air to quantify the total loss rate of O_3 in the gallery and the relative loss rates to gallery surfaces, people, and reactions with NO and NO_2 . Typical depletion of O_3 observed in the gallery relative to the supply air was 1 ppb. To simulate this, the model depicted in Figure 3.1 was run with the reactions given in Table 3.1 included and with the supply air concentration of O_3 , NO , and NO_2 constrained to the measured concentration for each compound. Ozone deposition velocities were then fitted to give the best agreement between the measured and modeled gallery concentrations of O_3 , NO , and NO_2 . The estimated per-person deposition velocity calculated for the gallery of $0.38 \text{ cm s}^{-1} \text{ person}^{-1}$ is consistent with the range of $0.40\text{-}0.62 \text{ cm s}^{-1}$ reported in past studies carried out in well-controlled test rooms (Fadeyi et al. 2013;

Wisthaler and Weschler 2010) and in classrooms (Fischer et al. 2013). The O₃ deposition velocity to surfaces of 0.021 cm s⁻¹ is also consistent with prior measurements of indoor environments (Reiss et al. 2004). The agreement of these results gives us confidence both in our model and in the generalizability of the test room results.

The modeled loss rates of O₃ to reaction with surfaces, occupants, and NO_x during two days of the ARTISTIC campaign are presented in Figure 3.5. Averaged over the three weeks of gallery measurements surfaces accounted for 62% of the O₃ loss, NO for 31%, occupants for 5%, and NO₂ for 2%. Especially notable in Figure 3.5 is the temporal variability of the contributions of NO to O₃ loss. Depending on the NO concentration and gallery occupancy the O₃ removal rate inside the gallery varied by a factor of four. The NO concentrations in the museum supply air for the period presented in Figure 3.5 varied between 0 to 4 ppb, with the rapid variations in concentration indicating a nearby source that was likely traffic emissions from surrounding streets or possibly emissions from pottery kilns located in an adjacent building. These rapid variations in NO concentration drastically affected the O₃ loss rate, reducing the amount of O₃ reacting with other sinks when NO concentrations were high. The opening for the BFA exhibit took place on April 28th, and the high occupancy inside the gallery led to people being the dominant sink for O₃ in the gallery. Conversely, on Saturday April 29th museum occupancy and NO concentrations were both low (Figure 3.5), which was typical of weekend days in our study, and under those conditions surfaces were the dominant O₃ sink. These results show that the reactive loss of O₃ indoors is highly variable in time, and an accurate accounting of the fate of O₃ in a particular indoor environment must account for the variability in occupancy and NO_x in the space being studied. This behaviour also has significant implications for production of indoor NO₃ and OH radicals, as discussed below.

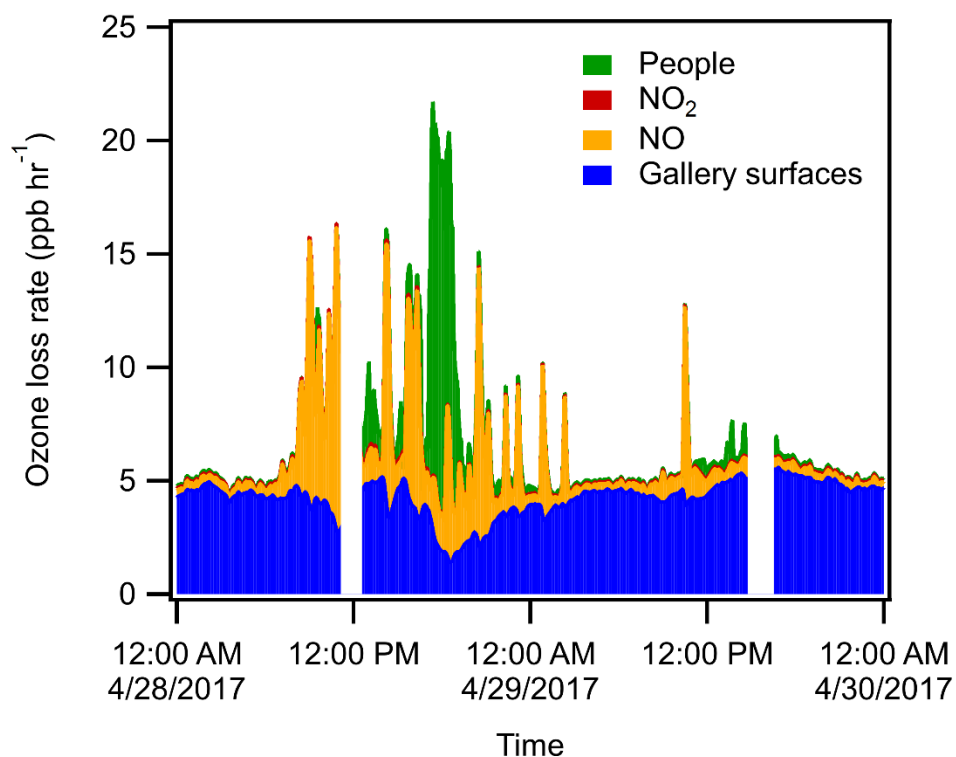


Figure 3.5. O₃ loss rate in the University of Colorado Art Museum gallery apportioned between reactions with gallery surfaces, occupants, NO, and NO₂. The art exhibit opening can be clearly seen as the dramatic increase in the loss rate to occupants at 5:00 PM on April 28th.

3.3.4. VOC Oxidation and Autoxidation. To evaluate the relative contributions of reactions with O₃, OH radicals, and NO₃ radicals to VOC chemistry inside the gallery we used our O₃ concentration measurements along with model estimates of OH and NO₃ radical concentrations. Because the primary source of OH radicals inside the museum is alkene ozonolysis (due to low photolysis rates), a surrogate alkene was incorporated into the model to react with O₃ and generate OH radicals. The surrogate alkene has a concentration of 5 ppb (twice the average measured alkene concentration in the museum) and reacts with ozone at the rate constant of limonene ($2.1 \times 10^{-16} \text{ cm}^3 \text{ molec}^{-1} \text{ s}^{-1}$) (Atkinson and Arey, 2003). These conditions were chosen to maximize estimates of OH radical production, giving upper limits for the OH radical concentration and oxidation rates presented below. The maximum concentrations of O₃,

OH radicals and NO₃ radicals in the museum were 2.4×10^{11} molecules cm⁻³ (12 ppb), 1.2×10^5 molecules cm⁻³ (0.0059 ppt) and 2.0×10^6 molecules cm⁻³ (0.098 ppt). From these concentrations and the known rate constants for reactions of limonene with each oxidant (Table 3.1), we estimated the lifetime of the surrogate alkene with respect to reaction with O₃, OH radicals and NO₃ radicals in the museum to be 5.5 h, 15 h, and 12 h. Since saturated compounds react almost exclusively with OH radicals and the rate constant for reaction of OH radicals with most of these compounds is smaller than that for limonene (Atkinson and Arey, 2003), the lifetimes for most saturated VOCs with respect to oxidation will be greater than 15 hr. These upper-limit values indicate that VOC removal by ventilation (1.25 h timescale) and deposition (>1 h timescale for compounds with C^* below 10^8 μg m⁻³) dominates over oxidation, especially for saturated VOCs because of their slow reactions with O₃ and NO₃.

We evaluated the model predictions regarding the chemistry of the surrogate alkene using an experiment in which a navel orange was peeled and eaten inside the museum in order to release monoterpenes, all of which were detected by the PTR-MS at m/z 81 and 137. Since measurements by Arey et al. (1991) indicated that >90% of the monoterpene emissions from a navel orange were limonene, for this discussion we assumed that those emitted in the museum consisted entirely of this compound. The increase in concentration of limonene above the background due to the orange emissions was ~1 ppb, corresponding to a total mass of emitted limonene of 77 mg. As can be seen in Figure 3.6A, the timescale for limonene removal following emission was 0.87 h, which is faster than the expected loss rate due to the exchange of indoor and outdoor air by the museum's HVAC system (1.25 h). The model prediction for the timescales for limonene removal by reactions with O₃, OH radicals and NO₃ radicals are 8.3 h, 17 h, and 7.7 h, giving a combined removal timescale of 3.25 h. The saturation vapor

concentration of limonene is $2 \times 10^7 \mu\text{g m}^{-3}$, and using Figure 3.4 we estimate that the deposition timescale of limonene is between 1.1 h and 6.6 h, and for the following calculations we use 2 h, the timescale calculated from the average of the two rate constants. When oxidation happens in parallel with removal by ventilation and deposition to indoor surfaces, the predicted timescale for removal of limonene from the museum is 0.62 h. As shown in Figure 3.6A, this value is in reasonable agreement with the measured timescale of 0.87 h. Under these conditions, 19% of the limonene reacts, 31% deposits to indoor surfaces and the remainder is ventilated to outdoor air.

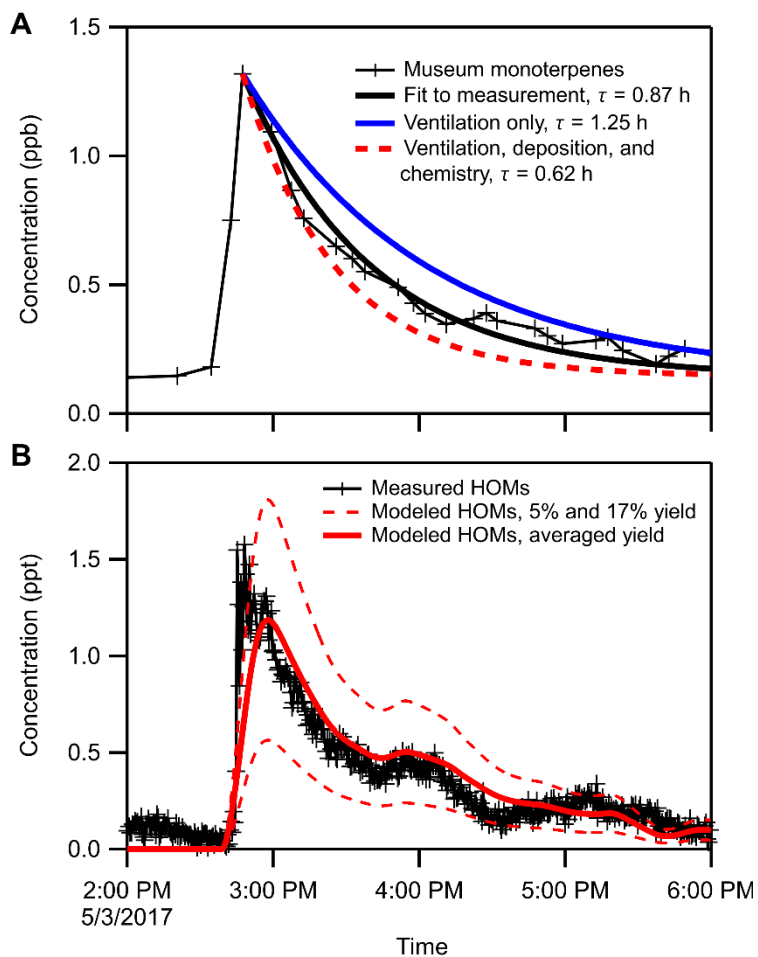


Figure 3.6. Measured and modeled time series of limonene concentrations in the University of Colorado Art museum following the consumption of an orange showing removal by ventilation and chemistry (A). Measured and modeled concentrations of highly oxidized multifunctional

compounds (HOMs) produced from limonene ozonolysis (B). The model outputs using the two published yields for limonene HOMs bracket the measured HOM concentrations.

We also used the limonene emission event to evaluate model predictions of product formation by comparing NO₃-CIMS measurements of HOMs formed from limonene ozonolysis to model predictions. The two published HOM yields for limonene ozonolysis are 5.3% (Jokinen et al. 2015) and 17% (Ehn et al. 2014), and the model predictions using each of these yields and their average are shown alongside our measurements of indoor HOMs in Figure 3.6B. The mass spectrum and assigned molecular formulas of the highly oxygenated multifunctional compounds (HOMs) measured with NO₃-CIMS following the emission of limonene in the museum are presented in Figure 3.7 and Table 3.4. The observed mass spectrum is similar to that observed by Jokinen et al. (2014) in a laboratory study of limonene ozonolysis, providing additional support for our assignments. To our knowledge this is the first measurement of HOMs in the indoor environment. The average HOM yield of 11% is in excellent agreement with our measurements. Since HOMs are low-volatility species and are expected to condense to the aerosol phase we included a term in the model to account for the condensational sink as measured by the SMPS of $\tau_{CS} = 13$ min. We also assumed that the HOMs were sufficiently low-volatility that they were quantitatively removed from the museum supply air so that the concentration being brought into the gallery was zero.

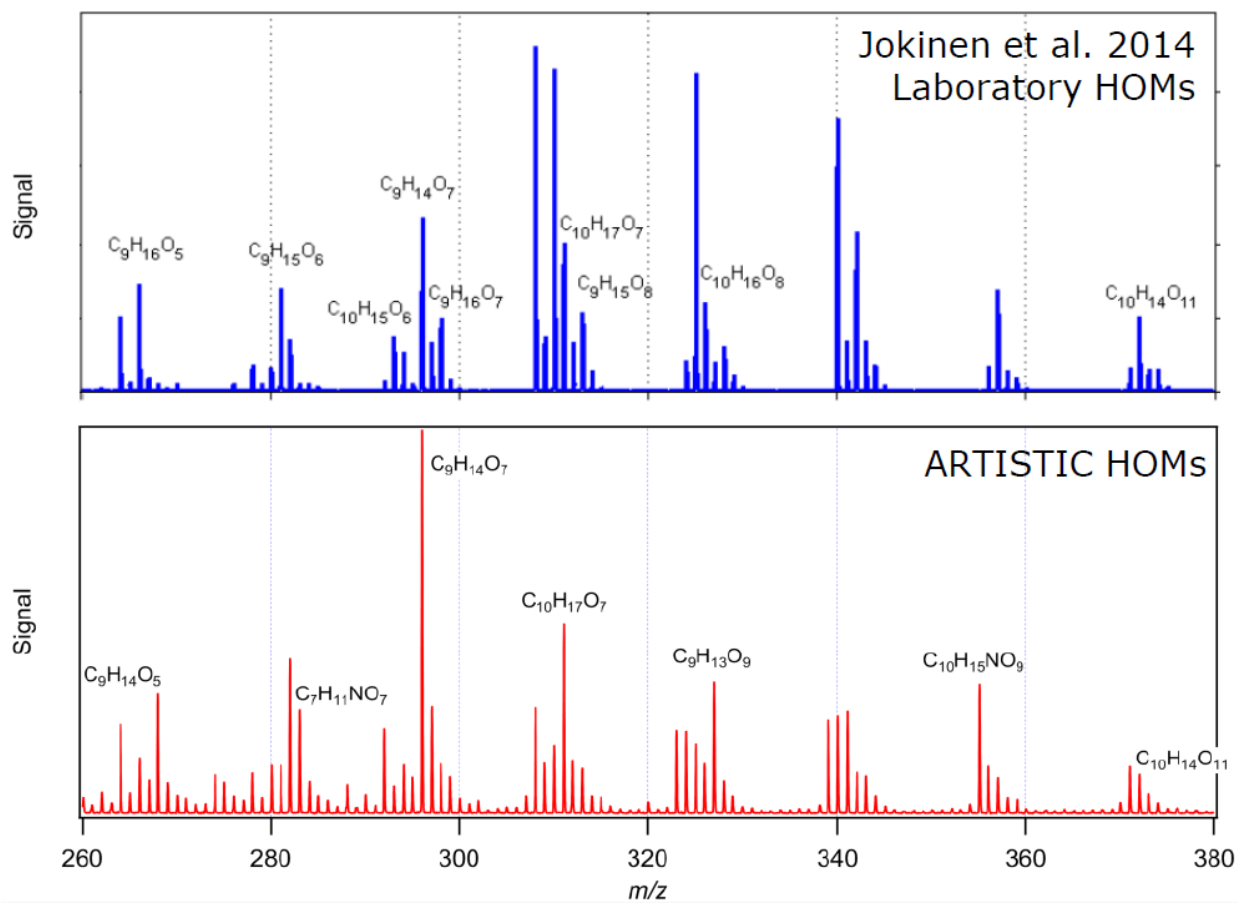


Figure 3.7. Comparison of nitrate-CIMS mass spectra of HOMs formed from limonene ozonolysis in a laboratory (Jokinen et al. 2014) and in the University of Colorado Art Museum.

Table 3.4. Assigned molecular formulas and detected m/z 's for HOMs formed from limonene ozonolysis in the University of Colorado Art Museum.

Assigned formula	m/z	Assigned formula	m/z
$C_9H_{14}O_5 \cdot NO_3^-$	264.07249	$C_{10}H_{15}O_8 \cdot NO_3^-$	325.065059
$C_9H_{16}O_5 \cdot NO_3^-$	266.08814	$C_{10}H_{16}O_8 \cdot NO_3^-$	326.072884
Unassigned	268.039813	$C_9H_{13}O_9 \cdot NO_3^-$	327.044323
$C_9H_{16}O_6 \cdot NO_3^-$	281.07523	$C_9H_{16}NO_8 \cdot NO_3^-$	328.075958
Unassigned	282.061145	$C_{10}H_{15}NO_8 \cdot NO_3^-$	339.068133
$C_7H_{11}NO_7 \cdot NO_3^-$	283.041918	$C_{10}H_{14}O_9 \cdot NO_3^-$	340.052148
$C_{10}H_{15}O_6 \cdot NO_3^-$	293.07523	Unassigned	341.069504
$C_9H_{14}O_7 \cdot NO_3^-$	296.062319	$C_9H_{14}NO_9 \cdot NO_3^-$	342.055222
$C_9H_{15}O_7 \cdot NO_3^-$	297.070144	$C_9H_{15}NO_9 \cdot NO_3^-$	343.063047
$C_9H_{16}O_7 \cdot NO_3^-$	298.077969	$C_{10}H_{15}NO_9 \cdot NO_3^-$	355.063047
$C_{10}H_{14}O_7 \cdot NO_3^-$	308.062319	$C_9H_{12}NO_{10} \cdot NO_3^-$	356.034487
$C_{10}H_{15}O_7 \cdot NO_3^-$	309.070144	$C_{10}H_{15}O_{10} \cdot NO_3^-$	357.054888
$C_9H_{14}NO_7 \cdot NO_3^-$	310.065393	Unassigned	371.048385
$C_{10}H_{17}O_7 \cdot NO_3^-$	311.085794	$C_{10}H_{14}O_{11} \cdot NO_3^-$	372.041978
$C_9H_{14}O_8 \cdot NO_3^-$	312.057234	$C_{19}H_{32}O_7 \cdot NO_3^-$	434.20317
$C_9H_{15}O_8 \cdot NO_3^-$	313.065059	$C_{19}H_{30}O_{12} \cdot NO_3^-$	512.162093
$C_7H_{17}O_{10} \cdot NO_3^-$	323.070538	$C_{20}H_{30}O_{14} \cdot NO_3^-$	556.151922
$C_{10}H_{14}O_8 \cdot NO_3^-$	324.057234	$C_{20}H_{30}O_{16} \cdot NO_3^-$	588.141751
		$C_{20}H_{30}O_{18} \cdot NO_3^-$	620.131581

Because HOMs are known to contribute significantly to total particulate matter in pristine outdoor environments (Ehn et al. 2014), we evaluated the impact of HOM formation in this experiment on the total mass of submicron particulate matter (PM_{10}) inside the museum. Using

the reaction and ventilation timescales described above and assuming a 25% SOA yield (Waring 2016), we predicted an increase in aerosol mass concentration inside the museum of $0.19 \mu\text{g m}^{-3}$, consistent with the increase in PM_{10} concentration measured by our SMPS of $0.22 \mu\text{g m}^{-3}$.

The observed HOM production in the gallery shows that autoxidation is a significant fate for organic peroxy radicals indoors. Using the method outlined in Praske et al. (2018) and our measurements of NO in the museum, we estimated that the bimolecular reaction lifetime of organic peroxy radicals in the museum was over 10 s 85% of the time, indicating that bimolecular organic peroxy radical reactions inside the museum were sufficiently slow to allow indoor autoxidation to proceed. It is important to note that low NO conditions inside the museum sometimes occurred even when significant NO was entering the museum from outdoors, but that indoor conversion of NO to NO_2 by reaction with O_3 maintained NO at sufficiently low concentrations for autoxidation to proceed. As the atmospheric chemistry community continues to conduct research on VOC autoxidation and subsequent SOA formation the results will also be broadly applicable to indoor air chemistry.

3.4. Conclusions

The results of this study show that when real-time measurements of VOCs and other trace gases are combined with relatively simple box modeling that it is possible to extract a wealth of qualitative and quantitative information about the transport, emission, deposition, and transformation of chemicals in the indoor environment. In our case, the box modeling was greatly simplified by the museum's constant volume flow ventilation system. Many indoor environments do not have such consistent air exchange rates, and accurately modeling transport within those environments requires significant effort to determine the variability in air exchange rates over time. Emissions of volatile chemical products were identified as the dominant source

of VOCs inside the museum, and often occurred in discrete events. The variability in the compounds emitted in each event demonstrates a continued need for real-time characterization of the composition and concentrations of chemical products used indoors.

The observed effect of a VOC's vapor pressure and Henry's law coefficient on deposition indicates that VOC sorption to indoor surfaces is analogous to gas-particle partitioning in the atmosphere, with the high indoor surface area concentrations extending the upper limit of volatility for compounds that will partition to the condensed phase by several orders of magnitude. The volatility range of compounds that deposit to indoor surfaces in the museum extends to higher volatility than is expected for partitioning to impermeable surfaces, indicating that absorption of VOCs by permeable surfaces, including paints and plastics, may play a significant role in VOC deposition indoors.

Deposition and ventilation to outside air are the dominant removal processes of VOCs indoors, with some removal of alkenes by O_3 and NO_3 oxidation. Simple reaction lifetime calculations using our estimates of indoor oxidant concentrations show that indoor VOC oxidation is generally slower than indoor-outdoor air exchange rates and deposition, and in environments without a photolytic OH source saturated VOCs have lifetimes of tens of hours, rendering them essentially inert indoors. Our measurements of rapid changes of the indoor O_3 reaction rate caused by variations in NO concentration demonstrate the importance of O_3 - NO_x reactions in determining the oxidation regime of indoor air for the small fraction of VOCs that react before being ventilated or depositing to a surface. In this study rapid titration of NO by excess O_3 and low rates of photolysis created an environment that favored low- NO_x chemistry initiated by O_3 , where RO_2^* radical intermediates reacted with HO_2^* radicals, other RO_2^* radicals, and by autoxidation to form peroxide-containing products. However, in environments where O_3

is instead titrated by excess NO_x , such as buildings with indoor combustion, high- NO_x chemistry is likely dominant. Oxidation is then initiated primarily by reaction with OH radicals, and RO_2^{\bullet} radical intermediates react with NO to form organic nitrates along with other products. As in outdoor air, defining the oxidation regime of an indoor environment allows for placement of better constraints when modeling oxidation rates, reaction products, and SOA yields.

Chapter 4

Effects of Gas-Wall Partitioning in Teflon Tubing and Instrumentation on Time-Resolved Measurements of Gas-Phase Organic Compounds

Reprinted with permission from Pagonis, D., Krechmer, J. E., de Gouw, J., Jimenez, J. L., and Ziemann, P. J.: Effects of gas-wall partitioning in Teflon tubing and instrumentation on time-resolved measurements of gas-phase organic compounds, *Atmospheric Measurement Techniques* 10, 4687-4696, doi: 10.5194/amt-10-4687-2017, 2017.

4.1. Introduction

Teflon tubing is widely used for sampling organic gases in field and laboratory studies, primarily because it is chemically inert and flexible. These properties also make Teflon the material of choice for environmental “smog” chambers, most of which are constructed using fluorinated ethylene-propylene (FEP) or perfluoroalkoxy (PFA) Teflon film (Hallquist et al. 2009). Although it has been known for decades that Teflon is permeable to small organic compounds (Yi-Yan et al., 1980; Chemours, 2016), only recently have environmental chamber studies shown that it can also absorb large gaseous organic compounds in an equilibrium partitioning process that is rapid (time scale ~10–60 min), reversible, and independent of the age of the chamber (Matsunaga and Ziemann, 2010; Yeh and Ziemann, 2015; Zhang et al., 2015; Krechmer et al., 2016; Ye et al., 2016). The equilibrium reached in this process can be conveniently described using a model that is analogous to gas-particle partitioning theory (Matsunaga and Ziemann, 2010), in which the chamber walls are treated as an equivalent mass

concentration of liquid organic aerosol, C_w . Values of C_w reported by Matsunaga and Ziemann (2010), Yeh and Ziemann (2015), and Krechmer et al. (2016) range from 0.3-30 mg m⁻³ for an 8 m³ chamber, a range indicating that a significant fraction of organic products formed from oxidation reactions regularly studied in environmental chambers (and even some less-volatile precursors) will be absorbed into the walls at equilibrium. Using typical values for C_w and the time scale for reaching gas-wall partitioning equilibrium, one can incorporate the effect into box models to estimate the effect of partitioning on chamber measurements, as has been done in several studies of secondary organic aerosol (SOA) yields (Matsunaga and Ziemann, 2010; Shiraiwa et al., 2013; McVay et al., 2014; Bian et al., 2015; Krechmer et al., 2015; La et al., 2016).

Although gas-wall partitioning of organic compounds in Teflon environmental chambers has now been systematically investigated in a number of studies, this is not the case for Teflon tubing used for sampling lines. Delays in instrument response have been observed and documented repeatedly, with many references to “sticky” compounds and “memory effects” inside tubing and instrumentation. For example: Teflon O-rings are used inside the proton transfer reaction-mass spectrometer (PTR-MS) because other materials caused significant delays (Warneke et al., 2003); measured eddy covariance frequencies are dampened by sticky compounds (Park et al., 2013); heated instruments have been developed specifically to reduce delays for semivolatile compounds (Mikoviny et al., 2010); and instrument surfaces are often heated when measuring aerosol components through thermal desorption (Holzinger et al., 2010). Memory effects in the inlet of the PTR-MS have been modeled previously, but the concept was not extended to tubing (Schuhfried et al., 2012).

In the study presented here, we quantified delays observed when a set of organic compounds with a range of volatilities were sampled through Teflon tubing for analysis in a PTR-MS, and then developed a model that applies the principles of gas chromatography and gas-wall partitioning in Teflon environmental chambers to predict the delays measured for different tubing lengths and diameters, flow rates, and organic functional groups. The results quantify the potential effects of tubing on measurements of organic gases and enable better design of sampling systems, in particular when fast instrument response is needed.

4.2. Materials and Methods

4.2.1. Measurements of Tubing Delay. Experiments were conducted by sampling homologous series of either C₁₁, C₁₂, C₁₄–C₁₆ 1-alkenes (1-undecene, 1-dodecene, 1-tetradecene, 1-pentadecene, 1-hexadecene) or C₈, C₁₀, C₁₂–C₁₄ 2-ketones (2-octanone, 2-decanone, 2-dodecanone, 2-tridecanone, 2-tetradecanone) from an 8 m³ FEP Teflon environmental chamber into a quadrupole PTR-MS using Teflon tubing. The PTR-MS has been described previously (de Gouw and Warneke, 2007). For each experiment approximately 20 ppb of each of the compounds in a homologous series were added to the chamber by evaporating a known amount from a glass bulb (with heating as necessary) into a 5 L min⁻¹ stream of ultra high purity (UHP) N₂. The chamber was then mixed with a Teflon-coated fan for 1 min and allowed to sit for 30 min to ensure that gas-wall partitioning equilibrium had been achieved inside the chamber (Matsunaga and Ziemann, 2010). The combined passivation time of the tubing + PTR-MS for compounds in the chamber was determined by moving the tubing from sampling room air (a clean air source for the conditions of these experiments) to sampling chamber air containing the compounds. This procedure produces a step function in the concentration of compounds sampled, and is identical to frontal analysis, a long-standing technique for characterizing

chromatography columns (James and Phillips, 1954; Schay and Szekely, 1954). After the instrument response reached steady state (meaning that the PTR-MS and tubing were fully equilibrated with the incoming air), either the tubing was moved back to sampling room air, allowing the PTR-MS and tubing to approach a new equilibrium state, or the PTR-MS was investigated separately by detaching the inlet tubing so that it sampled room air directly. The effect of the tubing on the equilibration time was isolated by comparing the response times when the PTR-MS was sampling room air with and without the tubing.

The base case measurements of delays were conducted with 2-ketones sampled through 1.0 m of PFA Teflon tubing (1/4 in. OD, 3/16 in. ID) at a flow rate of 0.36 L min^{-1} , with the 1-alkenes evaluated under the same conditions. The effect of tubing length on the delay was evaluated by also using 3.0 m of PFA Teflon tubing with the same OD and ID at a flow rate of 0.36 L min^{-1} . The effect of flow rate on the delay was evaluated by increasing the flow rate from 0.36 to 2.7 L min^{-1} by adding a line sampling an additional 2.3 L min^{-1} flow (controlled by a critical orifice) in parallel with the PTR-MS. In this experiment a 3.0 m length of PFA Teflon tubing was used to achieve a sufficiently large delay. The effect of tubing diameter on the delay was investigated using a 3.0 m length of 1/8 in. OD, 1/16 in. ID PFA Teflon tubing at a flow rate of 0.36 L min^{-1} . Flow was laminar in the tubing during all experiments, with calculated Reynolds numbers of 90 and 650 for the low and high flow experiments in the 3/16 in. ID tubing and 260 in the experiment using 1/16 in. ID tubing. The tests were conducted at ambient laboratory temperature ($23 \text{ }^{\circ}\text{C}$) and when the instruments had been pumped down and operated for several weeks, thus representing typical operating conditions.

4.2.2. Chemicals The following chemicals, purities, and suppliers were used in this study: 1-undecene (97%), 1-dodecene (95%), 1-tetradecene (92%), 1-pentadecene (98%), 2-

octanone (98%), 2-decanone (98%), and 2-tridecanone (99%) from Aldrich; 2-dodecanone (98%) and 2-tetradecanone (98%) from ChemSampCo; and 1-hexadecene (99.8%) from Fluka.

4.2.3. Model for Transport of an Organic Compound Through Teflon Tubing

The model used to describe the effect of tubing on the delay is a linear kinetic chromatography model, where the affinity of a compound for the walls of the Teflon tubing (the stationary phase) is determined by its saturation concentration (c^*). This approach seems reasonable, considering the nature of the processes involved, the dependence of gas-wall partitioning on c^* (Matsunaga and Ziemann 2010; Krechmer et al., 2016), and the observation that the extent of partitioning of an organic compound in a Teflon chamber correlates well with its retention time measured by gas chromatography (Yeh and Ziemann, 2015). Based on the chamber results, we assume that the rate of absorption of a compound into the walls is controlled by gas-phase diffusion to the walls (and thus does not depend on mass accommodation), and treat absorption and desorption as first-order processes. For a numerical solution the tubing is divided into a series of perfectly mixed bins, with compound flowing into and out of each bin and also undergoing gas-wall partitioning, as shown in Figure 4.1.

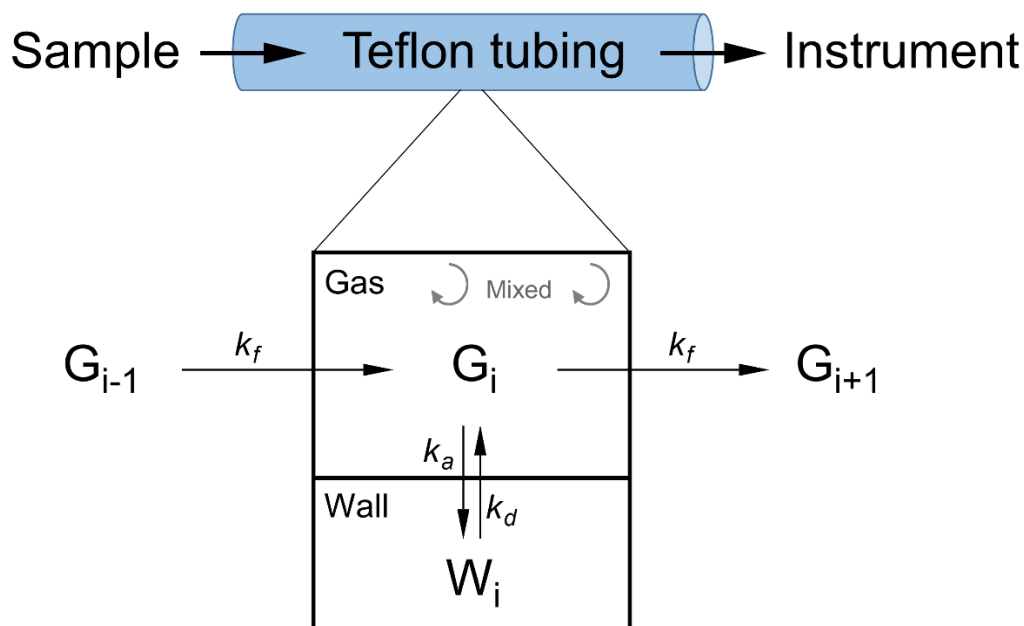


Figure 4.1. Schematic of the chromatography model used to describe delays caused by gas-wall partitioning of organic compounds in Teflon tubing. Compounds flow through a series of perfectly mixed bins, undergoing gas-wall partitioning within each bin. The rates of flow between bins (k_f), absorption (k_a) and desorption (k_d) are dependent on tubing diameter, flow rate, and the saturation vapor concentration c^* of the compound being measured.

Our assumption of diffusion-limited absorption is consistent with the criteria developed by McMurry and Stolzenburg (1987), who compared time scales for diffusion and uptake at the walls to determine whether mass accommodation affects the uptake kinetics of sticky compounds passing through tubing. They estimate the time scale for diffusion (τ_{diff}) as in Equation 4.1:

$$\tau_{diff} = \frac{d_t^2}{8 D_g} \quad (4.1)$$

and the time scale for accommodation into the wall (τ_{ac}) as in Equation 4.2:

$$\tau_{ac} = \frac{d_t}{2 \alpha \bar{c}} \quad (4.2)$$

where D_g is the compound's diffusion coefficient in air, α is its mass accommodation coefficient on the tubing wall, \bar{c} is its mean thermal speed, and d_t is the ID of the tubing. The mass accommodation coefficient has an impact on the rate of uptake at the walls when the time scale

for accommodation is comparable to or larger than the time scale for diffusion, as in Equation 4.3:

$$\frac{\tau_{ac}}{\tau_{diff}} = \frac{4 D_g}{\alpha \bar{c} d_t} \gtrsim 1 \quad (4.3)$$

Using a diffusion coefficient of $0.067 \text{ cm}^2 \text{ s}^{-1}$, the average of values calculated for the compounds studied here (range = $0.055 - 0.088 \text{ cm}^2 \text{ s}^{-1}$) using three methods (Tucker and Nelken, 1986), and a tubing ID of 0.47 cm, Equation 4.3 indicates that mass accommodation does not affect the rate of uptake to the walls for values of $\alpha > 3 \times 10^{-5}$. Since this threshold is similar to that determined in studies of gas-wall partitioning in Teflon environmental chambers, where it has been shown that the rate of turbulent mixing within the chamber is the rate-limiting process in establishing partitioning equilibrium for compounds with mass accommodation coefficients greater than $\sim 10^{-5}$ (Matsunaga and Ziemann, 2010; Krechmer et al., 2016), our assumption that absorption of compounds into the walls is limited by gas-phase diffusion seems justified.

The first-order rate constant for absorption of compounds into the tubing walls (k_a) was calculated using Equation 4.4:

$$k_a = \frac{8 D_g}{d_t^2} \quad (4.4)$$

which is the inverse of the time scale for diffusion-limited transport to the walls given by Equation 4.1. For the 0.47 cm ID tubing used in our experiments, $\tau_a = 0.4 \text{ s}$. Rate constants for desorption of compounds out of the walls (k_d) were calculated using Equation 4.5:

$$k_d = \frac{k_a}{K_{gw}} \quad (4.5)$$

where K_{gw} is the equilibrium constant for gas-wall partitioning inside the tubing. The most and least volatile compounds measured here had desorption time scales of 0.2 s and 50 s, respectively, in 0.47 cm ID tubing. Values of K_{gw} were calculated using Equation 4.6:

$$K_{gw} = \frac{C_w}{c^*} \quad (4.6)$$

which was employed by Matsunaga and Ziemann (2010) in their model for gas-wall partitioning in Teflon environmental chambers. Values of c^* were estimated using the SIMPOL.1 group contribution method (Pankow and Asher, 2007), and the effective wall mass C_w for PFA Teflon tubing was determined by fitting the model output for our base experimental case (0.47 cm ID tubing sampling at 0.36 L min⁻¹) to the experimentally determined tubing delays under those conditions. We varied C_w in the model to generate tubing delays as a function of c^* , and we then used an orthogonal-distance regression to minimize a sum-of-squares residual. These residuals were calculated in log-log space (log(delay) vs log(c^*), as the data is shown in Figure 4.5) because both compound c^* and tubing delays vary across several orders of magnitude and we wished to avoid biasing the fitting towards data acquired at high c^* or at longer tubing delays. The C_w value assumed by the model was then varied to find the minimum residual, giving an optimal C_w value of 4 g m⁻³. The delays predicted for this C_w value are plotted in Figure 4.5.

For perfectly mixed flow in the bins, flow is modeled as a first-order process as in Equation 4.7:

$$k_f = \frac{Q}{Al} \quad (4.7)$$

where Q is the volumetric flow rate inside the tubing, A is the cross-sectional area of the tubing, and l is the length of a bin in the model (2 cm). A comparison of the concentration profiles of compounds at the tubing exit simulated assuming perfectly mixed or laminar flow is

presented in Figure 4.2. The concentration profile for laminar flow was produced using the residence time distribution $E(t)$ shown in Equation 4.8:

$$E(t) = \frac{t_m^2}{2t^3} \quad (4.8)$$

where t_m is the mean residence time and t is the time elapsed (Fogler, 2006). The error this assumption causes in transfer time through a 1 m length of tubing is generally smaller than the effect of gas-wall partitioning within the tubing and so does not affect the model results presented here.

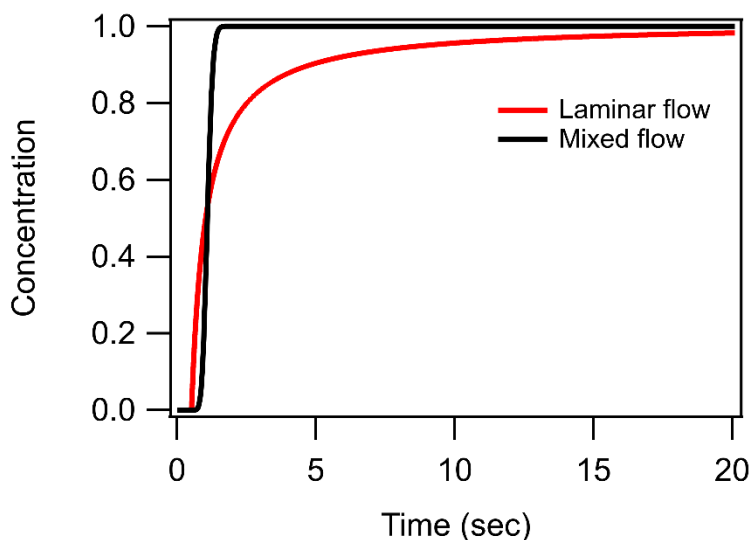


Figure 4.2. Simulated time profiles of compound concentrations at the tubing exit assuming flow in bins is perfectly mixed rather than laminar. The mixed flow profile was generated by running the model with gas-wall partitioning turned off. The profiles are for 1 m of tubing with 3/16 in. ID at a flow rate of 1 L min⁻¹.

Diffusion of compounds absorbed into the walls of the Teflon tubing is fast compared to the time scales investigated here, and thus it is not explicitly included in our model. This is similar to the assumption often made in chromatography models that diffusion within the stationary phase does not affect mass transfer within the column (Guiochon et al., 2006). Using the formulation developed by Krechmer et al. (2016), we estimate that the depth to which

organic compounds effectively partition into the Teflon tubing is 2.2 nm for the C_w value derived here. This value is consistent with our estimates for Teflon chambers, which ranged from 1.5 – 4.5 nm (Krechmer et al., 2016). Diffusion coefficients of larger organic molecules in Teflon (e.g., toluene and benzene) are $D_t \sim 2 \times 10^{-9} \text{ cm}^2 \text{ s}^{-1}$ (Tokarev et al., 2006), resulting in a time scale for diffusion in the walls of $\tau_{dw} \sim l_w^2 / D_t \sim 0.1 \text{ ms}$. This is much smaller than the minimum time scale for gas-phase diffusion and accommodation of $\sim 400 \text{ ms}$, indicating that this process is too fast to limit partitioning and thus does not need explicit representation in the model.

Using the rate constants defined above, the rates of change in concentration of compounds in the gas phase and wall compartments in bin i , $[G_i]$ and $[W_i]$, can be expressed as in Equations 4.9 and 4.10:

$$\frac{d[G_i]}{dt} = k_f[G_{i-1}] - k_f[G_i] - k_a[G_i] + k_d[W_i] \quad (4.9)$$

$$\frac{d[W_i]}{dt} = k_a[G_i] - k_d[W_i] \quad (4.10)$$

where both $[G_i]$ and $[W_i]$ are expressed in units of moles per cubic meter of air. These units are consistent with our treatment of gas-wall partitioning as being analogous to gas-particle partitioning, where the concentration of compounds in the condensed phase is represented as moles (or mass) per cubic meter of air (Pankow 1994, Donahue et al., 2006).

The model was solved numerically using the Euler method with at a time step of 1 ms and 50 bins per meter of tubing, using IGOR Pro (Wavemetrics, v7.02). Shortening the time step and/or increasing the number of bins per meter of tubing did not appreciably change the numerical results.

4.3. Results and Discussion

4.3.1. Effect of Volatility, Tubing Length, and Flow Rate on Tubing Delays. Tubing delays were measured by introducing step function changes in the concentration of organic

compounds measured by the PTR-MS, with all compounds of a homologous series being measured simultaneously, as shown in Figure 4.3. We quantify delays in this study as the amount of time required for the PTR-MS signal to achieve 90% of the total change caused by the step function change in sample concentration. As can be seen in Figure 4.3A for 2-ketones, the total (PTR-MS + tubing) delay increases with increasing compound carbon number and therefore decreasing compound volatility. This can be explained by noting that the criteria for gas-wall partitioning equilibrium is that the rates of absorption and desorption are equal throughout the system, so for tubing (a similar equation holds for the PTR-MS) this condition is everywhere given by Equation 4.11:

$$k_a[G] = k_d[W] \quad (4.11)$$

Substituting Equations 4.5 and 4.6 and rearranging, the equilibrium condition is then given by Equation 4.12:

$$[W] = \frac{C_w [G]}{c^*} \quad (4.12)$$

Since C_w , $[G]$ (the input concentration), and the rate of absorption are essentially the same for all compounds, the time required for $[W]$ to reach the equilibrium value given by Equation 4.12 increases with decreasing compound volatility. This reflects the need for the tubing to absorb a larger amount of the less volatile compounds to reach equilibrium, while only a very small amount of the more volatile species needs to be absorbed to meet that condition.

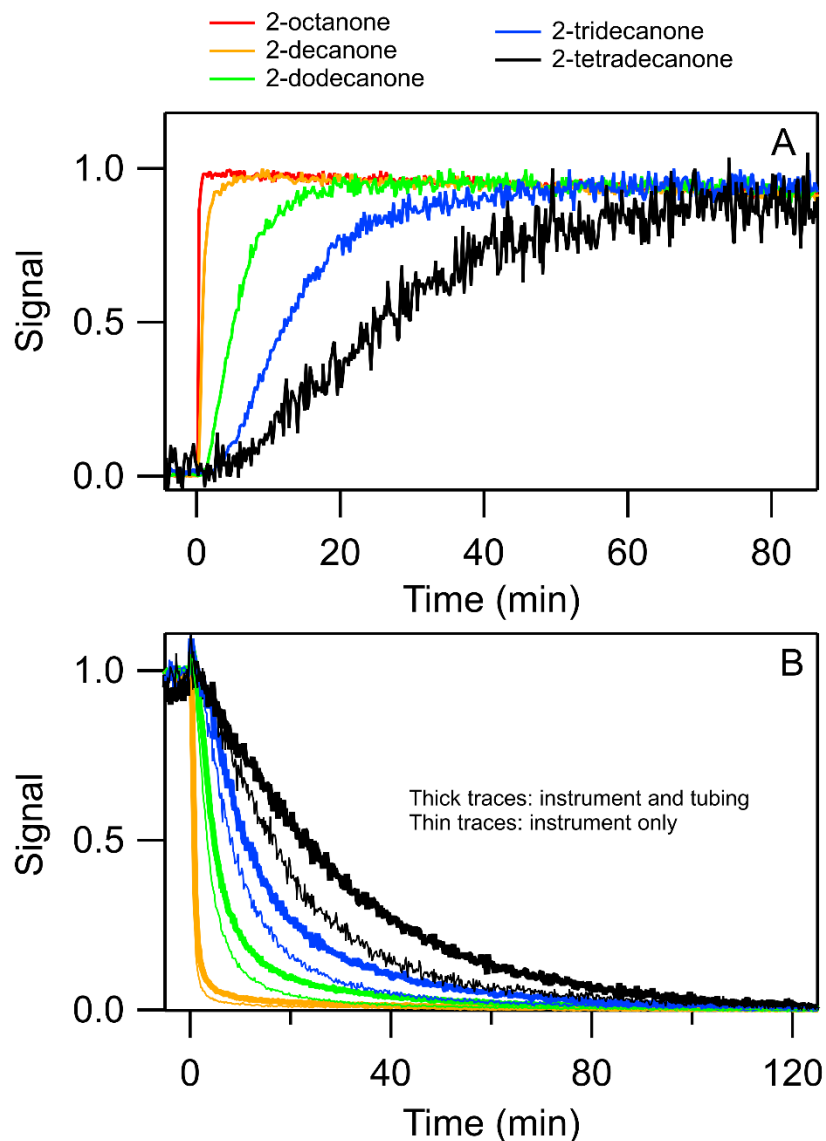


Figure 4.3. (A) PTR-MS time profiles measured in response to a step function increase in the concentration of 2-ketones. All compounds were measured simultaneously through 1 m of 3/16 in. ID PFA Teflon tubing at a flow rate of 0.36 L min^{-1} . Profiles are normalized to peak signal. The decline in signal over time is due to drift in instrument response following start-up. (B) PTR-MS time profiles measured in response to a step function decrease in the concentration of 2-ketones for tubing + PTR-MS (thick lines) and the PTR-MS alone (thin lines). The tubing used was a 3 m length of 3/16 in. ID PFA Teflon, and the flow rate for both traces was 0.36 L min^{-1} . Profiles are normalized to the equilibrium concentration measured prior to the step change. The signal-to-noise ratio is lower at higher carbon numbers due to gas-wall partitioning in the chamber lowering sample concentration as well as mass discrimination within the PTR-MS quadrupole mass analyzer. For visual clarity the traces for 2-octanone are not shown since they overlap with the traces for 2-decanone.

The effects of the PTR-MS and tubing were uncoupled by comparing the equilibration times for the PTR-MS + tubing with the equilibration time of the PTR-MS alone. The differences in equilibration times are significant and easily observed in the time profiles of 2-ketones shown in Figure 4.3B. Here we define the tubing delay as the difference in the time it takes for the signal to drop to 10% of its initial value, with and without the tubing attached to the PTR-MS. Both tubing and instrument delays are substantial.

The tubing delays measured for 2-ketones sampled through two lengths of 0.47 cm ID tubing (1 and 3 m) at a single flow rate (0.36 L min⁻¹) and through a single length of 0.47 cm ID tubing (3 m) at two flow rates (0.36 and 2.7 L min⁻¹) are shown in Figure 4.4A and Figure 4.4B, respectively. The tubing delay increases almost proportionally with tubing length, similar to the effect of column length on retention time established in the chromatography literature, captured in Equation 4.13:

$$t_r = \frac{B L}{v_f} \quad (4.13)$$

where t_r is retention time, L is column length, v_f is the bulk flow velocity, and B is a constant that incorporates the partitioning coefficient and volumes of stationary and mobile phases (Poole, 2003; Skoog et al., 2007). The tubing delay decreases as flow rate is increased (Figure 4.4B) because compounds have less time to partition to the walls, but the observed change is less than inversely proportional to the flow velocity (0.20 instead of 0.13) as predicted by Equation 4.13. This discrepancy is thought to occur because, unlike chromatography, where the time scale for absorption of compound to the walls is much shorter than the time scale for flow in the tube, in the tubing experiments the time scales are comparable.

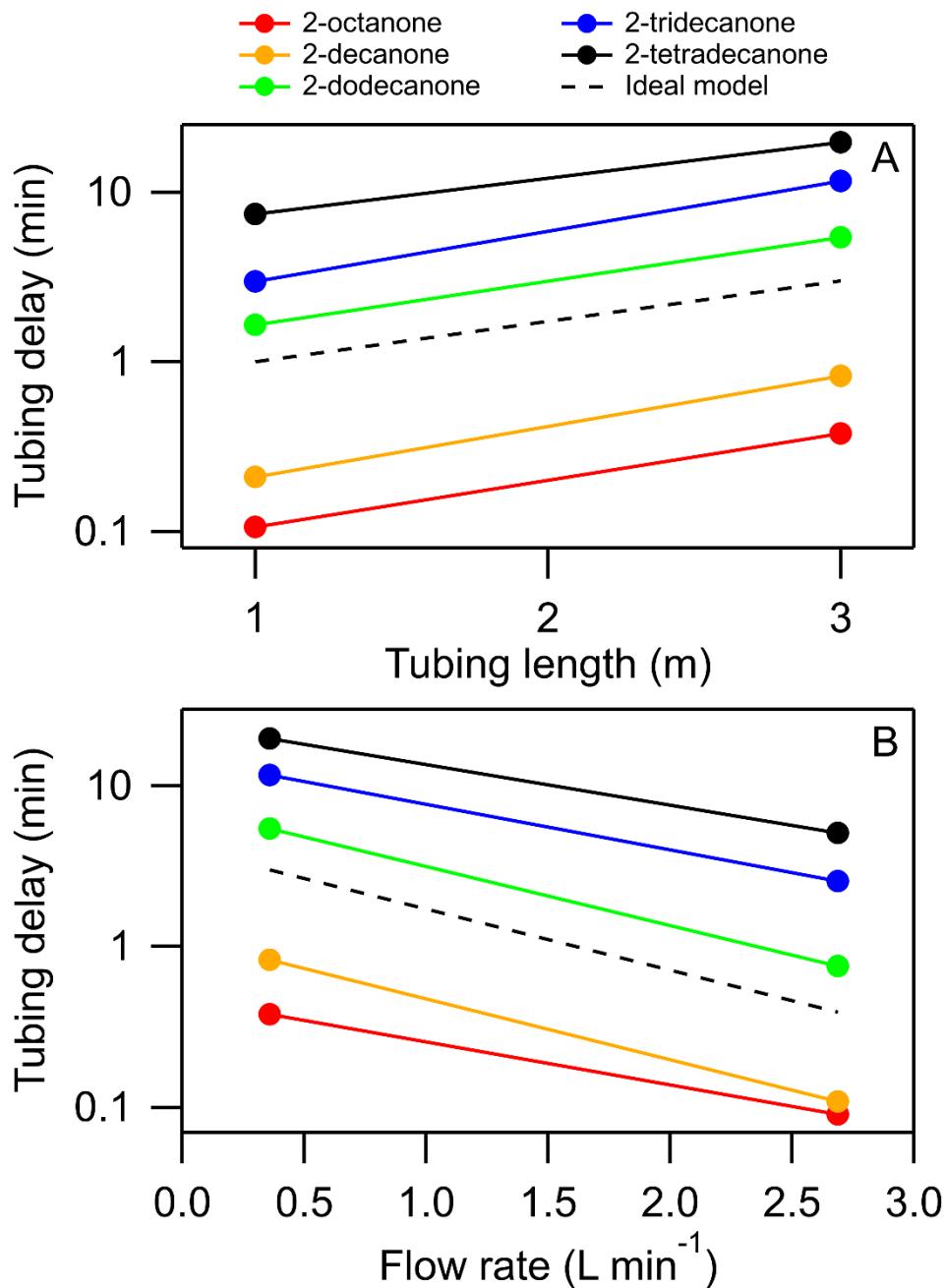


Figure 4.4. (A) Tubing delays for PTR-MS analysis of 2-ketones sampled using 1 and 3 m of 3/16 in. ID tubing at a flow rate of 0.36 L min⁻¹. The dashed line corresponds to the model case where the delay is proportional to the length of the tubing, which for these experiments is a factor of three. (B) Tubing delays for PTR-MS analysis of 2-ketones sampled using 3 m of 3/16 in. ID tubing and flow rates of 0.36 and 2.7 L min⁻¹. The dashed line corresponds to the model case where the delay is inversely proportional to the flow rate, which for these experiments is a factor of 0.13.

The dependence of tubing delays measured for 2-ketones and 1-alkenes on c^* for a range of conditions are shown in Figure 4.5. Because delays increase proportionally with increasing tubing length, they are plotted as minutes of delay per meter of tubing. Delays are inversely proportional to c^* , eventually levelling off at the residence time of the tubing when $c^* \gg C_w$ and gas-wall partitioning becomes insignificant. This trend is driven by the change in the time scale to reach partitioning equilibrium with c^* , as described in Equation 4.12. Figure 4.5 also compares model output to our experimental results, and shows that the model accurately predicts the tubing delay as a function of c^* across all functional groups, tubing lengths, and flow rates tested. No effect of functional group on tubing delay was observed, consistent with past studies of gas-wall partitioning in Teflon chambers, where compound volatility is the property that best predicts the extent of sorption (Matsunaga 2010). We note here that past work has shown that gas-wall partitioning equilibrium established in Teflon chambers is independent of sample concentration (Matsunaga and Ziemann, 2010) and relative humidity (Krechmer et al., 2017). Limited experiments conducted here were consistent with those findings, indicating that this model can be used to estimate tubing delays in both lab and field settings.

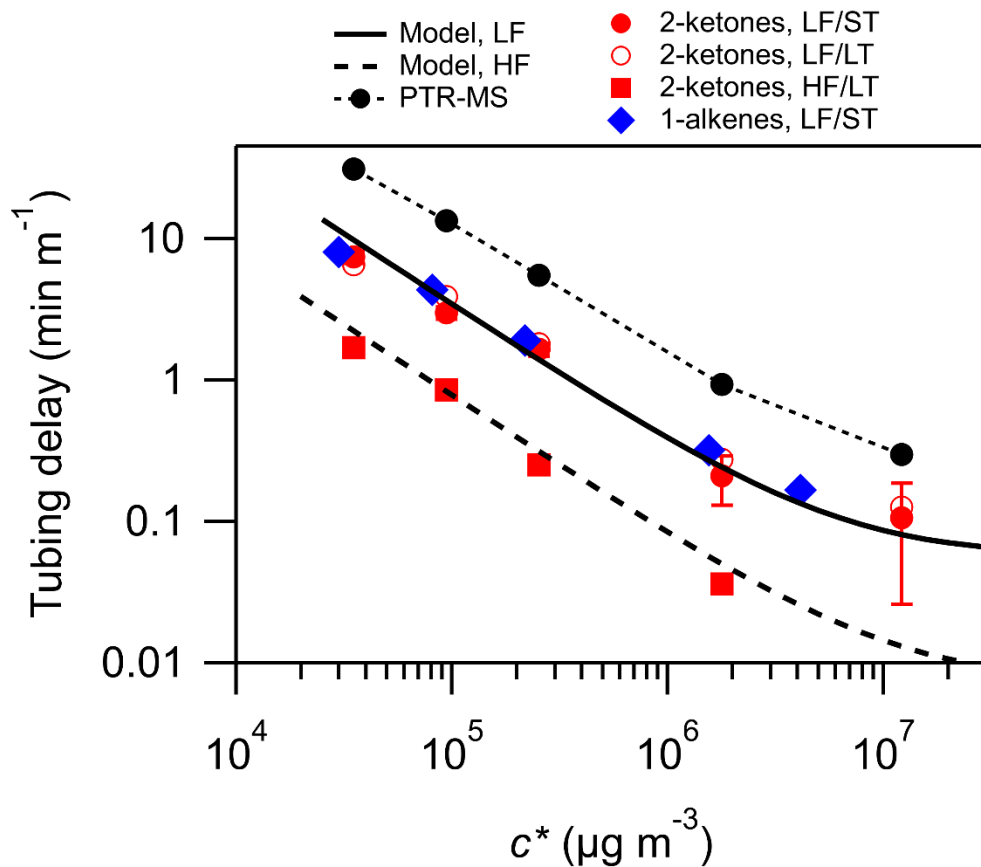


Figure 4.5. Comparison of modeled and measured tubing delays for homologous series of 2-ketones and 1-alkenes with a range of c^* values using short (ST = 1 m) and long (LT = 3 m) lengths of 3/16 in. ID tubing with low (LF = 0.36 L min⁻¹) flow, and long tubing with low and high (HF = 2.7 L min⁻¹) flow. The instrument delay for the PTR-MS is also shown. Values of c^* were calculated using SIMPOL.1 (Pankow and Asher, 2007). Error bars are only shown for the 2-ketones LF/ST case, and represent the variability (std. dev.) of the observations. Note that for the larger delays, the error bars are smaller than the data points.

Model simulations were also conducted for a range of flow rates and c^* typically encountered in laboratory and field studies. The tubing delays predicted by the model are presented in Figure 4.6 and are clearly significant, especially for organic compounds with c^* below 10⁵ μg m⁻³. The results also quantify the heuristics already being used by researchers to minimize tubing delays, which are to minimize tubing length, increase flow rate, and heat tubing. Heating tubing increases the c^* of the compounds being measured, reducing their gas-wall partitioning coefficient and thereby decreasing tubing delay. Sampling compounds through the

tubing at higher flows than necessary for instruments and dumping excess flow (oversampling) also reduces tubing delays by decreasing the time available for compounds to partition to the walls. The delays for 3/16 in. ID Teflon tubing presented in Figure 4.6 can be estimated using the empirical parameterization in Equation 4.14:

$$Delay (min m^{-1}) = \frac{3.18 \times 10^{-3}}{\frac{Q}{4.73 + Q} \times \frac{c^*}{8.11 \times 10^6 + c^*}} \quad (4.14)$$

where Q is flow rate ($L \text{ min}^{-1}$) and c^* is the saturation vapor concentration ($\mu\text{g m}^{-3}$) at the temperature of the tubing calculated using SIMPOL.1. This parameterization matches the model predictions of tubing delay within a factor of 1.2 for delays between 5 sec m^{-1} and 60 min m^{-1} across the range of flow rates and c^* plotted in Figure 4.6. We note that although the parameterization in Equation 4.14 is based on diffusion coefficients D estimated at $23 \text{ }^\circ\text{C}$, changes in D due to temperature produce only small changes in predicted delay ($\sim 10\%$ when raising temperature from $23 \text{ }^\circ\text{C}$ to $100 \text{ }^\circ\text{C}$). This effect is negligible compared to the change in delay caused by the accompanying shift in c^* (several orders of magnitude for the same temperature change), making this parameterization a useful predictive tool for the changes in tubing delay caused by changes in temperature. The parameterization does not, however, take into account changes in the absorptive properties of Teflon that may occur at lower or higher temperatures.

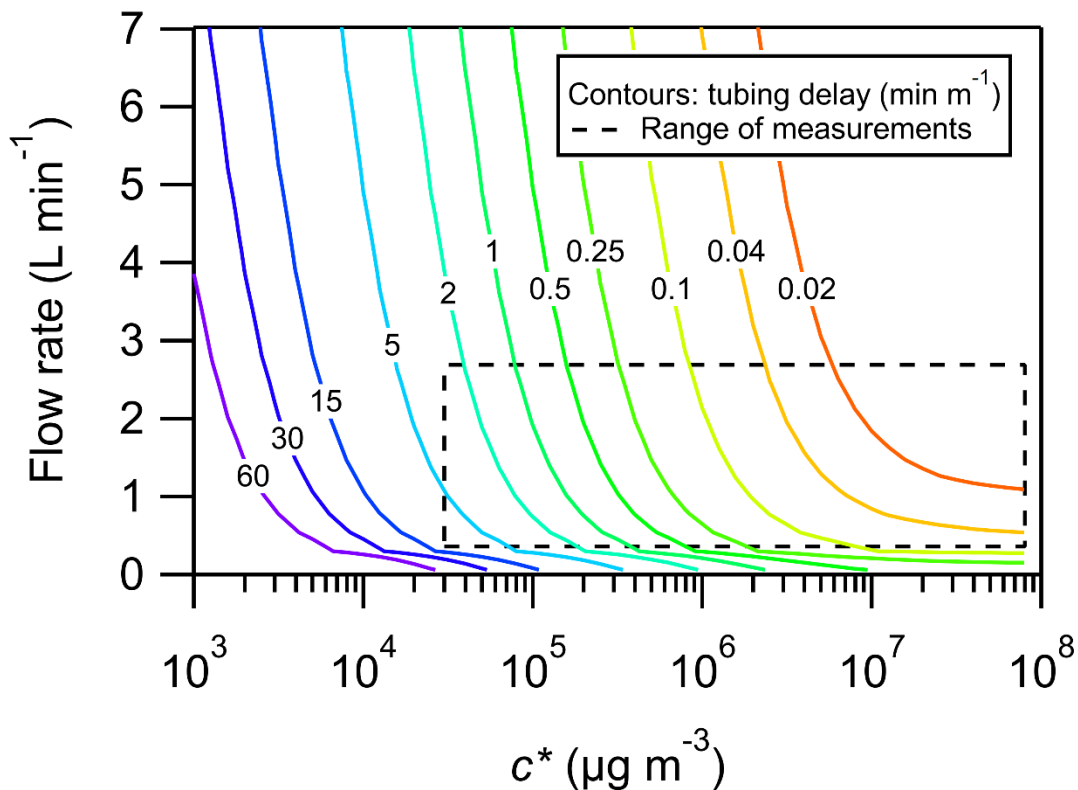


Figure 4.6. Simulated tubing delays presented as a function of c^* and flow rate for 3/16 in. ID PFA Teflon tubing. The range of conditions for measurements made in this study are shown by the dashed box. Values of c^* were calculated using SIMPOL.1 (Pankow and Asher, 2007).

4.3.2. Estimating C_w for Teflon Tubing. As mentioned above, the value of C_w used in the model for the 0.47 cm ID PFA Teflon tubing was estimated by fitting the model predictions to the experimental data in Figure 4.5. The optimal value for C_w was 4 g m^{-3} (grams of absorbing phase per m^3 of internal tube volume). In order to directly compare C_w in tubing and chambers one must correct for differences in the surface area to volume ratios. Since we model gas-wall partitioning as occurring within a finite depth at the surface of the Teflon tubing or chamber, the volume of Teflon into which partitioning occurs is the product of the Teflon surface area (SA) and the partitioning depth (δ). C_w can then be expressed as in Equation 4.15:

$$C_w = \frac{SA \delta \rho}{V} \quad (4.15)$$

where ρ is the density of Teflon and V is the volume of gas exposed to the given surface area of Teflon. The equivalent wall mass measured for tubing can then be scaled for comparison with chamber values using Equation 4.16:

$$C_{w,ch} = C_{w,t} \frac{SA_{ch} V_t \delta_{ch} \rho_{ch}}{SA_t V_{ch} \delta_t \rho_t} \quad (4.16)$$

where the subscripts ch and t denote the chamber and tubing. As discussed above, $\delta_{ch}/\delta_t \sim 0.7-2$, and since PFA (tubing) and FEP (chambers) Teflon have the same density, $\rho_{ch}/\rho_t = 1$.

When scaled according to Equation 4.16, the value of $C_{w,t} = 4 \text{ g m}^{-3}$ reported above is equivalent to $\sim 10-30 \text{ mg m}^{-3}$ of liquid organic aerosol in an 8 m^3 chamber. This is comparable to the values of C_w determined in FEP Teflon chambers: 16 mg m^{-3} for 1-alkenes and 24 and 78 mg m^{-3} for 2-ketones (Matsunaga and Ziemann, 2010; Yeh and Ziemann, 2015), where values from Matsunaga and Ziemann (2010) were recalculated with c^* values obtained using SIMPOL.1 (Pankow and Asher, 2007). The similarity in C_w values indicates that gas-wall partitioning of organic compounds is similar for PFA and FEP Teflon. We also note that since gas-wall partitioning in tubing depends on C_w (Equation 4.6), and since estimates of C_w depend on the method used to estimate compound vapor pressures, researchers applying the results of this work to other compounds should use SIMPOL.1 to estimate c^* values, even when measured vapor pressures are available.

4.3.3. Effect of Tubing Diameter on Tubing Delays. We find that tubing delays are shortest for small diameter tubing, provided that flow rate or Reynolds number is held constant. When the tubing is being depassivated following a step-function decrease in sample concentration one can treat the residence time of compound in the walls of the tubing (τ_w) as the limiting step in depassivation. By substituting Equations 4.4, 4.6 and 4.14 into Equation 4.5 one

arrives at an expression for the residence time of a compound in the walls of the tubing given in Equation 4.17:

$$\tau_w = \frac{C_w}{k_a c^*} = \frac{\delta_t \rho_t d_t}{2 c^* D_g} \quad (4.17)$$

which shows a linear relationship between τ_w and tubing diameter. While this approach is clearly a simplification and ignores the effect of flow rate on the rate of equilibration, we show in Figure 4.7 that our numerical model also predicts a linear relationship between tubing delay and tubing diameter when flow rate is held constant. This linear relationship also aligns well with our experimental results. In Figure 4.8 we present tubing delays and model results for 1/16 and 3/16 in. ID tubing. In the region where delays are dominated by gas-wall partitioning inside the tubing ($c^* < 10^6 \mu\text{g m}^{-3}$) we observe that modeled and measured delays are three times longer for 3/16 in. ID tubing compared to 1/16 in. ID tubing. This relationship breaks down at higher volatilities ($c^* > 10^6 \mu\text{g m}^{-3}$) since $c^* > C_w$, and the extent of gas-wall partitioning is small, giving very short residence times in the walls. With this in mind, one can conclude that tubing delays scale directly with tubing diameter at a constant flow rate when delays are larger than a few seconds.

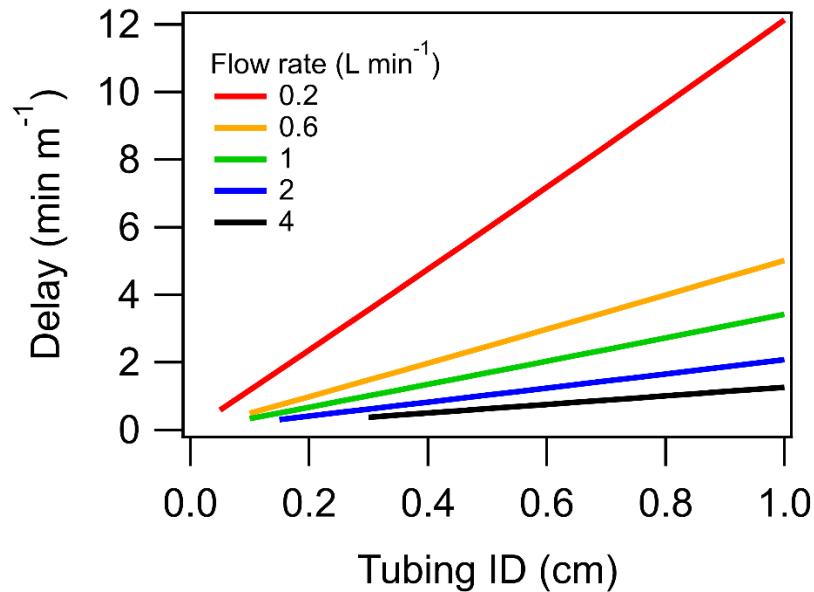


Figure 4.7. Simulated tubing delays presented as a function of tubing ID at various flow rates for a compound with $c^* = 10^5 \mu\text{g m}^{-3}$ sampled through PFA tubing.

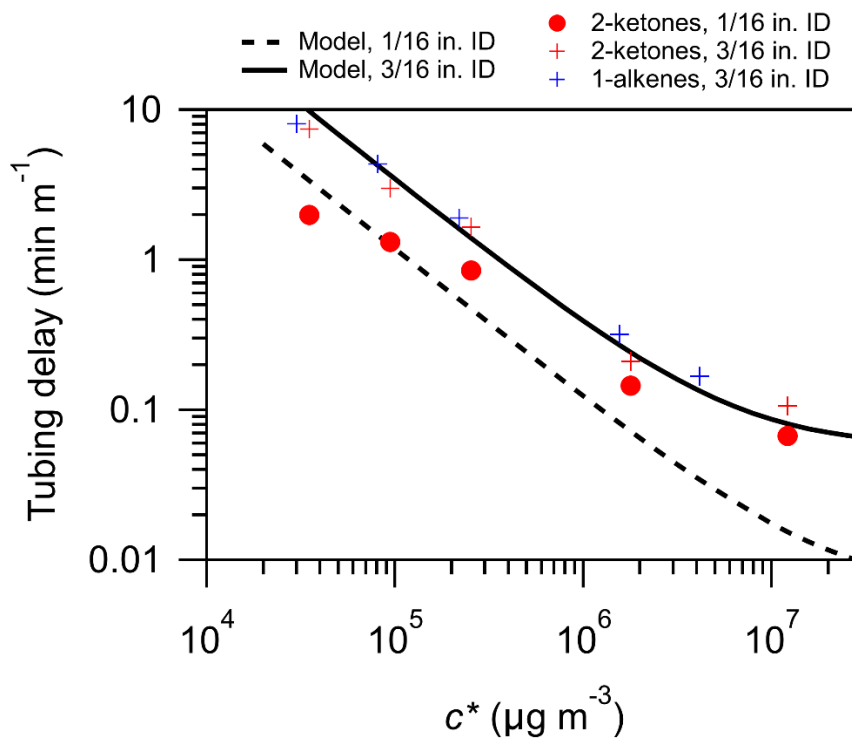


Figure 4.8. Comparison of measured and modeled tubing delays for 1/16 in. ID and 3/16 ID PFA Teflon tubing sampling at 0.36 L min^{-1} . Values of c^* were calculated using SIMPOL.1 (Pankow and Asher, 2008).

To quantify the effect of simultaneous changes in tubing diameter and flow rate we generated model predictions of tubing delay for a compound with $c^* = 10^5 \mu\text{g m}^{-3}$ across a range of tubing diameters and flow rates. These results are presented in Figure 4.9, and provide guidance for designing a sampling system that minimizes tubing delay. As expected, the model predictions indicate that smaller diameter tubing has shorter tubing delays when flow rate or Reynolds number is held constant. The results in Figure 4.9 also suggest that one may be able to reduce tubing delays by sampling under turbulent flow conditions. We did not attempt to quantify delays under such conditions, however, in part due to the larger pressure drops experienced in that flow regime, which are undesirable under many circumstances.

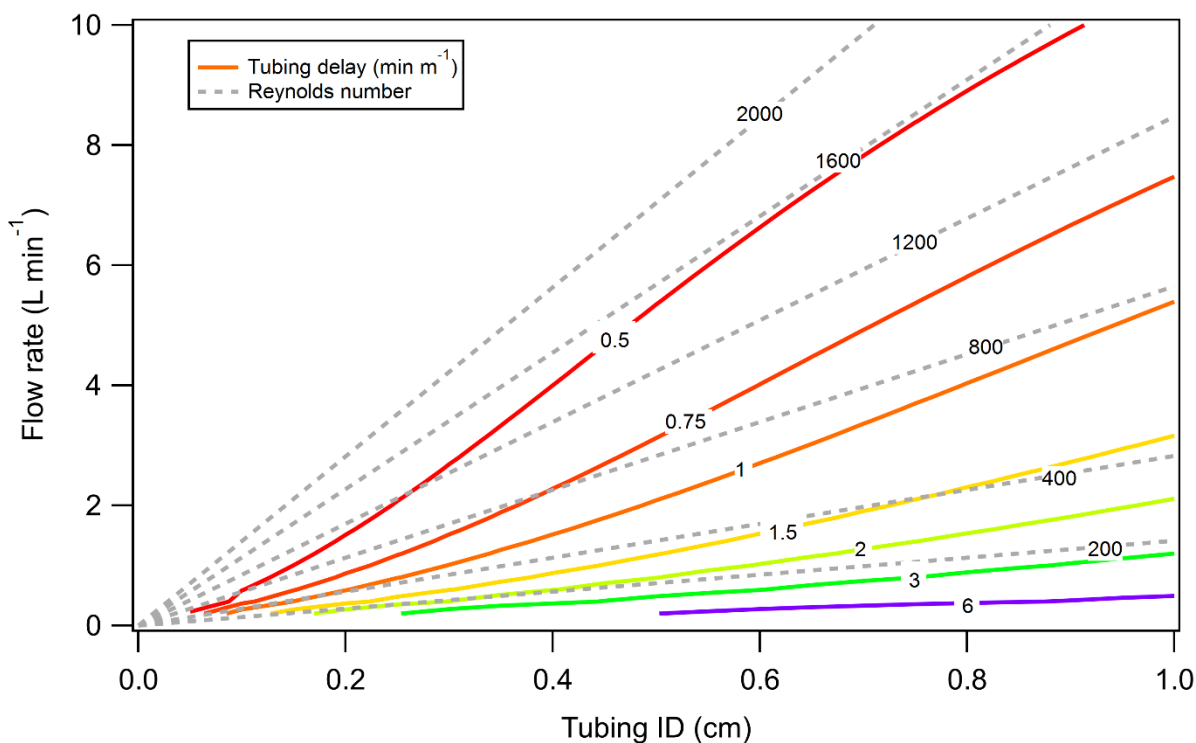


Figure 4.9. Simulated tubing delays presented as a function of tubing ID and flow rate for a compound with $c^* = 10^5 \mu\text{g m}^{-3}$ sampled through PFA tubing. Reynolds numbers are overlaid to illustrate the nonlinear relationship between tubing delay, flow rate and tubing diameter.

4.3.4. Effect of Instrumentation on Delays. In these experiments gas-wall partitioning inside the PTR-MS was the largest source of delay. We used the PTR-MS time profiles shown in Figure 4.3B to quantify the dependence of this delay on c^* , and the results are shown with the tubing delays in Figure 4.5. The instrument delays observed for the PTR-MS are significant, equivalent to several meters of Teflon tubing. This amount of Teflon is significantly larger than the size of the PTR-MS inlet, indicating that the surfaces inside the PTR-MS are stickier than Teflon. We encourage others to use this method to determine delays caused by their particular instrument across the range of volatilities being measured. This volatility-dependent response function is important for interpreting the time profiles of compounds being measured, since it sets the lower limit for how fast the instrument can respond to sudden changes in concentration. One can convolve the tubing model output $F(t)$ with the instrument response function $I(t)$ to obtain the instrument response $R(t)$, as in Equation 4.18.

$$R(t) = F(t) * I(t) = \int_0^{\infty} [F(t - \tau) \times I(\tau)] d\tau \quad (4.18)$$

This approach was evaluated by sampling a set of 2-ketones from an equilibrated environmental chamber into the PTR-MS in a 60 s pulse, with the PTR-MS sampling clean air before and after the pulse. The experiment was conducted with 1 m of 3/16 in. ID PFA tubing sampling at 0.36 L min^{-1} . As seen in Figure 4.10, the convolution of the model output with the instrument response function for each 2-ketone gives excellent agreement with the experimental data. For example, a 60 s pulse of 2-tridecanone is convoluted to a response lasting more than 20 min, underscoring the importance of accounting for both tubing and instrument delays.

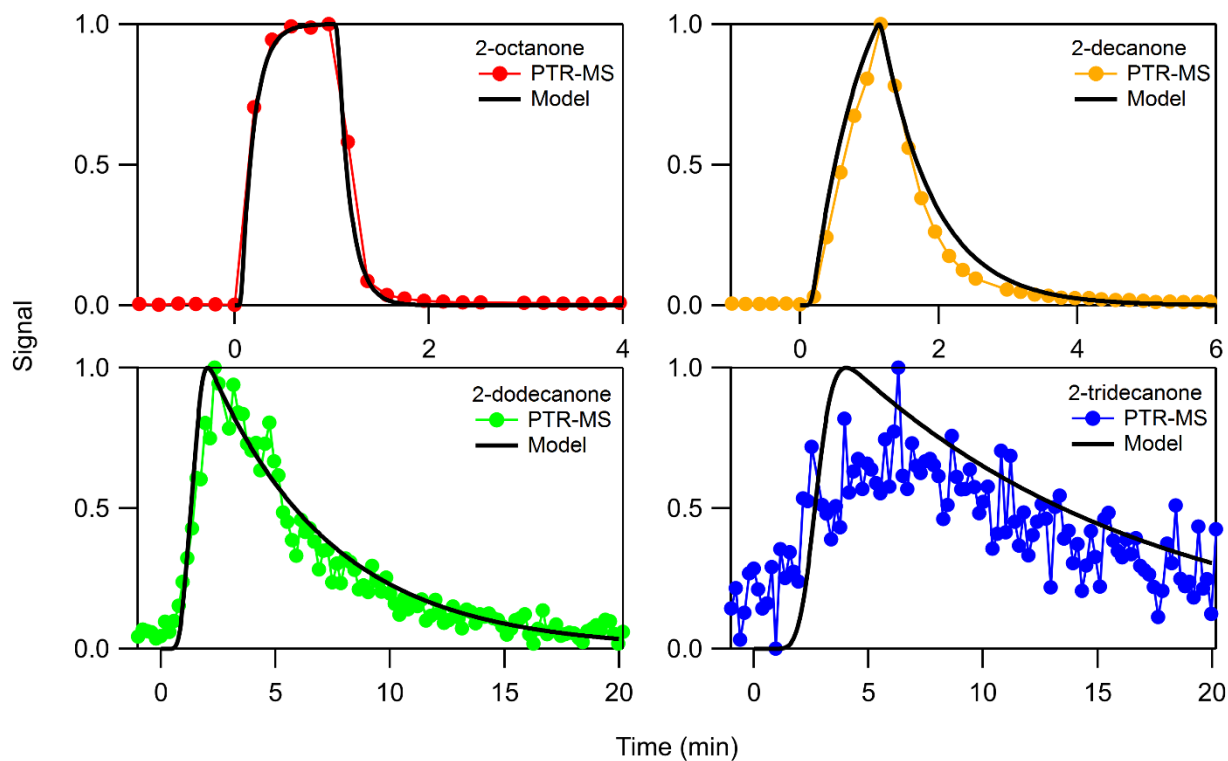


Figure 4.10. Measured and modeled time series for a 60-second pulse of 2-ketones measured by the PTR-MS through 1 m of 3/16 in. ID PFA Teflon tubing at 0.36 L min^{-1} . The tubing model output was convolved with the instrument response function for each 2-ketone to generate the traces.

After the experiments described in this work were completed we removed all extraneous tubing from the inlet of the PTR-MS in an attempt to minimize the instrument response time for future work. This was a success, and we decreased the instrument response time by a factor of 5 by reconfiguring the inlet. This result again shows the importance of minimizing the total amount of tubing in a sampling configuration when fast instrument response is needed.

4.4. Conclusions

We found that gas-wall partitioning of organic compounds inside Teflon tubing significantly affects time-resolved measurements of compounds with saturation concentration (c^*) below $10^7 \mu\text{g m}^{-3}$. The compounds measured in this study (SIMPOL.1-calculated c^* values

ranging from $3 \times 10^4 \mu\text{g m}^{-3}$ to $1 \times 10^7 \mu\text{g m}^{-3}$) are all expected to exist entirely in the gas phase in the atmosphere (Donahue et al, 2006). We found that measurements of compounds in this volatility range were significantly affected by delays caused by partitioning to the walls of the tubing and the PTR-MS. We modeled the delays caused by Teflon tubing using a simple chromatography model and the gas-wall partitioning framework of Matsunaga and Ziemann (2010). This model accurately predicts tubing delays across all compound volatilities, functional groups, tubing lengths and diameters, and flow rates tested. The measurements and model simulations indicate that delays can shift compound time profiles by minutes to hours – time scales that are highly relevant to both laboratory and atmospheric measurements.

A potential application of these delays is for estimating compound saturation concentration, even when the identity of the compound is unknown. Past work has proposed using desorption kinetics inside an inlet as a technique for identifying compounds (Schuhfried et al., 2012), and the model presented here can be used in a similar way. Another possible application is to induce time separation among different compounds that are otherwise indistinguishable to the analytical instrumentation (e.g., compounds with the same accurate mass in CIMS; Stark et al., 2015), since the c^* of multifunctional compounds with the same molecular formula can often differ by 5 orders-of-magnitude (Krechmer et al., 2015). The separation in time can then be exploited via manual analyses or factor analysis techniques (e.g., Ulbrich et al., 2009). This is equivalent to a “poor-person’s chromatography,” but using ambient temperature and Teflon surfaces that avoid thermal decomposition of multifunctional species that can occur in gas chromatography due to use of high temperatures (Stark et al., 2017).

Accounting for tubing and instrument delays is especially important in circumstances where concentrations of the compounds are changing rapidly, including eddy covariance

measurements, mobile platforms such as aircraft, rapidly changing emission sources such as fires or motor vehicle exhaust, and fast processes such as chemical reactions and gas-particle-wall partitioning. As CIMS techniques continue to be developed for detecting multifunctional organic compounds, extra care must be taken to minimize the impact that tubing and instrument surfaces have on measurements since these compounds are especially sticky.

Based on our results, we recommend that studies measuring intermediate volatility and semivolatile compounds ($c^* < 10^6 \mu\text{g m}^{-3}$) minimize the length of Teflon tubing used; and since increased flow rates and smaller tubing diameters also help to mitigate tubing delays, use the fastest flow rate in the smallest diameter tubing that still maintains laminar flow. We also recommend that researchers determine the volatility-dependent time response function of their instrument. This sets the lower limit for the response time for a given compound and allows for deconvolution of the effects of gas-wall partitioning in the instrument from those in the inlet tubing. The instrument response function can then be convolved with the output of the model presented in this study to correct for delay artifacts caused by gas-wall partitioning in Teflon tubing. This method can also be used to characterize other tubing materials, the effect of temperature and other variables, and enable improved inlet system designs.

Chapter 5

Thesis Conclusions

This thesis presents three studies of the physical and chemical processes that govern the transport and transformation of organic compounds in indoor and outdoor environments. Chapter 2 presents results of a study of the reactions of a hydroperoxyaldehyde (AHPA) in SOA. AHPA was found to cyclize rapidly, establishing equilibrium between a cyclic peroxyhemiacetal and a ring-open hydroperoxyaldehyde in approximately 3 minutes. The equilibrium constant for this cyclization reaction was measured to be 2.6. Following cyclization, the peroxide functionality of AHPA in SOA decomposes at a rate of 17% per hour when organic seed aerosol is used, a result consistent with past studies of other peroxide-containing SOA. The decomposition rate is dependent on the acid content and phase state of the SOA, with sulfuric acid / dioctyl sebacate (DOS) seed aerosol promoting the complete decomposition of AHPA in 30 minutes, while aqueous sulfuric acid / ammonium sulfate seed aerosol showed the same AHPA decomposition rate as DOS seed. This result indicates that the sulfuric acid in aqueous seed aerosol is not available to catalyze decomposition reactions in the organic phase of phase-separated SOA. Several decomposition pathways of AHPA are proposed, including bimolecular Baeyer-Villiger oxidation, concerted elimination of hydrogen or alkyl groups from the cyclic peroxyhemiacetal, and acid-catalyzed decomposition of the peroxyhemiacetal and peroxyacetal form of AHPA. Most notable is the incorporation of alcohols from the SOA into the structure of AHPA as ester and acetal groups, indicating that as peroxide-rich HOMs decompose in SOA they may form large oligomers. The insights provided by this study into the chemistry of multifunctional

hydroperoxides in SOA advance our knowledge of how oligomers form in SOA, improving our ability to predict SOA yields, composition, and lifetime in the atmosphere.

Chapter 3 of this thesis presents the results of a six-week indoor air quality study at the University of Colorado Art Museum, including the emission rates, deposition velocities, and chemical reactions of organic compounds. Human VOC emission factors were determined during a high-occupancy event and were found to agree within a factor of two with prior studies that used similar methodology. The emission factors that do not agree within a factor of two are explained by the difference in outdoor air quality and the activities conducted in each environment, with the emission factors for ethanol, monoterpenes, and ozone-squalene oxidation products explained by increased alcohol consumption, reduced personal care product use, and lower ozone concentrations, respectively. Following the application of paint to a gallery wall, emission factors were quantified for VCPs in paint. Using a simple box model of the museum's HVAC system, the deposition velocities of organic compounds to museum surfaces was determined as a function of volatility, with compounds having C^* below $10^8 \mu\text{g m}^{-3}$ showing measurable partitioning to the surfaces. The reaction rate of ozone inside an art gallery was found to be highly variable in time, with reactions with gallery surfaces, occupants, and NO all serving as the primary loss process under different conditions. On average, reaction with surfaces, NO, occupants, and NO₂ contributed 62%, 31%, 5%, and 2% to ozone loss, respectively. The deposition velocities of ozone to surfaces and to occupants were within the ranges previously reported in the literature, and we note that in the conditions observed in the museum, ozone deposition to occupants could not be quantified accurately if reactions with NO_x were not taken into account. The oxidation rates of VOCs in the museum were estimated using a simple box model, and the measured concentration of HOMs from limonene ozonolysis were

found to be consistent with the model predictions of limonene oxidation rate. Additionally, the predicted SOA yield of limonene HOMs was within the measurement uncertainty of the PM₁ in the museum. The results of this study will enable future predictions of indoor air quality based on outdoor air quality, building ventilation rates, occupancy levels, occupant activities, and indoor VCP use.

In Chapter 4 results are presented of a study examining the impact of gas-surface partitioning of organic compounds on measurements of gas-phase organic compounds. Delays in instrument response times due to gas-wall partitioning of organic compounds in Teflon tubing can be described using a simple chromatography model, where the partitioning of a given compound is determined by the compound's C^* and the equivalent absorbing mass (C_w) of the tubing. Using this model, the C_w for PFA Teflon tubing was found to be 4 g m^{-3} , causing delays of seconds to minutes in instrument response for compounds with $C^* < 10^7 \text{ } \mu\text{g m}^{-3}$. This value of C_w for PFA Teflon tubing is consistent with values of C_w measured in FEP Teflon chambers, indicating that the surface properties of the two materials are similar. The chromatography model presented in this chapter accurately predicted delays in instrument response time across all flow rates, tubing diameters, tubing lengths, and analyte functional groups tested. Increasing flow rate, decreasing tubing diameter, and decreasing tubing length all shorten delay times when all other parameters are held constant. No effect of functional groups on tubing delays was observed. The output of the model presented in this chapter can be convolved with an instrument response function to predict the measured time series of a compound that has significant instrument and tubing delays. The results of this study will enable better design of inlets and instruments, allowing for faster instrument response timescales and improved measurements of gas-phase organic compounds with C^* below $10^7 \text{ } \mu\text{g m}^{-3}$.

This thesis presents advances in knowledge of the chemistry of multifunctional hydroperoxides in secondary organic aerosol; the emission, deposition, and chemistry of organic compounds in the indoor environment; and the effect of gas-surface partitioning on measurements of gas-phase organic compounds. In all of these research areas there is still much to be learned, and future work should examine: 1) the effect of aerosol phase on acid and metal-ion catalysis, including Fenton chemistry; 2) the rates and products of Baeyer-Villager chemistry in peroxide-rich SOA; 3) the fate of VOCs sorbed to surfaces in the indoor environment; 4) gas-wall partitioning in additional tubing materials besides Teflon; and 5) mathematical techniques to deconvolve tubing and instrument delays from measured time series.

References

- Aimanant, S. and P. J. Ziemann. 2013a. Development of spectrophotometric methods for the analysis of functional groups in oxidized organic aerosol. *Aerosol Sci. Technol.*, 47:581–591. doi:10.1080/02786826.2013.773579.
- Aimanant, S. and P. J. Ziemann. 2013b. Chemical mechanisms of aging of aerosol formed from the reaction of n-pentadecane with OH radicals in the presence of NO_x. *Aerosol Sci. Technol.*, 47:979–990. doi:10.1080/02786826.2013.804621.
- Alwarda, R., S. Zhou, and J. P. D. Abbatt. 2018. Heterogeneous oxidation of indoor surfaces by gas-phase hydroxyl radicals. *Indoor Air*, 00:1-10.
- Antonovskii, V. L. and V. A. Terent'ev. 1967. Effect of the structure of hydroperoxides and some aldehydes on the kinetics of the noncatalytic formation of α-hydroxy peroxides. *Zhurnal Org. Khimii*, 3:1011–1015.
- Arey, J., A. M. Winer, R. Atkinson, S. M. Aschmann, W. D. Long, C. L. Morrison, and D. M. Olszyk. 1991. Terpenes emitted from agricultural species found in California's Central Valley. *J. Geophys. Res.*, 96:9329-9336.
- Atkinson, R. 1997. Gas-phase tropospheric chemistry of volatile organic compounds: 1. Alkanes and alkenes. *J. Phys. Chem. Ref. Data*, 26:215–290. doi:10.1063/1.556012.
- Atkinson, R., and J. Arey. 2003. Atmospheric degradation of volatile organic compounds. *Chem. Rev.*, 103:4605–4638. doi:10.1021/cr0206420.
- Bennett, D. H., and E. J. Furtaw. 2004. Fugacity-based indoor residential pesticide fate model. *Environ. Sci. Technol.*, 38:2142-2152.
- Bertram, A. K., S. T. Martin, S. J. Hanna, M. L. Smith, A. Bodsworth, Q. Chen, M. Kuwata, A. Liu, Y. You, and S. R. Zorn. 2011. Predicting the relative humidities of liquid-liquid

- phase separation, efflorescence, and deliquescence of mixed particles of ammonium sulfate, organic material, and water using the organic-to-sulfate mass ratio of the particle and the oxygen-to-carbon elemental ratio of the organic component. *Atmos. Chem. Phys.*, 11:10995–11006. doi:10.5194/acp-11-10995-2011.
- Bertram, T. H., J. R. Kimmel, T. A. Crisp, O. S. Ryder, R. L. N. Yatawelli, J. A. Thornton, M. J. Cubison, M. Gonin, and D. R. Worsnop. 2011. A field-deployable, chemical ionization time-of-flight mass spectrometer. *Atmos. Meas. Tech.*, 4:1471-1479.
- Bian, Q., A. A. May, S. M. Kreidenweis, and J. R. Pierce. 2015. Investigation of particle and vapor wall-loss effects on controlled wood-smoke smog-chamber experiments. *Atmos. Chem. Phys.*, 15:11027-11045. doi:10.5194/acp-15-11027-2015.
- Borisova, I. A., V. I. Kadentsev, S. S. Zlotskii, O. S. Chizhov, M. R. Skurko, D. L. Rakhmankulov and R. A. Karakhanov. 1981. Behavior of acetals under chemical ionization conditions. *Russ. Chem. Bull.*, 30:1219–1224. doi:10.1007/BF01417976.
- Bruckner, R. 2002. *Advanced Organic Chemistry*. Harcourt/Academic Press, San Diego, CA, USA.
- Burkholder, J. B., S. P. Sander, J. Abbatt, J. R. Barker, R. E. Huie, C. E. Kolb, M. J. Kurylo, V. L. Orkin, D. M. Wilmouth, and P. H. Wine. 2015. *Chemical Kinetics and Photochemical Data for Use in Atmospheric Studies, Evaluation No. 18*. JPL Publication 15-10, Jet Propulsion Laboratory, Pasadena, CA.
- Capouet, M., J. F. Müller, K. Ceulemans, S. Compennolle, L. Vereecken, and J. Peeters. 2008. Modeling aerosol formation in alpha-pinene photo-oxidation experiments. *J. Geophys. Res.*, 113:D02308. doi:10.1029/2007JD008995.

Chemours: Teflon FEP fluoroplastic film:

https://www.chemours.com/Teflon_Industrial/en_US/assets/downloads/teflon-fep-film-properties.pdf Accessed July 2017.

Clegg, S. L., P. Brimblecombe, and A. S. Wexler. 1998. A thermodynamic model of the system $H^+ - NH_4^+ - Na^+ - SO_4^{2-} - NO_3^- - Cl^- - H_2O$ at 298.15 K. *J. Phys. Chem. A*, 102:2155–2171. doi:10.1021/jp973043j.

Coggon, M. M., B. C. McDonald, A. Vlasenko, P. R. Veres, F. Bernard, A. R. Koss, B. Yuan, J. B. Gilman, J. Peischl, K. C. Aikin, J. DuRant, C. Warneke, S. M. Li, and J. A. de Gouw. 2018. Diurnal variability and emission pattern of decamethylcyclopentasiloxane (D₅) from the application of personal care products in two North American cities. *Environ. Sci. Technol.*, 52:5610-5618.

Crouse, J. D., L. B. Nielsen, S. Jørgensen, H. G. Kjaergaard, and P. O. Wennberg. 2013. Autoxidation of organic compounds in the atmosphere. *J. Phys. Chem. Lett.*, 4:3513–3520. doi:10.1021/jz4019207.

de Gouw, J. and C. Warneke. 2007. Measurements of volatile organic compounds in the Earth's atmosphere using proton-transfer-reaction mass spectrometry. *Mass Spec. Rev.*, 26:223–257. doi:10.1002/mas.20119.

Docherty, K. S. and P. J. Ziemann. 2003. Effects of stabilized Criegee intermediate and OH radical scavengers on aerosol formation from reactions of β -pinene with O₃. *Aerosol Sci. Technol.*, 37:877–891. doi:10.1080/027868203000930.

Docherty, K. S. and P. J. Ziemann. 2006. Reaction of oleic acid particles with NO₃ radicals: Products, mechanism, and implications for radical-initiated organic aerosol oxidation. *J. Phys. Chem. A*, 110:3567–3577. doi:10.1021/jp0582383.

- Docherty, K. S., W. Wu, Y. B. Lim, and P. J. Ziemann. 2005. Contributions of organic peroxides to secondary aerosol formed from reactions of monoterpenes with O₃. *Environ. Sci. Technol.*, 39:4049–4059. doi:10.1021/es050228s.
- Donahue, N. M., G. T. Drozd, S. A. Epstein, A. A. Presto, and J. H. Kroll. 2011. Adventures in ozoneland: Down the rabbit-hole. *Phys. Chem. Chem. Phys.*, 13:10848–10857. doi:10.1039/c0cp02564j.
- Donahue, N. M., A. L. Robinson, C. O. Stainer, and S. N. Pandis. 2006. Coupled partitioning, dilution, and chemical aging of semivolatile organics. *Environ. Sci. Technol.*, 40:2635–2643. doi:10.1021/es052297c.
- Duncan, S. M., K. G. Sexton, and B. J. Turpin. 2017. Oxygenated VOCs, aqueous chemistry, and potential impacts on residential indoor air composition. *Indoor Air*, 28:198-212.
- Durham, L. J., C. F. Wurster, and H. S. Mosher. 1958. Peroxides. VIII. The Mechanism for the thermal decomposition of n-butyl hydroperoxide and n-butyl 1-hydroxybutyl peroxide. *J. Am. Chem. Soc.*, 80:332–337. doi:10.1021/ja01535a020.
- Ehn, M., E. Kleist, H. Junninen, T. Petäjä, G. Lönn, S. Schobesberger, M. Dal Maso, A. Trimborn, M. Kulmala, D. R. Worsnop, A. Wahner, J. Wildt, and T. F. Mentel. 2012. Gas phase formation of extremely oxidized pinene reaction products in chamber and ambient air. *Atmos. Chem. Phys.*, 12:5113–5127. doi:10.5194/acp-12-5113-2012.
- Ehn, M., J. A. Thornton, E. Kleist, M. Sipilä, H. Junninen, I. Pullinen, M. Springer, F. Rubach, R. Tillmann, B. Lee, F. Lopez-Hilfiker, S. Andres, I. H. Acir, M. Rissanen, T. Jokinen, S. Schobesberger, J. Kangasluoma, J. Kontkanen, T. Nieminen, T. Kurtén, L. B. Nielsen, S. Jørgensen, H. G. Kjaergaard, M. Canagaratna, M. Dal Maso, T. Berndt, T. Petäjä, A. Wahner, V.M. Kerminen, M. Kulmala, D. R. Worsnop, J. Wildt, and T. F. Mentel. 2014.

- A large source of low-volatility secondary organic aerosol. *Nature*, 506:476–479.
doi:10.1038/nature13032.
- Epstein, S. A., S. L. Blair, and S. A. Nizkorodov. 2014. Direct photolysis of α -pinene ozonolysis secondary organic aerosol: Effect on particle mass and peroxide content. *Environ. Sci. Technol.*, 48:11251–11258. doi:10.1021/es502350u.
- Fadeyi, M. O., C. J. Weschler, K. W. Tham, and Z. M. Sultan. 2013. Impact of human presence on secondary organic aerosols derived from ozone-initiated chemistry in a simulated office environment. *Environ. Sci. Technol.*, 47:3933-3941.
- Fischer, A., E. Ljungstrom, and S. Langer. 2013. Ozone removal by occupants in a classroom. *Atmos. Environ.*, 314:11-17.
- Fogler, S. H. 2006. Elements of chemical reaction engineering, 4th ed., Prentice Hall, Upper Saddle River, NJ
- Friedel, R. A., and A. G. Sharkey. 1956. Mass spectra of acetal-type compounds. *Anal. Chem.*, 28:940–944. doi:10.1021/ac60114a004.
- Gao, S., M. Keywood, N. L. Ng, J. Surratt, V. Varutbangkul, R. Bahreini, R. C. Flagan, and J. H. Seinfeld. 2004. Low-molecular-weight and oligomeric components in secondary organic aerosol from the ozonolysis of cycloalkenes and α -pinene. *J. Phys. Chem. A*, 108:10147–10164. doi:10.1021/jp047466e.
- Gao, Y., W. A. Hall, and M. V. Johnston. 2010. Molecular composition of monoterpene secondary organic aerosol at low mass loading. *Environ. Sci. Technol.*, 44:7897–7902. doi:10.1021/es101861k.
- Gligorovski, S. 2016. Nitrous acid (HONO): An emerging indoor pollutant. *J. Photochem. Photobiol. A*, 314:1-5.

- Griesbaum, K., and J. Neumeister. 1982. Ozonolysis of symmetrically 1,2-disubstituted ethylenes in HCl/methanol solutions: Acid catalyzed reactions of primary cleavage products. *Chem. Berichte-Recueil*, 115:2697–2706. doi:10.1002/cber.19821150803.
- Grosjean, D. 1985. Wall loss of gaseous pollutants in outdoor Teflon chambers. *Environ. Sci. Technol.*, 79:1059–1065. doi:10.1021/es00141a006.
- Guiochon, G., A. Felinger, D. G. Shirazi, and A. M. Katti. 2006. *Fundamentals of Preparative and Nonlinear Chromatography*, 1st ed., Elsevier Inc, San Diego, CA.
- Guo, H., J. Liu, K. D. Froyd, J. M. Roberts, P. R. Veres, P. L. Hayes, J. L. Jimenez, A. Nenes, and R. J. Weber. 2017. Fine particle pH and gas–particle phase partitioning of inorganic species in Pasadena, California, during the 2010 CalNex campaign. *Atmos. Chem. Phys.*, 17:5703–5719. doi:10.5194/acp-17-5703-2017.
- Guo, H., L. Xu, A. Bougiatioti, K. M. Cerully, S. L. Capps, J. R. Hite Jr., A. G. Carlton, S.-H. Lee, M. H. Bergin, N. L. Ng, A. Nenes, and R. J. Weber. 2015. Fine-particle water and pH in the southeastern United States. *Atmos. Chem. Phys.*, 15:5211–5228. doi:10.5194/acp-15-5211-2015.
- Hallquist, M., J. C. Wenger, U. Baltensperger, Y. Rudich, D. Simpson, M. Claeys, J. Dommen, N. M. Donahue, C. George, A. H. Goldstein, J. F. Hamilton, H. Herrmann, T. Hoffmann, Y. Iinuma, M. Jang, M. E. Jenkin, J. L. Jimenez, A. Kiendler-Scharr, W. Maenhaut, G. McFiggans, T. F. Mentel, A. Monod, A. S. H. Prévôt, J. H. Seinfeld, J. D. Surratt, R. Szmigielski, and Wildt, J. 2009. The formation, properties and impact of secondary organic aerosol: Current and emerging issues. *Atmos. Chem. Phys.*, 9:5155–5236. doi:10.5194/acp-9-5155-2009.

- Hayes, M. J., and D. C. Pepper. 1961. The solubility of H₂SO₄ in 1,2-dichloroethane. *Trans. Farad. Soc.*, 57:432–435. doi:10.1039/TF9615700432.
- Holzinger, R., J. Williams, F. Herrmann, J. Lelieveld, N. M. Donahue, and T. Rockmann. 2010. Aerosol analysis using a Thermal-Desorption Proton-Transfer-Reaction Mass Spectrometer (TD-PTR-MS): A new approach to study processing of organic aerosols. *Atmos. Chem. Phys.*, 10:2257–2267. doi:10.5194/acp-10-2257-2010.
- Huang, Y., R. Zhao, S. M. Charan, C. M. Kenseth, X. Zhang, and J. H. Seinfeld. 2018. Unified theory of vapor-wall mass transport in Teflon-walled environmental chambers. *Environ. Sci. Technol.*, 52:2134-2142.
- James, D. H. and C. S. G. Phillips. 1954. The chromatography of gases and vapours. Part III. The determination of adsorption isotherms, *J. Chem. Soc.*, 1066–1070.
- Jimenez, J. L., M. R. Canagaratna, N. M. Donahue, A. S. H. Prevot, Q. Zhang, J. H. Kroll, P. F. DeCarlo, J. D. Allan, H. Coe, N. L. Ng, A. C. Aiken, K. S. Docherty, I. M. Ulbrich, A. P. Grieshop, A. L. Robinson, J. Duplissy, J. D. Smith, K. R. Wilson, V. A. Lanz, C. Hueglin, Y. L. Sun, J. Tian, A. Laaksonen, T. Raatikainen, J. Rautiainen, E. J. Dunlea, J. A. Huffman, T. B. Onasch, M. R. Alfarra, P. I. Williams, K. Bower, P. Vaattovaara, M. Ehn, M. Kulmala, J. M. Tomlinson, D. R. Collins, M. J. Cubison, Y. Kondo, J. Schneider, F. Drewnick, S. Borrmann, S. Weimer, K. Demerjian, D. Salcedo, L. Cottrell, R. Griffin, A. Takami, T. Miyoshi, S. Hatakeyama, A. Shimono, J. Y Sun, Y. M. Zhang, K. Dzepina, J. R. Kimmel, D. Sueper, J. T. Jayne, S. C. Herndon, A. M. Trimborn, L. R. Williams, E. C. Wood, A. M. Middlebrook, C. E. Kolb, U. Baltensperger, and D. R. Worsnop. 2009. Evolution of organic aerosols in the atmosphere. *Science*, 326:1525-1529.

Jimenez Group Publications: Pagonis AMT tubing model.

http://cires1.colorado.edu/jimenez/group_pubs.html, last access: November 2017.

Jokinen, T., M. Sipila, H. Junninen, M. Ehn, G. Lonn, J. Hakala, T. Petaja, R. L. Mauldin III, M.

Kulmala, and D. R. Worsnop. 2012. Atmospheric sulphuric acid and neutral cluster measurements using CI-API-TOF. *Atmos. Chem. Phys.*, 12:4117-4125.

Jokinen, T., M. Sipila, S. Richters, V.-M. Kerminen, P. Paasonen, F. Stratman, D. Worsnop, M.

Kulmala, M. Ehn, H. Herrmann, and T. Berndt. 2014. Rapid autoxidation forms highly oxidized RO₂ radicals in the atmosphere. *Angew. Chem.*, 53:14596-14600.

Jokinen, T., T. Berndt, R. Makkonen, V. Kerminen, H. Junninen, P. Paasonen, F. Stratmann, H.

Herrmann, A. B. Guenther, D. R. Worsnop, M. Kulmala, M. Ehn, and M. Sipila. 2015.

Production of extremely low volatile organic compounds from biogenic emissions: Measured yields and atmospheric implications. *Proc. Nat. Acad. Sci.*, 112:7123-7128.

Klepeis, N. E., W. C. Nelson, W. R. Ott, J. P. Robinson, A. M. Tsang, P. Switzer, J. V. Behar, S.

C. Hern, and W. H. Engelmann. 2001. The national human activity pattern survey (NHAPS): A resource for assessing exposure to environmental pollutants. *J. Exp. Sci. & Environ. Epidemiol.*, 11:231-252.

Krapf, M., I. El Haddad, E. A. Bruns, U. Molteni, K. R. Daellenbach, A. S. H. Prévôt, U.

Baltensperger, and J. Dommen. 2016. Labile peroxides in secondary organic aerosol. *Chem*, 1:603–616. doi:10.1016/j.chempr.2016.09.007.

Krechmer, J.E., M. M. Coggon, P. Massoli, T. B. Nguyen, J. D. Crouse, W. Hu, D. A. Day, G.

S. Tyndall, D. K. Henze, J. C. Rivera-Rios, J. B. Nowak, J. R. Kimmel, R. L. Mauldin, H.

Stark, J. T. Jayne, M. Sipilä, H. Junninen, J. St. Clair, X. Zhang, P. A. Feiner, W. H.

Brune, F. N. Keutsch, P. O. Wennberg, J. H. Seinfeld, D. R. Worsnop, J. L. Jimenez, and

- M. R. Canagaratna. 2015. Formation of low volatility organic compounds and secondary organic aerosol from isoprene hydroxyhydroperoxide low-NO oxidation. *Environ. Sci. Technol.*, 49:10330-10339. doi:10.1021/acs.est.5b02031.
- Krechmer, J. E., D. Pagonis, P. J. Ziemann, and J. L. Jimenez. 2016. Quantification of gas-wall partitioning in Teflon environmental chambers using rapid bursts of low-volatility oxidized species generated in situ. *Environ. Sci. Technol.*, 50:5757–5765. doi:10.1021/acs.est.6b00606.
- Krechmer, J. E., D. A. Day, P. J. Ziemann, and J. L. Jimenez. 2017. Direct measurements of gas/particle partitioning and mass accommodation coefficients in environmental chambers. *Environ. Sci. Technol.*, 51:11867–11875. doi:10.1021/acs.est.7b02144.
- Krechmer, J., F. Lopez-Hilfiker, A. Koss, M. Hutterli, C. Stoermer, B. Deming, J. Kimmel, C. Warneke, R. Holzinger, J. Jayne, D. Worsnop, K. Fuhrer, M. Gonin, and J. de Gouw. 2018. Evaluation of a new reagent-ion source and focusing ion-molecule reactor for use in proton-transfer-reaction mass spectrometry. *Anal. Chem.*
- Kristensen, K., Å. K. Watne, J. Hammes, A. Lutz, T. Petäjä, M. Hallquist, M. Bilde, and M. Glasius. 2016. High-molecular weight dimer esters are major products in aerosols from α -pinene ozonolysis and the boreal forest. *Environ. Sci. Technol. Lett.*, 3:280–285. doi:10.1021/acs.estlett.6b00152.
- Kypri, K., J. Langley, and S. Stephenson. 2005. Episode-centred analysis of drinking to intoxication in university students. *Alcohol Alcohol.*, 40:447-452.
- La, Y. S., M. Camredon, P. J. Ziemann, R. Valorso, A. Matsunaga, V. Lannuque, J. Lee-Taylor, A. Hodzic, S. Madronich, and B. Aumont. 2016. Impact of chamber wall loss of gaseous organic compounds on secondary organic aerosol formation: Explicit modeling of SOA

- formation from alkane and alkene oxidation. *Atmos. Chem. Phys.*, 16:1417–1431.
doi:10.5194/acp-16-1417-2016.
- Lin, S. T., L. L. Tien, and N. C. Chang. 1989. Mass spectra of some acetals. *Analyst*, 114:1083–1085. doi:10.1039/AN9891401083.
- Liu, S., R. Li, R. J. Wild, C. Warneke, J. A. de Gouw, S. S. Brown, S. L. Miller, J. C. Luongo, and P. J. Ziemann. 2016. Contribution of human-related sources to indoor volatile organic compounds in a university classroom. *Indoor Air*, 26:925-938.
- Liu, S., S. L. Thompson, H. Stark, P. J. Ziemann, and J. L. Jimenez. 2017. Gas-phase carboxylic acids in a university classroom: Abundance, variability, and sources. *Environ. Sci. Technol.*, 51:5454-5463.
- Matsunaga, A. and P. J. Ziemann. 2009. Yields of β -hydroxynitrates and dihydroxynitrates in aerosol formed from OH radical-initiated reactions of linear alkenes in the presence of NO_x. *J. Phys. Chem. A*, 113:599–606. doi:10.1021/jp807764d.
- Matsunaga, A. and P. J. Ziemann. 2010. Gas-wall partitioning of organic compounds in a Teflon film chamber and potential effects on reaction product and aerosol yield measurements. *Aerosol Sci. Technol.*, 44:881–892. doi:10.1080/02786826.2010.501044.
- McDonald, B. C., J. A. de Gouw, J. B. Gilman, S. H. Jathar, A. Akherati, C. D. Cappa, J. L. Jimenez, J. Lee-Taylor, P. L. Hayes, S. A. McKeen, Y. Y. Cui, S. Kim, D. R. Gentner, G. Isaacman-VanWertz, A. H. Goldstein, R. A. Harley, G. J. Frost, J. M. Roberts, T. B. Ryerson, and M. Trainer. 2018. Volatile chemical products are emerging as largest petrochemical source of urban organic emissions. *Science*, 359:760-764.
- McGillen, M. R., B. F. E. Curchod, R. Chhantyal-Pun, J. M. Beames, N. Watson, M. A. H. Khan, L. McMahon, D. E. Shallcross, and A. J. Orr-Ewing. 2017. Criegee intermediate-

- alcohol reactions, a potential source of functionalized hydroperoxides in the atmosphere. *Earth Space Chem.*, 1:664–672. doi:10.1021/acsearthspacechem.7b00108.
- McLafferty, F. W. 2012. *Mass Spectrometry of Organic Ions*. Fourth Ed. University Science Books, Sausalito, CA, USA.
- McMurry, P. H. and M. R. Stolzenburg. 1987. Mass accommodation coefficients from penetration measurements in laminar tube flow. *Atmos. Environ.*, 21:1231–1234. doi:10.1016/0004-6981(87)90251-4.
- McVay, R. C., C. D. Cappa, and J. H. Seinfeld. 2014. Vapor-wall deposition in chambers: Theoretical considerations. *Environ. Sci. Technol.*, 48:10251–10258. doi:10.1021/es502170j.
- Mertes, P., L. Pfaffenberger, J. Dommen, M. Kalberer, and U. Baltensperger. 2012. Development of a sensitive long path absorption photometer to quantify peroxides in aerosol particles (Peroxide-LOPAP). *Atmos. Meas. Tech.*, 5:2339–2348. doi:10.5194/amt-5-2339-2012.
- Mikoviny, T., L. Kaser, and A. Wisthaler. 2010. Development and characterization of a High-Temperature Proton-Transfer-Reaction Mass Spectrometer (HT-PTR-MS). *Atmos. Meas. Tech.*, 3: 537–544. doi:10.5194/amt-3-537-2010.
- Müller, L., M. C. Reinnig, J. Warnke, and T. Hoffmann. 2008. Unambiguous identification of esters as oligomers in secondary organic aerosol formed from cyclohexene and cyclohexene/ α -pinene ozonolysis. *Atmos. Chem. Phys.*, 8:1423–1433. doi:10.5194/acp-8-1423-2008.
- Mutzel, A., L. Poulain, T. Berndt, Y. Iinuma, M. Rodigast, O. Böge, S. Richters, G. Spindler, M. Sipila, T. Jokinen, M. Kulmala, and H. Herrmann. 2015. Highly oxidized

- multifunctional organic compounds observed in tropospheric particles: A field and laboratory study. *Environ. Sci. Technol.*, 49:7754–7761. doi:10.1021/acs.est.5b00885.
- Orlando, J. J. and G. S. Tyndall. 2012. Laboratory studies of organic peroxy radical chemistry: an overview with emphasis on recent issues of atmospheric significance. *Chem. Soc. Rev.*, 41:6294–6317. doi:10.1039/c2cs35166h.
- Pagonis, D., J. E. Krechmer, J. de Gouw, J. L. Jimenez, and P. J. Ziemann. 2017. Effects of gas–wall partitioning in Teflon tubing and instrumentation on time-resolved measurements of gas-phase organic compounds. *Atmos. Meas. Tech.*, 10:4687-4696.
- Pankow, J. F. and W. E. Asher. 2008. SIMPOL.1: A simple group contribution method for predicting vapor pressures and enthalpies of vaporization of multifunctional organic compounds. *Atmos. Chem. Phys.* 8:2773-2796. doi:10.5194/acpd-7-11839-2007.
- Pankow, J. F.: An absorption model of gas/particle partitioning of organic compounds in the atmosphere, *Atmos. Environ.*, 28, 185–188, doi:10.1016/1352-2310(94)90093-0, 1994.
- Park, J. H., A. H. Goldstein, J. Timkovsky, S. Fares, R. Weber, J. Karlik, and R. Holzinger. 2013. Eddy covariance emission and deposition flux measurements using proton transfer reaction - time of flight - mass spectrometry (PTR-TOF-MS): Comparison with PTR-MS measured vertical gradients and fluxes. *Atmos. Chem. Phys.*, 13:1439–1456, doi:10.5194/acp-13-1439-2013.
- Peng, Z., D. A. Day, H. Stark, R. Li, B. B. Palm, W. H. Brune, J. L. Jimenez. 2015. HO_x radical chemistry in oxidation flow reactors with low-pressure mercury lamps systematically examined by modeling. *Atmos. Meas. Tech.*, 8:4863–4890. doi:10.5194/amt-8-4863-2015.
- Poole, C. F. 2003. *The Essence of Chromatography*, 1st ed., Elsevier, Boston, MA.

- Pope III, C. A., R. T. Burnett, D. Krewski, M. Jerrett, Y. Shi, E. E. Calle, and M. J. Thun. 2009. Cardiovascular mortality and exposure to airborne fine particulate matter and cigarette smoke. *Circulation*, 120:941-948.
- Praske, E., R. V. Otkjær, J. D. Crouse, J. C. Hethcox, B. M. Stoltz, H. G. Kjaergaard, and P. O. Wennberg. 2018. Atmospheric autoxidation is increasingly important in urban and suburban North America. *Proceed. Natl. Acad. Sci. USA*, 115:64–69. doi:10.1073/pnas.1715540115.
- Ranney, A. P. and P. J. Ziemann. 2016. Kinetics of acid-catalyzed dehydration of cyclic hemiacetals in organic aerosol particles in equilibrium with nitric acid vapor. *J. Phys. Chem. A*, 120:2561–2568. doi:10.1021/acs.jpca.6b01402.
- Ranney, A. P. and P. J. Ziemann. 2017 Identification and quantification of oxidized organic aerosol compounds using derivatization, liquid chromatography, and chemical ionization mass spectrometry. *Aerosol Sci. Technol.*, 51:342–353. doi:10.1080/02786826.2016.1271108.
- Raventos-Duran, T., M. Camderon, R. Valorso, C. Mouchel-Vallon, and B. Aumont. 2010. Structure-activity relationships to estimate the effective Henry's law constants of organics of atmospheric interest. *Atmos. Chem. Phys.*, 10:7643-7654.
- Reiss, R., P. B. Ryan, and P. Koutrakis. 1994. Modeling ozone deposition onto indoor residential surfaces. *Environ. Sci. Technol.*, 28:303-307.
- Riva, M., S. H. Budisulistiorini, Z. Zhang, A. Gold, J. A. Thornton, B. J. Turpin, and J. D. Suratt. 2017. Multiphase reactivity of gaseous hydroperoxide oligomers produced from isoprene ozonolysis in the presence of acidified aerosols. *Atmos. Environ.*, 152:314–322. doi:10.1016/j.atmosenv.2016.12.040.

- Sander, S. P., R. R. Friedl, D. M. Golden, M. J. Kurylo, R. E. Huie, V. L. Orkin, B. J. Finlayson-Pitts. 2003. Chemical kinetics and photochemical data for use in atmospheric studies. JPL Publication 02-05.
- Schay, G. and G. Szekely. 1954. Gas adsorption measurements in flow systems. *Acta Chim.*, 5:167-182.
- Schuhfried, E., E. Aprea, L. Cappellin, C. Soukoulis, R. Viola, T. D. Märk, F. Gasperi, and F. Biasioli. 2012. Desorption kinetics with PTR-MS: Isothermal differential desorption kinetics from a heterogeneous inlet surface at ambient pressure and a new concept for compound identification. *Int. J. Mass Spectrom.*, 314:33–41, doi:10.1016/j.ijms.2012.01.013.
- Schwarzenbach, R. P., P. M. Gschwend, and D. M. Imboden. 2003. Environmental Organic Chemistry. JohnWiley & Sons, Inc., Hoboken, NJ, USA.
- SDBSWeb : <http://sdb.sdb.aist.go.jp> National Institute of Advanced Industrial Science and Technology. Accessed December 2017.
- Shiraiwa, M., L. D. Yee, K. A. Schilling, C. L. Loza, J. S. Craven, A. Zuend, P. J. Ziemann, and J. H. Seinfeld. 2013. Size distribution dynamics reveal particle-phase chemistry in organic aerosol formation. *Proc. Natl. Acad. Sci. U. S. A.*, 110:11746–11750. doi:10.1073/pnas.1307501110.
- Skoog, D. A., F. J. Holler, and S. R. Crouch. 2007. Principles of Instrumental Analysis, Cengage Learning, Boston, MA..
- Stark, H., B. M. Lerner, R. Schmitt, R. Jakoubek, E. J. Williams, T. B. Ryerson, F. C. Fehsenfeld. 2007. Atmospheric in situ measurement of nitrate radical (NO₃) and other

- photolysis rates using spectroradiometry and filter radiometry. *J. Geophys. Res. Atmos.*, 112:D10.
- Stark, H., R. L. N. Yatavelli, S. L. Thompson, J. R. Kimmel, M. J. Cubison, P. S. Chhabra, M. R. Canagaratna, J. T. Jayne, D. R. Worsnop, and J. L. Jimenez. 2015. Methods to extract molecular and bulk chemical information from series of complex mass spectra with limited mass resolution. *Int. J. of Mass Spectrom.*, 389:26-38.
doi:10.1016/j.ijms.2015.08.011.
- Stark, H., R. L. N. Yatavelli, S. L. Thompson, H. Kang, J. E. Krechmer, J. R. Kimmel, B. B. Palm, W. Hu, P. L. Hayes, D. A. Day, P. Campuzano Jost, M. R. Canagaratna, J. T. Jayne, D. R. Worsnop, and J. L. Jimenez. 2017. Impact of thermal decomposition on thermal desorption instruments: advantage of thermogram analysis for quantifying volatility distributions of organic species. *Environ. Sci. Technol.*, 51:8491-8500.
doi:10.1021/acs.est.7b00160.
- Stein, S.E. 2016. Mass Spectra., in NIST Chemistry WebBook, NIST Standard Reference Database Number 69, Eds. Linstrom, P. J. and Mallard, W. G., National Institute of Standards and Technology, Gaithersburg, MD 20899.
- Tang, X., P. K. Misztal, W. W. Nazaroff, and A. H. Goldstein. 2015. Siloxanes are the most abundant volatile organic compound emitted from engineering students in a classroom. *Environ. Sci. Technol. Lett.*, 2:303-307.
- Tang, X., P. K. Misztal, W. W. Nazaroff, and A. H. Goldstein. 2016. Volatile organic compound emissions from humans indoors. *Environ. Sci. Technol.*, 50:12686-12694.
- Tobias, H. J. and P. J. Ziemann. 2000. Thermal desorption mass spectrometric analysis of organic aerosol formed from reactions of 1-tetradecene and O₃ in the presence of

- alcohols and carboxylic acids. *Environ. Sci. Technol.*, 34:2105–2115.
doi:10.1021/es9907156.
- Tobias, H. J. and P. J. Ziemann. 2001. Kinetics of the gas-phase reactions of alcohols, aldehydes, carboxylic acids, and water with the C13 stabilized Criegee intermediate formed from ozonolysis of 1-tetradecene. *J. Phys. Chem. A*, 105:6129–6135. doi:10.1021/jp004631r.
- Tobias, H. J., P. M. Kooiman, K. S. Docherty, and P. J. Ziemann. 2000. Real-time chemical analysis of organic aerosols using a thermal desorption particle beam mass spectrometer. *Aerosol Sci. Technol.*, 33:170–190. doi:10.1080/027868200410912.
- Tokarev, A., K. Friess, J. Machkova, M. Šipek, Yu. Yampolskii. 2006. Sorption and diffusion of organic vapors in amorphous Teflon AF2400. *J. Polymer Sci. B*, 44:832–844.
doi:10.1002/polb.20725.
- Tucker, W. A. and L. H. Nelken. 1982. Diffusion coefficients in air and water, in Handbook of Chemical Property Estimation Methods, edited by Lyman, W. J., Reehl, W. F., and Rosenblatt, D. H., McGraw-Hill, New York, NY., 17.1-17.35.
- Ulbrich, I. M., M. R. Canagaratna, Q. Zhang, D. R. Worsnop, and J. L. Jimenez. Interpretation of organic components from positive matrix factorization of aerosol mass spectrometric data. *Atmos. Chem. Phys.*, 9:2891-2918. doi:10.5194/acp-9-2891-2009.
- Veres, P. R., P. Faber, F. Drewnick, J. Lelieveld, and J. Williams. 2013. Anthropogenic sources of VOC in a football stadium: Assessing human emissions in the atmosphere. *Atmos. Environ.*, 77:1025-1059.
- Vinnik, M. I. and P. A. Obratsov. 1990. The mechanism of the dehydration of alcohols and the hydration of alkenes in acid solution. *Russ. Chem. Rev.*, 59:63–77.
doi:10.1070/RC1990v059n01ABEH003510.

- Waring, M. S., and J. R. Wells. 2015. Volatile organic compound conversion by ozone, hydroxyl radicals, and nitrate radicals in residential indoor air: Magnitudes and impacts of oxidant sources. *Atmos. Environ.*, 106:382-391.
- Warneke, C., J. A. De Gouw, W. C. Kuster, P. D. Goldan, and R. Fall. 2003. Validation of atmospheric VOC measurements by proton-transfer-reaction mass spectrometry using a gas-chromatographic preseparation method. *Environ. Sci. Technol.*, 37:2494–2501. doi:10.1021/es026266i.
- Warneke, C., J. A. de Gouw, J. S. Holloway, J. Peischl, T. B. Ryerson, E. Atlas, D. Blake, M. Trainer, and D. D. Parrish. 2012. Multiyear trends in volatile organic compounds in Los Angeles, California: Five decades of decreasing emissions. *J. Geophys. Res.*, 117:D00V17.
- Weschler, C. J., and N. Carslaw. 2018. Indoor chemistry. *Environ. Sci. Technol.*, 52:2419-2428.
- Weschler, C. J., and W. W. Nazaroff. 2017. Growth of organic films on indoor surfaces. *Indoor Air.*, 27:1101-1112.
- Wexler, A. S. and S. L. Clegg. 2002. Atmospheric aerosol models for systems including the ions H^+ , NH_4^+ , Na^+ , SO_4^{2-} , NO_3^- , Cl^- , Br^- , and H_2O . *J. Geophys. Res.*, 107:ACH14.1–ACH14.14. doi:10.1029/2001JD000451.
- Wisthaler, A., and C. J. Weschler. 2010. Reactions of ozone with human skin lipids: Sources of carbonyls, dicarbonyls, and hydroxycarbonyls in indoor air. *Proc. Nat. Acad. Sci. U.S.A.*, 107:6568-6575.
- Won, D., R. Corsi, and M. Rynes. 2001. Sorptive interactions between VOCs and indoor materials. *Indoor Air*, 11:246-256.

- Wong, J. P. S., N. Carslow, R. Zhao, S. Zhou, and J. P. D. Abbatt. 2017. Observations and impacts of bleach washing on indoor chlorine chemistry. *Indoor Air*, 27:1082-1090.
- Wong, M. K. C., B. K. Scott, and C. M. Peterson. 1992. Breath acetaldehyde following ethanol consumption. *Alcohol*, 9:189-192.
- Wright, B. M., T. P. Jones, and A. W. Jones. 1975. Breath alcohol analysis and the blood : breath ratio. *Med. Sci. Law*, 15:205-210.
- Wurster, C. F., L. J. Durham, and H. S. Mosher. 1958. Peroxides. VII. The thermal decomposition of primary hydroperoxides. *J. Am. Chem. Soc.*, 80:327–331.
doi:10.1021/ja01535a019.
- Ye, P., X. Ding, J. Hakala, V. Hofbauer, E. S. Robinson, and N. M. Donahue. 2016. Vapor wall loss of semi-volatile organic compounds in a Teflon chamber. *Aerosol Sci. Technol.*, 50:822–834. doi:10.1080/02786826.2016.1195905.
- Yeh, G. K. and P. J. Ziemann. 2015. Gas-wall partitioning of oxygenated organic compounds: Measurements, structure–activity relationships, and correlation with gas chromatographic retention factor. *Aerosol Sci. Technol.*, 49:727–738.
doi:10.1080/02786826.2015.1068427.
- Yi-Yan, N., R. M. Felder, and W. J. Koros. Selective permeation of hydrocarbon gases in poly(tetrafluoroethylene) and poly(fluoroethylene-propylene) copolymer. *J. Appl. Polym. Sci.*, 25:1755–1774. doi:10.1002/app.1980.070250822.
- Zelikman, E. S., Y. N. Yur'ev, L. B. Berezova, and V. K. Tsyskovskii. 1971. Ozonolysis of olefins in the presence of aliphatic alcohols and acids. *Zhurnal Org. Khimii*, 7:633–636.

- Zhang, X., R. H. Schwantes, R. C. McVay, H. Lignell, M. M. Coggon, R. C. Flagan, and J. H. Seinfeld. 2015. Vapor wall deposition in Teflon chambers. *Atmos. Chem. Phys.*, 15:4197–4214. doi:10.5194/acp-15-4197-2015.
- Zhang, Y., Y. Chen, A. T. Lambe, N. E. Olson, Z. Lei, R. L. Craig, Z. Zhang, A. Gold, T. B. Onasch, J. T. Jayne, D. R. Worsnop, C. J. Gaston, J. A. Thornton, W. Vizuete, A. P. Ault, and J. D. Surratt. 2018. Effect of the aerosol-phase state on secondary organic aerosol formation from the reactive uptake of isoprene-derived epoxydiols (IEPOX). *Environ. Sci. Technol. Lett.*, 5:167–174. doi:10.1021/acs.estlett.8b00044.
- Zhou, S., M. W. Forbes, and J. P. D. Abbatt. 2016. Kinetics and products from heterogeneous oxidation of squalene with ozone. *Environ. Sci. Technol.*, 50:11688-11697.
- Ziemann, P. J. 2002. Evidence for low-volatility diacyl peroxides as a nucleating agent and major component of aerosol formed from reactions of O₃ with cyclohexene and homologous compounds. *J. Phys. Chem. A*, 106:4390–4402. doi:10.1021/jp012925m.
- Ziemann, P. J. 2003. Formation of alkoxyhydroperoxy aldehydes and cyclic peroxyhemiacetals from reactions of cyclic alkenes with O₃ in the presence of alcohols. *J. Phys. Chem. A*, 107:2048–2060. doi:10.1021/jp022114y.
- Ziemann, P. J. and R. Atkinson. 2012. Kinetics, products, and mechanisms of secondary organic aerosol formation. *Chem. Soc. Rev.*, 41:6582–6605. doi:10.1039/c2cs35122f.